




Fundamental laws of chiral band crossings: Local constraints, global constraints, and topological phase diagrams

Kirill Alpin ^{1,*}, Moritz M. Hirschmann ^{1,2,*}, Niclas Heinsdorf^{1,3}, Andreas Leonhardt ¹, Wan Yee Yau ^{1,4},
Xianxin Wu ^{1,5} and Andreas P. Schnyder¹

¹Max Planck Institute for Solid State Research, Heisenbergstrasse 1, D-70569 Stuttgart, Germany

²RIKEN Center for Emergent Matter Science, Wako, Saitama 351-0198, Japan

³Stewart Blusson Quantum Matter Institute, University of British Columbia, Vancouver BC V6T 1Z4, Canada

⁴Institute for Theoretical Physics III, University of Stuttgart, D-70550 Stuttgart, Germany

⁵Institute for Theoretical Physics, Chinese Academy of Sciences, Beijing, China



(Received 15 May 2023; accepted 12 September 2023; published 21 November 2023)

We derive two fundamental laws of chiral band crossings: (i) a local constraint relating the Chern number to phase jumps of rotation eigenvalues and (ii) a global constraint determining the number of chiral crossings on rotation axes. Together with the fermion doubling theorem, these laws describe all conditions that a network of chiral band crossing must satisfy. We apply the fundamental laws to prove the existence of enforced double Weyl points, nodal planes, and generic Weyl points, among others. In addition, we show that chiral space group symmetries can not stabilize nodal lines with finite Chern numbers. Combining the local constraint with explicit low-energy models, we determine the generic topological phase diagrams of all multifold crossings. Remarkably, we find a fourfold crossing with Chern number 5, which exceeds the previously conceived maximum Chern number of 4. We identify materials crystallizing in space group 198, such as B20 materials and BaAsPt, as suitable compounds with this Chern number 5 crossing.

DOI: [10.1103/PhysRevResearch.5.043165](https://doi.org/10.1103/PhysRevResearch.5.043165)

I. INTRODUCTION

Recent theoretical and experimental efforts have uncovered a huge number of materials with chiral band crossings near the Fermi level [1–6]. These include Weyl semimetals [7–10], where two bands cross at isolated points, nodal plane materials with twofold degeneracies on planes [11–15], as well as materials with multifold band crossings [16–19], such as threefold, fourfold, or sixfold Weyl points. These types of band crossings have been classified by use of symmetry and topology. For example, Refs. [20–31] classified symmetry-enforced topological features of periodic band structures, Refs. [16,19,32–34] studied band topologies of low-energy models, and Refs. [35–37] investigated the connection between rotation eigenvalues and Chern numbers.

Common to chiral band crossings is that their little groups do not contain inversion or mirror symmetries (i.e., are chiral), such that they act as sources or sinks of Berry flux with quantized Chern numbers. As a consequence, chiral Weyl materials exhibit a number of unusual phenomena, e.g., the chiral anomaly [38–41], large negative magnetoresistance [42], or a quantized circular photogalvanic effect [43–45], which might

be utilized for the development of new devices and technologies [46,47]. In combination with magnetic order, chiral band crossings are highly tunable via an external magnetic field [14,48,49], a property that is vital for future applications.

Despite the above mentioned efforts, three fundamental questions remain largely unanswered, namely: (i) What is the underlying reason for the existence of chiral band crossings? (ii) How are different band crossings connected with each other by symmetry and topology? (iii) What are useful guiding principles for the search and design of materials whose chiral band crossings lead to large topological responses? To answer these questions, we derive in this article two fundamental laws, a local and a global constraint, that are satisfied by any set of chiral band crossings connected by symmetry and topology (Secs. II and III). We show that such sets of band crossings from an interrelated network of band topologies [15], whose chiral charges are determined by the fundamental laws. While the local constraint, Eq. (1), relates the chiral charge of the crossing to the jump in symmetry eigenvalues, the global constraint, Eq. (2), restricts the number and types of crossings on a high-symmetry axis, forming parts of the topological network. Together with the fermion doubling theorem by Nielsen and Ninomiya [50], the two fundamental laws describe all the conditions that networks of chiral band topologies must satisfy and therefore provide the fundamental reason for their existence.

To showcase the power of these fundamental laws, we apply them to prove, among others, the existence of enforced double Weyl points (Sec. IV A 1), topological nodal planes (Sec. IV B 1), and generic Weyl points (Sec. IV B 2). We show that nodal lines with finite chiral charges can not be

*These authors contributed equally to this work.

Published by the American Physical Society under the terms of the [Creative Commons Attribution 4.0 International license](https://creativecommons.org/licenses/by/4.0/). Further distribution of this work must maintain attribution to the author(s) and the published article's title, journal citation, and DOI. Open access publication funded by the Max Planck Society.

stabilized by lattice symmetries, but only by internal artificial symmetries, and present a low-energy model that realizes such an artificial chiral nodal line (Sec. IV A 3). Furthermore, we find that, due to the presence of multiple symmetries, the local constraints at multifold crossings can lead to nonminimal Chern number configurations. We show this by using generic low-energy models to derive the general topological phase diagrams of multifold crossings (Sec. V). In this way, we find that there exist fourfold crossings with Chern number 5 (Sec. VB 1), which exceeds the previously conceived maximum Chern number of 4 for multifold crossings [51,52] and for pointlike crossings in general [35,36]. Combining all of these results yields useful principles for the search of materials with chiral (multifold) band crossings. Performing a database search we identify BaAsPt in SG 198 as a suitable compound exhibiting a Chern number 5 crossings at the Fermi level (Sec. VIA) and find that NbO₂ and TaO₂ in SG 80 realize double Weyl points at TRIMs and away from TRIMs (Sec. VIB).

II. TWO SYMMETRY CONSTRAINTS ON CHIRAL CROSSINGS

A chiral band crossing point, commonly referred to as a Weyl point, acts as a monopole of Berry curvature $\mathbf{\Omega}(\mathbf{k})$. Each Weyl point can be characterized by a topological charge, the chirality, which is given by the Chern number ν calculated on a closed manifold of gapped bands surrounding the crossing point. Previously, it has been found that a crossing at \mathbf{k}_c is always topologically charged, if the little group $G_{\mathbf{k}_c}$ is chiral, i.e., if there are neither inversion nor mirror symmetries [11]. Without fine-tuning or additional symmetries the charge of a Weyl point is $\nu = \pm 1$.

If one considers one or more rotation symmetries, the Chern numbers ν of all chiral crossing in the BZ as well as their multiplicity are subject to local and global constraints, respectively. In this section we formulate these two constraints on the existence and the topological charge of chiral crossings, generalizing previous works [35–37]. The proofs are then given in Sec. III.

A. The local constraint

We find a simple relation how the charge ν_{b,c_b} of a crossing c_b between the bands numbered by b and $b+1$ is related to the change of complex phase $\Delta\varphi_{b,c_b}$ of an n -fold rotation eigenvalue λ_b . Here and in what follows, we sort the bands by their energy, i.e., $E_{b+1}(\mathbf{k}) > E_b(\mathbf{k}) \forall \mathbf{k}$. For a given band b the eigenvalue $\lambda_b(\mathbf{k})$ is generally a function of the crystal momentum \mathbf{k} , which is restricted to the rotation axis. The eigenvalue may, but does not need to jump at each crossing on the axis, yielding $\Delta\varphi_{b,c_b} = \arg(\lambda_b(\mathbf{k}_{c_b} + \epsilon\hat{\mathbf{z}})/\lambda_b(\mathbf{k}_{c_b} - \epsilon\hat{\mathbf{z}}))$ with the unit vector along the rotation axis $\hat{\mathbf{z}}$ and $\epsilon > 0$ is sent to 0, see Fig. 1(a).

With these definitions we will show that

$$\nu_{b,c_b} = \Delta\varphi_{b,c_b} \frac{n}{2\pi} \pmod{n}, \quad (1)$$

where the complex phase is only determined up to the order n of the rotation axis. Equation (1) includes previous results obtained for low-energy models subject to one rotation

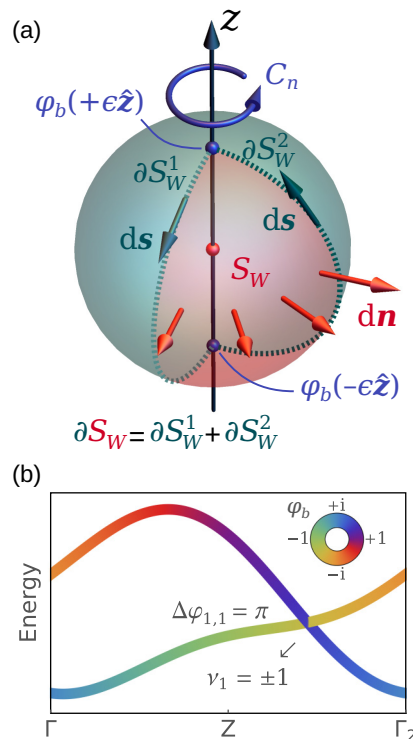


FIG. 1. (a) *Local constraint.* Integration area to determine the Chern number around a point crossing (red sphere). In the presence of a C_n rotation the full sphere of radius ϵ (green + red) comprises n symmetry-related copies of the spherical wedge S_W (red). By Stokes theorem the flux of Berry curvature $\mathbf{\Omega}$ through S_W is equal to the line integral of the Berry connection \mathbf{A} along its boundary ∂S_W (dashed lines). The value of the Berry phase depends on $\Delta\varphi_{b,c_b} = \varphi(+\epsilon\hat{\mathbf{z}}) - \varphi(-\epsilon\hat{\mathbf{z}})$. (b) *Global constraint.* The phase φ_b of screw rotation symmetry eigenvalues enforces a band crossing in band b with chirality ν_b . The points $\Gamma(0, 0, 0)$ and $\Gamma_2(0, 0, 2\pi)$ are related by a reciprocal lattice vector.

symmetry and a time-reversal symmetry [35,36], and agrees with the expression derived by classifying equivariant line bundles [37]. If one recalls that at generic low-symmetry positions the number of singly charged Weyl points is restricted by rotation symmetry to be an integer multiple of n , one expects that a larger charge $|\nu_{b,c_b}| > n/2$ localized to a point is fine-tuned. Therefore, although the relation is only valid \pmod{n} , it is expected that real systems are restricted to crossings with $|\nu_{b,c_b}| < n/2$. Equation (1) is valid even with time-reversal symmetry or other crystalline symmetries as long as the crossing c_b is pointlike, e.g., also if time-reversal enables a gapless crossings between equal rotation eigenvalues. With this insight a recently discovered type of unusual twofold double Weyl point, which occurs on a twofold instead of a fourfold or sixfold rotation axis away from time-reversal invariant momenta (TRIMs), can be understood, see Sec. IV A 1. But a caveat is in order here: If time-reversal and screw symmetries appear together not only can equal eigenvalues be paired but in several cases this enforces nodal planes, in which case Eq. (1) does not apply.

We will see that Eq. (1) is a central tool to identify the topology of nodal planes. Since our results can be applied

to more than one rotation symmetry at a time, it provides a handle to study higher-fold crossings, where more than two bands intersect. In such crossings every band b is subject to Eq. (1) for each rotation symmetry, assuming the bands are nondegenerate on the rotation axis.¹ We will see in Sec. IV A 2 that this not only explains the observed topological charges, but results in more than one possible configuration of topological charges.

B. The global constraint

The second implication of rotation (and mirror) symmetries that governs the qualitative band topology of topological (semi)metals, is a global constraint on the number and type of required crossings c_b per band b . Generally, two types of crystalline symmetries can be distinguished, those with symmorphic operations, which leave at least one point in space invariant, and those with nonsymmorphic operations that leave no point invariant, e.g., screw rotations and glide mirror operations. Since the BZ is periodic, nonsymmorphic symmetries lead to an exchange of bands, due to the \mathbf{k} dependence of their eigenvalues $\lambda_b(\mathbf{k})$, which implies the existence of at least one band crossing on a nonsymmorphic rotation axis [53]. Conversely, for bands along a symmorphic rotation axis, it must be possible to undo all band crossings via pair annihilation, due to the BZ periodicity. These constraints can be formalized with complex phase differences $\Delta\varphi_{b,c_b}$. We consider an n -fold symmetry comprising a translation $(a, b, \frac{m}{n})$, e.g., for a rotation this corresponds to $\{C_n^z|a, b, \frac{m}{n}\}$ in the Seitz notation. If a band b is not part of a multifold crossings, one finds for each of the rotation axes

$$\sum_{b,c_b} \Delta\varphi_{b,c_b} = -b \cdot 2\pi \frac{m}{n} \pmod{2\pi}, \tag{2}$$

which only depends on the band index b , the translation part $\frac{m}{n}$, and the phase difference $\Delta\varphi_{b,c_b}$ for crossings c_b between the bands b and $b + 1$. If there is a multifold crossing for band b , a similar relation has to be considered, where c_b also includes crossings to higher and lower bands, see Eq. (49). Equation (2) constrains the complex phase that must be accumulated as one moves through the BZ, up to multiples of 2π . If the right side of Eq. (2) is nonzero up to 2π , it is clear that there must be at least one crossing, which contributes to the summation on the left side. We note that a glide mirror symmetry can be treated analogously, by considering crossings on any path within the mirror plane that crosses the entire BZ, such that it is closed due the periodicity in \mathbf{k} . The usefulness of this formalization for rotation symmetric systems becomes evident in conjunction with our first result, Eq. (1), which relates each $\Delta\varphi_{b,c_b} \neq 0$ to a topological charge. Therefore Eq. (2) states that the *total chirality* of all crossings on a rotation axis is given by the band index and the translation part of the screw, up to multiples of the order of the rotation axis. This implies that accidental crossings on the rotation axis may change the total charge only by multiples of the order of the rotation axis, which is reminiscent of what happens at generic

positions, where a symmetry imposes certain multiplicities of topological crossings.

III. DERIVATION OF THE TWO CONSTRAINTS

In this section, we derive the local and global constraints, which were discussed in the previous section. For pedagogical reasons, we first present the proof for nondegenerate bands in Sec. III A and then generalize it to degenerate bands in Sec. III B. In Sec. III C, we discuss properties of the sewing matrix with antiunitary symmetries. The global constraint is derived in Sec. III D.

A. Abelian Chern numbers and eigenvalue jumps

In the following, we derive the constraint, Eq. (1), on the Chern number ν of a crossing c_b in band b , which is protected by an n -fold rotation symmetry C_n . A related proof is given in Ref. [37], where the Picard group of complex line bundles is computed over a sphere subject to a cyclic group action. To give self-contained proofs, we calculate the Chern number by generalizing the formalism used in Refs. [54–58] to spherical integration surfaces. The Chern number for a nondegenerate band is defined using the flux of Berry curvature $\mathbf{\Omega}(\mathbf{k})$ through a surface S enclosing the crossing as

$$\nu = \frac{1}{2\pi} \int_S d\mathbf{n} \cdot \mathbf{\Omega}(\mathbf{k}), \tag{3}$$

where the surface S is assumed to be a sphere in reciprocal space, without loss of generality, and \mathbf{n} is the vector normal to the sphere, see Fig. 1(a). For ease of presentation, we have excluded here the case of bands that are degenerate also away from the crossing point, for which a non-Abelian Berry curvature must be considered, see Sec. III B. To calculate the Chern number, Eq. (3), we split the sphere S into n spherical wedges S_W , which are related by the C_n rotation symmetry. The Abelian Berry curvature transforms as a vector under rotations, i.e., $D(C_n)\mathbf{\Omega}(\mathbf{k}) = \mathbf{\Omega}(D(C_n)\mathbf{k})$ [55], where $D(C_n)$ is the spatial representation of the rotation C_n . Noting that the scalar product $\mathbf{n} \cdot \mathbf{\Omega}(\mathbf{k})$ is left invariant under the introduction of the orthogonal matrix $D(C_n)$, one obtains

$$\nu = \frac{n}{2\pi} \int_{S_W} d\mathbf{n} \cdot \mathbf{\Omega}(\mathbf{k}). \tag{4}$$

Further, by using that the curvature, $\mathbf{\Omega}(\mathbf{k}) = \nabla \times \mathbf{A}$, is the rotation of the Berry connection $(\mathbf{A}(\mathbf{k}))_{ab} = i\langle u_a(\mathbf{k})|\nabla|u_b(\mathbf{k})\rangle$, where $|u_b(\mathbf{k})\rangle$ is the orbital part of a Bloch eigenfunction of the considered Hamiltonian, we can write Eq. (4) in terms of the Berry connection \mathbf{A} . For a sufficiently small sphere S , the only relevant divergence of the Berry curvature $\mathbf{\Omega}(\mathbf{k})$ occurs at the crossing c_b , i.e., $\mathbf{\Omega}(\mathbf{k})$ has continuous derivatives on S . We can thus apply Stokes theorem and find

$$\nu = \frac{n}{2\pi} \int_{\partial S_W} d\mathbf{s} \cdot \mathbf{A}(\mathbf{k}) \pmod{n}. \tag{5}$$

We note, that the integration in Eq. (5) corresponds to the Berry phase. Hence, Stokes theorem holds up to multiples of 2π , which, when taking the factor $\frac{n}{2\pi}$ into account, amounts to an equation valid \pmod{n} . In other words, the U(1) gauge freedom of eigenstates implies that the integration of $\mathbf{A}(\mathbf{k})$ in

¹In the degenerate case, one must use Eq. (18).

Eq. (5) can be changed by any integer multiple of 2π , whereas the Chern number ν is gauge-invariant. When we want to determine the value of the Chern number, the corresponding gauge choice is not known, and thus Eq. (5) holds modulo n .

The closed path ∂S_W can be split into two open and C_n -symmetry related paths ∂S_W^1 and ∂S_W^2 , i.e., $\partial S_W = \partial S_W^1 + \partial S_W^2$. But since a nonzero Berry flux through the surface S_W implies that no single-valued phase convention can be found on the full edge ∂S_W , we need to account for a mismatch in the phase convention. For this purpose we consider the sewing matrix \mathcal{B} , which is defined as [55]

$$[\mathcal{B}_{C_n}(\mathbf{k})]_{ab} = \langle u_a(D(C_n)\mathbf{k}) | U(C_n) | u_b(\mathbf{k}) \rangle, \quad (6)$$

where $U(C_n)$ describes the action of the rotation on the eigenstates of the Hamiltonian $|u_b(\mathbf{k})\rangle$. For nondegenerate bands, the sewing matrix is simply a complex phase factor $[\mathcal{B}_{C_n}(\mathbf{k})]_{ab} = \delta_{ab} e^{i\phi_b(\mathbf{k})}$. Specifically, at symmetry invariant momenta \mathbf{k}_{inv} with $D(C_n)\mathbf{k}_{\text{inv}} = \mathbf{k}_{\text{inv}}$ the sewing matrix, Eq. (6), reduces to the symmetry eigenvalue $\lambda_b = e^{i\phi_b(\mathbf{k}_{\text{inv}})}$ of $U(C_n)$ for band b , i.e., $\phi_b(\mathbf{k}_{\text{inv}}) = \varphi_b(\mathbf{k}_{\text{inv}})$. More generally, at \mathbf{k}_{inv} the sewing matrix becomes a diagonal matrix for an appropriate basis within a degenerate subspace. The Berry connection is then given by [55]

$$\begin{aligned} \mathbf{A}(D(C_n)\mathbf{k}) &= D(C_n)[\mathcal{B}_{C_n}(\mathbf{k})\mathbf{A}(\mathbf{k})\mathcal{B}_{C_n}^{-1}(\mathbf{k}) \\ &\quad + i\mathcal{B}_{C_n}(\mathbf{k})\nabla\mathcal{B}_{C_n}^{-1}(\mathbf{k})], \end{aligned} \quad (7)$$

see Appendix A for details. For nondegenerate bands $i\mathcal{B}_{C_n}(\mathbf{k})\nabla\mathcal{B}_{C_n}^{-1}(\mathbf{k}) = \nabla\phi_b(\mathbf{k})$ and $\mathcal{B}_{C_n}(\mathbf{k})\mathbf{A}(\mathbf{k})\mathcal{B}_{C_n}^{-1}(\mathbf{k}) = \mathbf{A}(\mathbf{k})$. Using the fact that the path ∂S_W^2 corresponds to the rotated path ∂S_W^1 but traversed in the reversed direction, we perform an integral substitution with $\mathbf{k} = D(C_n)\mathbf{k}'$ in the line integral over ∂S_W^2 , which turns the integration path ∂S_W^2 into $-\partial S_W^1$. The integral substitution has a unity Jacobian determinant, such that the term with $\mathbf{A}(\mathbf{k})$ cancels leaving only the sewing matrix term. Using Eq. (5), we complete the proof of Eq. (1),

$$\nu = \frac{n}{2\pi} \left(\int_{\partial S_W^1} ds \cdot \mathbf{A}(\mathbf{k}) + \int_{\partial S_W^2} ds \cdot \mathbf{A}(\mathbf{k}) \right) \pmod n \quad (8)$$

$$= -\frac{n}{2\pi} \int_{\partial S_W^1} ds \cdot \nabla\phi_b(\mathbf{k}) \pmod n \quad (9)$$

$$= \frac{n}{2\pi} (\varphi(\mathbf{k}_{c_b} + \epsilon\hat{\mathbf{z}}) - \varphi(\mathbf{k}_{c_b} - \epsilon\hat{\mathbf{z}})) \pmod n \quad (10)$$

$$= \frac{n}{2\pi} \Delta\varphi \pmod n, \quad (11)$$

where $\mathbf{k}_{c_b} + \epsilon\hat{\mathbf{z}}$ and $\mathbf{k}_{c_b} - \epsilon\hat{\mathbf{z}}$ are the north and south pole of the original sphere, respectively, see Fig. 1(a). The difference in complex phases $\Delta\varphi_{b,c_b}$ of the enclosed crossing is only meaningful up to multiples of 2π , which is consistent with the equality up to $\pmod n$.

A comment on the used gauge is in order. Here, we have used the cell-periodic part of the Bloch functions in the calculation of the Chern number and Berry phase [59], the \mathbf{k} dependence of the phases $\varphi_b(\mathbf{k})$ originates only from the exchange of symmetry eigenvalues and the wave functions $u_{b\mathbf{k}}(\mathbf{r})$ that correspond to $|u_b(\mathbf{k})\rangle$ are periodic in \mathbf{r} in agreement with the crystal lattice. In the next section, we will consider Bloch functions $\psi_{b\mathbf{k}}(\mathbf{r}) = e^{i\mathbf{k}\cdot\mathbf{r}}u_{b\mathbf{k}}(\mathbf{r})$, which capture

the periodicity of the Brillouin zone, i.e., $\psi_{b\mathbf{k}+\mathbf{K}}(\mathbf{r}) = \psi_{b\mathbf{k}}(\mathbf{r})$ for all reciprocal lattice vectors \mathbf{K} . The symmetry action for the periodic gauge $\psi_{b\mathbf{k}}(\mathbf{r})$ captures the global symmetry constraints on the band structure, because the symmetry eigenvalues of nonsymmorphic symmetries gain a phase factor that represents the translation part of the screw and glide symmetry operations. Nevertheless, Eq. (1) holds independently of the gauge choice, because all symmetry eigenvalues on a rotation axis obtain the same additional \mathbf{k} dependence in $\varphi_b(\mathbf{k})$. In other words, practically we think of $\Delta\varphi_{b,c_b}$ in the limit of $\epsilon \rightarrow 0$ [see, e.g., Eq. (10)], whereby $\Delta\varphi_{b,c_b}$ becomes the same for both conventions.

B. Non-Abelian Chern numbers and eigenvalue jumps

For bands with degeneracies on S , for example pairs of bands forming a nodal plane, Eq. (1) is not applicable, since Chern numbers can either become undefined or assume noninteger values. But in these cases, a non-Abelian Chern number can still be defined [60]

$$\nu_{b_1 b_2} = \frac{1}{2\pi} \int_S d\mathbf{n} \cdot \text{tr} \mathbf{\Omega}^{b_1 b_2}(\mathbf{k}), \quad (12)$$

where the trace runs over band indices b with $b_1 \leq b \leq b_2$ and the non-Abelian Berry curvature and connection [61] are

$$\mathbf{\Omega}^{b_1 b_2} = \nabla_{\mathbf{k}} \times \mathbf{A} - i\mathbf{A} \times \mathbf{A}, \quad (13)$$

$$\mathbf{A}^{nm} = i\langle n | \nabla_{\mathbf{k}} | m \rangle, \quad (14)$$

respectively, with $b_1 \leq n, m \leq b_2$. The band index range b_1, \dots, b_2 must be chosen such that these bands have a nonzero bandgap to bands $b_1 - 1$ and $b_2 + 1$ on the surface S .

A similar equation as Eq. (1) can be derived for non-Abelian Chern numbers. Using Eq. (12) and (13), we have

$$\begin{aligned} \nu_{b_1 b_2} &= \frac{1}{2\pi} \int_S d\mathbf{n} \cdot \text{tr}(\nabla_{\mathbf{k}} \times \mathbf{A} - i\mathbf{A} \times \mathbf{A}) \\ &= \frac{1}{2\pi} \int_S d\mathbf{n} \cdot \text{tr}(\nabla_{\mathbf{k}} \times \mathbf{A}) \\ &= \frac{n}{2\pi} \int_{\partial S_W} ds \cdot \text{tr} \mathbf{A}(\mathbf{k}) \pmod n, \end{aligned} \quad (15)$$

where we used the fact that $\text{tr}(\mathbf{A} \times \mathbf{A}) = 0$ since $\text{tr}(A_j A_i - A_i A_j) = 0$. In going from the second to the third line we reduced the integration area using symmetry and applied Stokes theorem just like in the proof for the abelian case. Splitting ∂S_W into ∂S_W^1 and ∂S_W^2 and mapping the latter to the former with Eq. (7), we get

$$\begin{aligned} \nu_{b_1 b_2} &= \left[\frac{n}{2\pi} \int_{\partial S_W^1} ds \cdot \text{tr} \mathbf{A}(\mathbf{k}) \right. \\ &\quad - \frac{n}{2\pi} \int_{\partial S_W^1} ds \cdot \text{tr}(\mathcal{B}_{C_n}(\mathbf{k})\mathbf{A}(\mathbf{k})\mathcal{B}_{C_n}^{-1}(\mathbf{k})) \\ &\quad \left. - i \frac{n}{2\pi} \int_{\partial S_W^1} ds \cdot \text{tr}(\mathcal{B}_{C_n}(\mathbf{k})\nabla\mathcal{B}_{C_n}^{-1}(\mathbf{k})) \right] \pmod n \\ &= -i \frac{n}{2\pi} \int_{\partial S_W^1} ds \cdot \text{tr}(\mathcal{B}_{C_n}(\mathbf{k})\nabla\mathcal{B}_{C_n}^{-1}(\mathbf{k})) \pmod n, \end{aligned} \quad (16)$$

where we used $\text{tr}(\mathcal{B}_{C_n}(\mathbf{k})\mathbf{A}(\mathbf{k})\mathcal{B}_{C_n}^{-1}(\mathbf{k})) = \text{tr}\mathbf{A}(\mathbf{k})$. Using Jacobi's formula, we have

$$\begin{aligned} \frac{d}{d\lambda} \log \det \mathcal{B}_{C_n}^{-1}(\lambda) &= \frac{1}{\det \mathcal{B}_{C_n}^{-1}(\lambda)} \frac{d \det \mathcal{B}_{C_n}^{-1}(\lambda)}{d\lambda} \\ &= \text{tr} \left(\mathcal{B}_{C_n}(\lambda) \frac{d\mathcal{B}_{C_n}^{-1}(\lambda)}{d\lambda} \right). \end{aligned} \quad (17)$$

Combining this with Eq. (16), we obtain

$$\begin{aligned} \nu_{b_1 b_2} &= -i \frac{n}{2\pi} \int_{\partial S_W^1} ds \cdot \nabla_{\mathbf{k}} \log \det \mathcal{B}_{C_n}^{-1}(\mathbf{k}) \quad \text{mod } n \\ &= -i \frac{n}{2\pi} \left[\log \det \mathcal{B}_{C_n}(\mathbf{k}_{c_b} + \epsilon \hat{\mathbf{z}}) \right. \\ &\quad \left. - \log \det \mathcal{B}_{C_n}(\mathbf{k}_{c_b} - \epsilon \hat{\mathbf{z}}) \right] \quad \text{mod } n. \end{aligned} \quad (18)$$

This is equivalent to

$$\nu_{b_1 b_2} = \frac{n}{2\pi} \sum_{b=b_1}^{b_2} \Delta\phi_{b, c_b} \quad \text{mod } n, \quad (19)$$

when the bands b_1, \dots, b_2 are nondegenerate, consistent with the abelian case, although here this is also true if the bands are degenerate somewhere on the sphere except at the poles. When they are degenerate at the poles, one must either resort to using Eq. (18) or choose an eigenbasis in the degenerate subspace, such that the sewing matrix \mathcal{B}_{C_n} is diagonal and use Eq. (19). In cases where degenerate bands on the rotation axis belong to distinct representations with $\Delta\phi_{b, c_b} < \pi$, it is possible to improve upon Eqs. (19) and (18). To do so one may consider any slightly symmetry-broken phase that reduces the degeneracy but preserves the considered n -fold rotation symmetry, where the signs of all ν can be uniquely defined using the local constraint in Eq. (1). An extension of this is discussed in the final remarks of Sec. IV B 1.

C. Sewing matrices of antiunitary symmetries

In this section, we derive similar expressions for the antiunitary symmetries as in Sec. III A. Applying these to generic crossings, we find that single-band Chern numbers of crossings with time-reversal symmetry have even (odd) Chern numbers without (with) SOC. In the following, W is either just the time-reversal symmetry $W = T$, with $R = 1$ or W is a combination of time-reversal and a crystalline symmetry with a real space representation R . In later examples, we are concerned with the $R = D(C_n)$ case. We start with the derivation of the sewing matrix α for nondegenerate bands

$$WH(\mathbf{k})W^{-1} = H(-R\mathbf{k}) \quad (20)$$

$$\Rightarrow WH(\mathbf{k})|u(\mathbf{k})\rangle = H(-R\mathbf{k})W|u(\mathbf{k})\rangle \quad (21)$$

$$\Rightarrow E(\mathbf{k})W|u(\mathbf{k})\rangle = H(-R\mathbf{k})W|u(\mathbf{k})\rangle \quad (22)$$

so $W|u(\mathbf{k})\rangle$ must be an eigenstate of $H(-R\mathbf{k})$. Therefore

$$\alpha(\mathbf{k})|u(-R\mathbf{k})\rangle = W|u(\mathbf{k})\rangle, \quad (23)$$

which leads to the sewing matrix for antiunitary symmetries

$$\alpha(\mathbf{k}) = \langle u(-R\mathbf{k})|W|u(\mathbf{k})\rangle. \quad (24)$$

The Berry connection transforms under W like so

$$\begin{aligned} A(\mathbf{k}) &= i\langle u(\mathbf{k})|\partial_{\mathbf{k}}|u(\mathbf{k})\rangle \\ &= -i\langle u(\mathbf{k})|W^\dagger \partial_{\mathbf{k}} W|u(\mathbf{k})\rangle \\ &= -i\alpha^*(\mathbf{k})\langle u(-R\mathbf{k})|\partial_{\mathbf{k}}\alpha(\mathbf{k})|u(-R\mathbf{k})\rangle \\ &= iR^{-1}\langle u(-R\mathbf{k})|\partial_{-R\mathbf{k}}|u(-R\mathbf{k})\rangle - i\alpha^*(\mathbf{k})\partial_{\mathbf{k}}\alpha(\mathbf{k}) \\ &= R^{-1}A(-R\mathbf{k}) - i\alpha^*(\mathbf{k})\partial_{\mathbf{k}}\alpha(\mathbf{k}), \end{aligned} \quad (25)$$

where we used

$$\begin{aligned} &\langle u(\mathbf{k})|W^\dagger \partial_{k_i} W|u(\mathbf{k})\rangle \\ &= \lim_{\epsilon \rightarrow 0} \langle u(\mathbf{k})|W^\dagger \frac{1}{\epsilon} (W|u(\mathbf{k} + \epsilon \mathbf{e}_i)\rangle - W|u(\mathbf{k})\rangle) \\ &= \lim_{\epsilon \rightarrow 0} \frac{1}{\epsilon} (\langle u(\mathbf{k})|W^\dagger W|u(\mathbf{k} + \epsilon \mathbf{e}_i)\rangle - \langle u(\mathbf{k})|W^\dagger W|u(\mathbf{k})\rangle) \\ &= \lim_{\epsilon \rightarrow 0} \frac{1}{\epsilon} (\langle u(\mathbf{k} + \epsilon \mathbf{e}_i)|u(\mathbf{k})\rangle - \langle u(\mathbf{k})|u(\mathbf{k})\rangle) \\ &= \langle \partial_{k_i} u(\mathbf{k})|u(\mathbf{k})\rangle = -\langle u(\mathbf{k})|\partial_{k_i} u(\mathbf{k})\rangle \end{aligned} \quad (26)$$

together with the antiunitarity of W

$$\langle \Psi|W^\dagger W|\Phi\rangle = \langle W\Psi|W\Phi\rangle = \langle \Phi|\Psi\rangle \quad (27)$$

and

$$\langle u(\mathbf{k})|u(\mathbf{k})\rangle = 1 \quad (28)$$

$$\Rightarrow \partial_{\mathbf{k}} \langle u(\mathbf{k})|u(\mathbf{k})\rangle = 0 \quad (29)$$

$$\Rightarrow \langle \partial_{\mathbf{k}} u(\mathbf{k})|u(\mathbf{k})\rangle = -\langle u(\mathbf{k})|\partial_{\mathbf{k}} u(\mathbf{k})\rangle. \quad (30)$$

1. Chern number constraints from $C_n T$ symmetries

Using Eq. (25), we can derive expressions similar to Eq. (1) for $C_4 T$

$$\begin{aligned} \nu_{c_b} &= \frac{2}{\pi} [\phi(\mathbf{S}) - \phi(\mathbf{N})] \quad \text{mod } 4 \\ &= -\frac{2}{\pi} \Delta\phi_{b, c_b} \quad \text{mod } 4, \end{aligned} \quad (31)$$

and for $C_6 T$

$$\nu_{c_b} = -\frac{3}{\pi} \Delta\phi_{b, c_b} \quad \text{mod } 3, \quad (32)$$

with $\alpha(\mathbf{k}) = e^{-i\phi(\mathbf{k})}$. The constraint for $C_6 T$ is only defined mod 3 instead of mod 6, since $C_6 T$ relates the Berry curvature of wedges spanning 1/3 of a sphere to each other, instead of 1/6 wedges. The main difference of Eqs. (31) and (32) to Eq. (1) is that $\Delta\phi_{b, c_b}$ is no longer the change of a symmetry eigenvalue but the phase change of the antiunitary symmetry sewing matrix (24).

$C_2 T$ relates the Berry curvature of the upper to the lower hemisphere, so to derive a local constraint we need to consider a path $\partial S_{\text{equator}}$ on the equator

$$\nu_{c_b} = \frac{1}{\pi} \int_{\partial S_{\text{equator}}} \mathbf{A}(\mathbf{k}) d\mathbf{k} \quad \text{mod } 2 \quad (33)$$

$$= \frac{1}{\pi} \int_{\partial S_{\text{equator}}} D(C_2) \mathbf{A}(\mathbf{k}) d\mathbf{k} - \frac{1}{\pi} \int_{\partial S_{\text{equator}}} i\alpha^*(\mathbf{k}) \partial_{\mathbf{k}} \alpha(\mathbf{k}) d\mathbf{k} \pmod{2} \quad (34)$$

$$= -\frac{1}{\pi} \int_{\partial S_{\text{equator}}} \mathbf{A}(\mathbf{k}) d\mathbf{k} - \frac{1}{\pi} \int_{\partial S_{\text{equator}}} i\alpha^*(\mathbf{k}) \partial_{\mathbf{k}} \alpha(\mathbf{k}) d\mathbf{k} \pmod{2} \quad (35)$$

$$\Rightarrow \nu_{c_b} = -\frac{1}{2\pi} \int_{\partial S_{\text{equator}}} \partial_{\mathbf{k}} \phi(\mathbf{k}) d\mathbf{k} \pmod{2}, \quad (36)$$

where we used Eq. (25), $\mathbf{A}(-D(C_2)\mathbf{k}) = \mathbf{A}(\mathbf{k})$ and $(D(C_2)\mathbf{v})d\mathbf{k} = -\mathbf{v}d\mathbf{k}$ with any vector \mathbf{v} on the equator. So ν_{c_b} is even (odd) when $\phi(\mathbf{k})$ winds an even (odd) number of times around the equator.

A C_3T constraint is redundant, since C_3T implies $T = (C_3T)^3$ and therefore also C_3 to exist separately.

2. Chern number constraint of crossings at TRIMs

Next we would like to evaluate a single band Chern number of a crossing with time-reversal symmetry, $W = T$ ($R = 1$) and $T^2 = \gamma$, where $\gamma = 1$ for spinless and $\gamma = -1$ for spinful fermions. We split the integration-sphere around the crossing into two halves,

$$\nu = \frac{1}{\pi} \left(\int_{\partial S_1} \mathbf{A}(\mathbf{k}) d\mathbf{k} + \int_{\partial S_2} \mathbf{A}(\mathbf{k}) d\mathbf{k} \right) \pmod{2} \quad (37)$$

$$= \frac{1}{\pi} \left(\int_{\partial S_1} \mathbf{A}(\mathbf{k}) d\mathbf{k} + \int_{\partial S_2} \mathbf{A}(-\mathbf{k}) d\mathbf{k} - \int_{\partial S_2} i\alpha^*(\mathbf{k}) \partial_{\mathbf{k}} \alpha(\mathbf{k}) d\mathbf{k} \right) \pmod{2} \quad (38)$$

$$= -\frac{1}{\pi} \int_{\partial S_2} i\alpha^*(\mathbf{k}) \partial_{\mathbf{k}} \alpha(\mathbf{k}) d\mathbf{k} \pmod{2}, \quad (39)$$

where ∂S_1 and ∂S_2 are two paths of equal length that form the boundary between the two halves of the full integration surface. Using $\alpha(\mathbf{k}) = e^{-i\phi(\mathbf{k})}$ we have

$$\nu = -\frac{1}{\pi} \int_{\partial S_2} \partial_{\mathbf{k}} \phi(\mathbf{k}) d\mathbf{k} \pmod{2} \quad (40)$$

$$= \frac{1}{\pi} (\phi(\mathbf{S}) - \phi(\mathbf{N})) \pmod{2} \quad (41)$$

with \mathbf{N} and \mathbf{S} being the north and southpole. To evaluate this expression, consider Eq. (23). We can reinsert itself with a replacement $\mathbf{k} \rightarrow -\mathbf{k}$ to get

$$\alpha(\mathbf{k}) |u(-\mathbf{k})\rangle = T \alpha^*(-\mathbf{k}) T |u(-\mathbf{k})\rangle \quad (42)$$

$$= \alpha(-\mathbf{k}) \gamma |u(-\mathbf{k})\rangle \quad (43)$$

so

$$\gamma = \alpha(\mathbf{k}) \alpha^*(-\mathbf{k}) \quad (44)$$

$$= e^{-i(\phi(\mathbf{k}) - \phi(-\mathbf{k}))}, \quad (45)$$

which can be applied to Eq. (41) to arrive at $\nu = 0 \pmod{2}$ for the spinless case ($\gamma = 1$) and $\nu = 1 \pmod{2}$ for the spinful one ($\gamma = -1$). So any crossing at TRIMs, which includes also

multifold ones, without further degeneracies away from the crossing, must have even (odd) Chern numbers without (with) SOC. We see that this constraint is explicitly fulfilled in all models found in this paper, for example in Sec. VB and in all low-energy Weyl point Hamiltonians at TRIMs in Ref. [36].

D. Global constraint on band topology

For chiral band crossings, global constraints on the band topology arise due to conditions on the sum of the topological charges of nodal points. One such global constraint is the fermion doubling theorem by Nielsen and Ninomiya, which states that for each band the sum of all chiralities has to vanish [50]. Here, we prove a global constraint on the rotation eigenvalues, which ultimately follows from the periodicity of the BZ [62]. To do so, we employ symmetry representations along the full rotation axis, which can be obtained by taking powers of the symmetry [63]. For concreteness we consider a screw rotation symmetry $C_n(x, y, \frac{m}{n})$, which describes an n -fold rotation around the z axis followed by a translation with the vector $(x, y, \frac{m}{n})$. Taking the n th power of the screw rotation, we obtain

$$\left[C_n \left(x, y, \frac{m}{n} \right) \right]^n = e^{i\pi s} T(0, 0, m) = e^{i\pi s + imk_z}, \quad (46)$$

where $m, n \in \mathbb{Z}$, $|m| < |n|$, and $s = 0$ ($s = 1$) for spinless (spinful) systems. In the second step, the translation by a full lattice vector $T(0, 0, m)$ is replaced by the usual one-dimensional representation of the translation group. Notably, the above and all following steps apply analogously to (glide) mirror operations, which would correspond to an operation with $n = 2$ and either $m = 0$ or $m = 1$ for mirror and glide mirror symmetries, respectively. The symmetry eigenvalues of the C_n screw rotation is found as the complex root of Eq. (46) yielding

$$\lambda_{C_n} = \exp \left(i \frac{2\pi p + s\pi + mk_z}{n} \right), \quad (47)$$

where $p \in \{0, 1, \dots, n-1\}$ distinguishes the n different complex roots. On the rotation axes invariant under the rotation $C_n(x, y, \frac{m}{n})$, we label the bands using λ_{C_n} or rather, equivalently, we consider the complex phase $\varphi(k_z) = \arg \lambda_{C_n}$. To label a specific band b that is identified by sorting the eigenvalues of the Hamiltonian according to their energy, we have to consider that Eq. (47) does not yet include band crossings. The phase $\varphi_b(k_z)$ for a specific band is given by

$$\varphi_b(k_z) = \frac{2\pi p + s\pi + mk_z}{n} + \sum_{k_c \leq k_z} \Delta\varphi_{b,c}, \quad (48)$$

which must include all phase jumps $\Delta\varphi_{b,c}$ at k_c corresponding to all crossings c up to k_z , which may be, for example, with the bands $b-1$ or $b+1$. The essential step to identify the global constraints on $\varphi_b(k_z)$, $\Delta\varphi_{b,c}$, and in extension also on all chiral crossings is the periodicity of the Brillouin zone. Thus we compare the phase $\varphi_b(k_z^0)$ at some position k_z^0 with the phase $\varphi_b(k_z^0 + 2\pi)$ after traversing the Brillouin and accumulating phase jumps $\Delta\varphi_{b,c}$ at k_c as well as a contribution

from $\frac{mk_z}{n}$,

$$\begin{aligned} \varphi_b(k_z^0 + 2\pi) - \varphi_b(k_z^0) &= 0 \pmod{2\pi} \\ \Leftrightarrow \sum_{c_b} \Delta\varphi_{b,c} + 2\pi \frac{m}{n} &= 0 \pmod{2\pi}. \end{aligned} \quad (49)$$

The phase jumps $\Delta\varphi_{b,c}$ in Eq. (49) are not independent for different bands b . For every phase jump there is the reverse exchange of eigenvalues in a higher or lower band. Suppose we consider a system, where all band crossings are twofold, then one may iteratively substitute Eq. (49) for band $b - 1$ into the equation for band b . Then crossings c_1 of the first band with the second band must also appear in Eq. (49) for $b = 2$, so $\sum_{c_2} \Delta\varphi_{2,c_2} = \sum_{c_{2,3}} \Delta\varphi_{2,c_{2,3}} + \sum_{c_{1,2}} \Delta\varphi_{2,c_{1,2}}$. Here, $c_{a,b}$ denotes a crossing of band a with band b . So we split up all crossings belonging to band 2 into ones which cross with band 1 and band 3. Further we note, as stated before, $\Delta\varphi_{2,c_{1,2}} = -\Delta\varphi_{1,c_{1,2}}$. The induction process leads to Eq. (2)

$$\begin{aligned} b = 1 & \quad \sum_{c_{1,2}} \Delta\varphi_{1,c_{1,2}} = -2\pi \frac{m}{n} \pmod{2\pi} \\ b = 2 & \quad \sum_{c_{2,3}} \Delta\varphi_{2,c_{2,3}} - \sum_{c_{1,2}} \Delta\varphi_{1,c_{1,2}} = -2\pi \frac{m}{n} \pmod{2\pi} \\ & \quad \Leftrightarrow \sum_{c_{2,3}} \Delta\varphi_{2,c_{2,3}} = -2 \times 2\pi \frac{m}{n} \pmod{2\pi} \\ & \quad \vdots \\ \text{any } b & \quad \sum_{c_{b,b+1}} \Delta\varphi_{b,c_{b,b+1}} = -b \times 2\pi \frac{m}{n} \pmod{2\pi}. \end{aligned} \quad (50)$$

This result contains the notion of filling-enforced semimetals, namely, if $b\frac{m}{n} \notin \mathbb{Z}$, then there must be at least one symmetry-enforced band crossing [20]. Once the filling, i.e., the considered band b , is a multiple of $\frac{n}{m}$, for this specific band no crossings to higher bands need to exist.

IV. APPLICATIONS AND EXTENSIONS

To demonstrate the power of the local and global constraints, we present a number of applications and discuss some extensions.

A. Applications and extensions of the local constraint

In the following we use the local constraint, Eq. (1), to prove the existence of enforced double Weyl points away from TRIMs (Sec. IV A 1). We generalize the local constraint to multiple rotation symmetries in Sec. IV A 2, which enables us to infer conditions for the Chern numbers for all types of (higher-fold) chiral crossings. Finally, we use the local constraint to show that nodal lines with nonzero Chern numbers can not be stabilized by chiral space group symmetries (Sec. IV A 3).

1. Chiral crossings between identical symmetry eigenvalues

In this section we use the local constraint, Eq. (1), to explain the existence of unusual enforced double Weyl points

away from TRIMs [35,36]. First, we clarify why these Weyl points pose an open question in the understanding of chiral crossings. According to conventional wisdom, a stable band degeneracy can only occur if at least one of the three following conditions is fulfilled. (i) The two bands forming the crossing belong to different symmetry representations, which prevents the introduction of gap opening terms, (ii) there is a higher-dimensional representation of the point group, or (iii) time reversal leads to a Kramers degeneracy at a TRIM. However, in space groups 80, 98, and 210 there exist band crossings away from TRIMs between bands with identical representations of dimension one [27]. So at first glance, all of the above three conditions for a crossing seem violated. Yet, the combination of time-reversal and fourfold rotation symmetry generates, due to Kramers theorem, pointlike degeneracies at high-symmetry points of certain nonprimitive Brillouin zones that are not TRIMs [27]. Interestingly, with SOC these crossings are known to be double Weyl points with Chern number ± 2 [28], but could until now not be understood in terms of symmetry eigenvalues [35,36].

For concreteness, let us now focus on the body-centered tetragonal SG 80 ($I4_1$), whose P point can host twofold degeneracies both with and without SOC [e.g., see Figs. 2(a) and 12]. As we will see, this band crossing can be understood by noting that the combined symmetry TC_{4z} , comprising time-reversal T , and fourfold screw rotation C_{4z} , leaves the P point invariant. Other than that, the only unitary symmetry that leaves P invariant is the rotation C_{2z} whose symmetry eigenvalues can be used to label the bands. We now need to distinguish the case with and without SOC, which differ slightly for SG 80. Without SOC different eigenvalues are paired by the antiunitary operation TC_{4z} . In our notation, this corresponds to $\Delta\varphi = \pm\pi$ for the Weyl point at P , which implies by Eq. (1) a Chern number of $\nu_{P,SG80} = 1 \pmod{2}$. With SOC the representation is doubled compared to before and splits into two one-dimensional and one two-dimensional representation at P, because the Kramers theorem only applies to the latter representation, see Ref. [27] for details. Since for the two-dimensional representation one eigenvalue of C_{2z} is paired to itself, one finds $\Delta\varphi = 0$ implying $\nu_{P,SG80,SOC} = 0 \pmod{2}$. Taking into account that the crossing at P has been $\nu_{P,SG80} = 1$ without spin, it follows from the conservation of topological charge that $\nu_{P,SG80,SOC} = \pm 2$. We have thus reached an explanation for the double Weyl point at P in terms of symmetry eigenvalues.

The discussed double Weyl point at P in SG 80 has a different origin and symmetry than any other twofold double Weyl point, which occur either on fourfold or sixfold rotation axes or at TRIMs in the presence of spinless time-reversal symmetry [35,36,64]. Hence, we expect that also the spin texture [65–72] and Berry curvature are distinct from the conventional double Weyl points. To demonstrate this, we compute the Berry curvature and spin texture of the double Weyl point in SG 80. For this purpose, we derive in Appendix B a tight-binding model including SOC for SG 80. Figure 2(a) shows the band structure of this model defined by Eq. (B5). As expected we find a double Weyl point of charge $\nu_P = 2$ at each P point, which is compensated by a pair of double Weyl points on the fourfold rotation axis Γ -Z-M with $\nu_{\Gamma\text{-Z-M}} = -2$. Figures 2(b) and 2(c) show the Berry curvature and spin texture

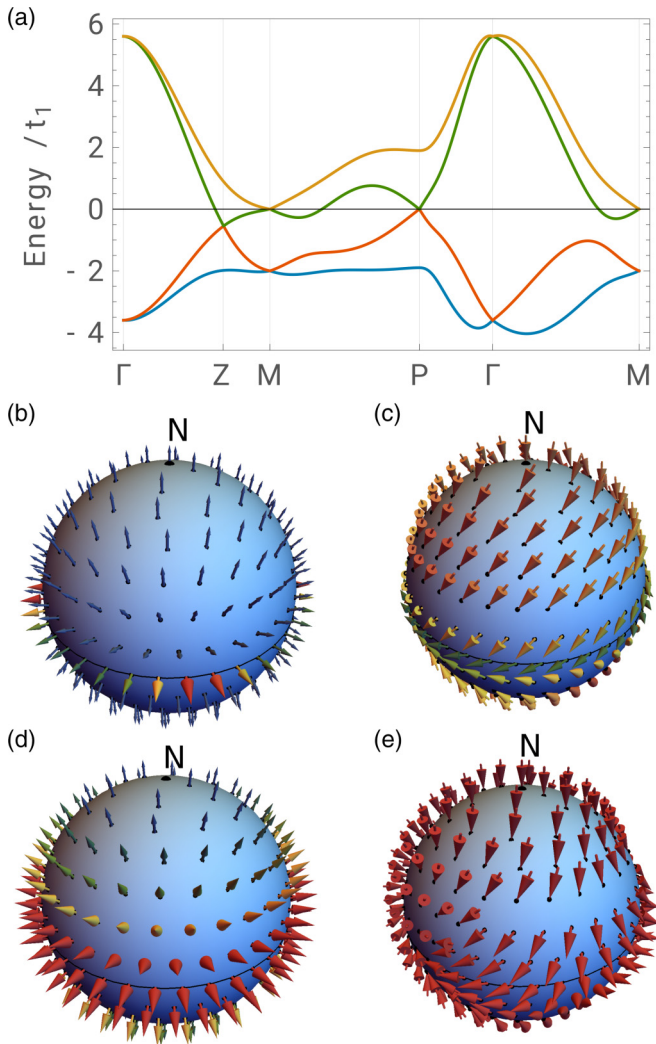


FIG. 2. Band structure, Berry curvature, and spin texture for SG 80. (a) Tight-binding model with SOC of SG 80 as defined in Eq. (B5). The body-centered tetragonal Brillouin zone is shown in the inset of Fig. 11(b). The double Weyl point at P is characterized by its Berry curvature and spin textures as shown in (b) and (c), respectively, which are given for the lower band of the crossing on a sphere enclosing it. For comparison, (d) and (e) show the Berry curvature and spin textures of a regular double Weyl point. For all vector plots, the north pole of the sphere is labeled by “N” and red color denotes a larger magnitude of the vector field than blue.

around the P point, respectively. To contrast this with conventional double Weyl points, we plot in Figs. 2(d) and 2(e) the Berry curvature and spin texture of a conventional double Weyl point defined by $H(\mathbf{k}) = k_z \sigma_z + (\sigma_+(k_x - ik_y)^2 + \text{H.c.})$, where $\sigma_+ = 1/2(\sigma_x + i\sigma_y)$ with the Pauli matrices σ_j [66,73]. While the details of these textures are parameter-dependent, their symmetry properties are generic and dictated by the local little groups. In general the spin texture at P in SG 80 is anisotropic and symmetric under the *antiunitary* C_4T symmetry [see regions of similar color shading in Fig. 2(c)]. In contrast, the texture of a conventional double Weyl point is symmetric under a *unitary* (e.g., fourfold) rotation symmetry, see Figs. 2(d) and 2(e). Another difference is that

the spin texture around the equator of Fig. 2(c) has a unit winding, whereas the one of Fig. 2(e) has a winding of two. These differences in spin texture could be measured experimentally, using, e.g., spin- and angle-resolved photoemission spectroscopy [65,70,72].

Using a database search (see Sec. VI) we have identified NbO₂ and TaO₂ as candidate materials in SG 80 realizing the double Weyl points away from TRIMs. The band structure and surface states of these compounds are presented in Sec. VI B. Notably, we find that for surface terminations perpendicular to any of the crystal axes there appear four Fermi arcs. This is because for these terminations the P point is projected onto a symmetry related copy of itself with the same Chern number ± 2 , such that four Fermi arcs emerge from the projected P point in the surface BZ.

The above arguments for SG 80 apply in a similar manner also to SG 98 ($I4_122$) and SG 210 ($F4_132$), for which the double Weyl points appear at the P and W points, respectively. In addition, related arguments using the local constraint can be employed to understand the charge $\nu = \pm 2$ of the threefold crossings in SG 199 ($I2_13$) and SG 214 ($I4_132$) at the point P, see the discussion in Sec. V B 2.

2. Chiral crossings with multiple rotation axes

Band crossing points symmetric under little groups that contain more than one rotation symmetry often exhibit larger topological charges than in the case of a single rotation symmetry [16,17,51]. Also in this case the local constraint, Eq. (1), can be used to understand the observed topological charges. In the following, we extend the above arguments to multiple rotation axes and consider, for concreteness, a twofold quadruple Weyl point at Γ in SG 195, for which a Chern number of $\nu = 4$ has been reported [73–76]. Other nontrivial examples of nodal points with multiple rotation symmetries are discussed in Secs. IV B 2 and V in the context of multifold band crossings.

For a single rotation axis one usually finds that $\nu_{c_b} = \Delta\varphi_{b,c_b} \frac{n}{2\pi}$ holds without the modulus operation, although the local constraint, Eq. (1), restricts the possible charges only up to the order of the rotation n . This is because higher topological charges would require fine tuning. To see this, consider a crossing point of charge $\nu = \nu_{c_b} + mn$, where m is some nonzero integer. If this crossing is perturbed by some symmetry-allowed perturbation, the crossing may split into one with charge ν_{c_b} and m sets of each n Weyl points. In fact, generally exactly this happens, because placing mn Weyl points on the rotation axis is a fine-tuned situation. In other words, to achieve higher topological charges ν , more lower orders in the low-energy expansion need to be set to zero, which would require fine tuning.

In the presence of multiple rotation symmetries, however, there are more symmetry constraints that can lead to higher topological charges, such that the smallest possible value given by the local constraint (1) is not realized. To demonstrate this, let us consider SG 195 ($P23$) with time-reversal symmetry, where a twofold quadruple Weyl point is enforced to occur at the TRIM Γ (and also at R), if, for example, the $^1E^2E$ representation is placed on the Wyckoff position 1a [77]. The corresponding little group at Γ consist of the point

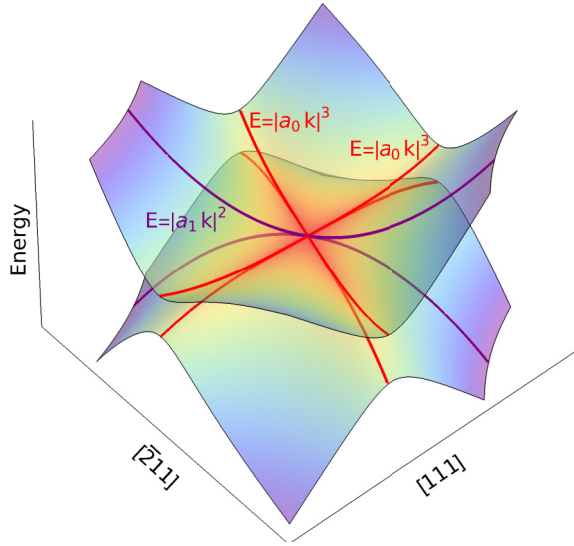


FIG. 3. *Quasisymmetry-enforced Chern number in twofold quadruple Weyl points.* Band structure around a twofold band crossing symmetric under point group 23 and time reversal, as given by Eq. (C1) with $d_1 = 0$. The splitting of the bands along the threefold (twofold) rotation axes in red (purple) is cubic (quadratic). A fourfold quasisymmetry enforces a charge of $\nu = 4$.

group 23 together with time-reversal, which does contain a twofold and a threefold rotation, but no fourfold rotation, different from the conventional twofold quadruple Weyl points of Refs. [73–76]. From the representation of this little group, one finds that there is no exchange of the twofold rotation eigenvalues, while the threefold rotation eigenvalue switch. Thus the local constraint (1) on the charge ν_Γ is

$$\nu_\Gamma = 0 \pmod{2} \quad \text{and} \quad \nu_\Gamma = 1 \pmod{3}. \quad (51)$$

Thus both $\nu_\Gamma = 4$ and $\nu_\Gamma = -2$ are in agreement with Eqs. (51). To resolve this ambiguity we construct a low-energy model $H_T(\mathbf{k})$ around Γ , which is symmetric under the point group 32 and time-reversal, see Appendix C. The energy bands of this model exhibit quadratic and cubic dispersions along different directions away from the crossing point, see Fig. 3. The topological phase diagram of this low-energy model contains only one phase with $\nu_\Gamma = 4$, in agreement with Eq. (51). However, the lowest possible topological charge of $\nu_\Gamma = -2$, cf. Eq. (51), is not realized, in contrast to the conventional twofold quadruple Weyl points with fourfold rotation symmetry [73–76]. This raises the question, why can the charge $\nu_\Gamma = -2$ not be realized in our low-energy model, even though it would be consistent with the local constraint?

There are two ways to answer this question. First, a closer look at the low-energy model presented in Appendix C reveals that there is a fourfold *quasisymmetry*, i.e., a symmetry of the low-energy model that is broken by terms of higher order in k . Namely, the low-energy Hamiltonian $H_T(\mathbf{k})$, Eq. (C1), is left invariant by $U(C_4^z)^\dagger H_T(\mathbf{k}) U(C_4^z) = H_T(D(C_4^z)^{-1}\mathbf{k})$, where $U(C_4^z)$ is the representation of a fourfold rotation symmetry and $D(C_4^z)$ is the corresponding transformation in real space, see Eq. (C4). $U(C_4^z)$ is a quasisymmetry, as it is a symmetry

only of the lowest-order terms, but not of the full Hamiltonian. Yet, since the Chern number is determined exclusively by the lowest orders in k , at which the point crossing is well-defined, this quasisymmetry forces the charge to be $\nu_\Gamma = +4$ for the crossing by adding the local constraint $\nu_\Gamma = 0 \pmod{4}$.

Second, the Chern number $\nu_\Gamma = 0 \pmod{4}$ can be understood by considering how the symmetries act on the Berry curvature integration. For this purpose, we need to consider the role of the time-reversal symmetry together with the twofold rotation, to be specific the combination C_2T . The Berry curvature flux through the northern $S_W(N)$ and southern $S_W(S)$ half of the spherical wedge S_W when considering C_2 are identical due to C_2T and thus

$$\nu_\Gamma = 2 \frac{2}{2\pi} \int_{S_W(N)} d\mathbf{n} \cdot \mathbf{\Omega}(\mathbf{k}) \quad (52)$$

$$= \frac{2}{\pi} \int_{\partial S_{NP_1} + \partial S_{equator} + \partial S_{P_2N}} \mathbf{A} ds \pmod{4}, \quad (53)$$

where we split the path $S_W(N)$ into $\partial S_{NP_1} + \partial S_{equator} + \partial S_{P_2N}$ and P_1 and P_2 being endpoints of $\partial S_{equator}$. The Berry connection integration on paths ∂S_{NP_1} and ∂S_{P_2N} are related by symmetry and can be evaluated in a similar way as in Eq. (8),

$$\int_{\partial S_{NP_1} + \partial S_{P_2N}} \mathbf{A} ds = \phi_b(\mathbf{P}_1) - \phi_b(\mathbf{N}). \quad (54)$$

Regarding the $\partial S_{equator}$ integration, consider Eq. (7) applied on this path

$$\begin{aligned} \int_{\partial S_{equator}} \mathbf{A}(D(C_2)\mathbf{k}) ds &= \int_{\partial S_{equator}} D(C_2)(\mathbf{A}(\mathbf{k}) - \nabla\phi_b(\mathbf{k})) ds \\ \Rightarrow \int_{\partial S_{equator}} \mathbf{A}(-\mathbf{k}) ds &= - \int_{\partial S_{equator}} \mathbf{A}(\mathbf{k}) - \nabla\phi_b(\mathbf{k}) ds \\ \Rightarrow \int_{\partial S_{equator}} \mathbf{A}(\mathbf{k}) ds &= - \int_{\partial S_{equator}} \mathbf{A}(\mathbf{k}) - \nabla\phi_b(\mathbf{k}) ds \\ \Rightarrow \int_{\partial S_{equator}} \mathbf{A}(\mathbf{k}) ds &= \frac{1}{2} \int_{\partial S_{equator}} \nabla\phi_b(\mathbf{k}) ds \\ &= \frac{1}{2} (\phi_b(\mathbf{P}_2) - \phi_b(\mathbf{P}_1)), \end{aligned} \quad (55)$$

where all equations are valid up to $\pmod{2\pi}$ and with $\mathbf{A}(D(C_2)\mathbf{k}) = \mathbf{A}(-\mathbf{k})$ and $(D(C_2)\mathbf{v}) ds = -\mathbf{v} ds$ with any vector \mathbf{v} on the equator. We also used Eq. (25) relating $\mathbf{A}(\mathbf{k})$ and $\mathbf{A}(-\mathbf{k})$ via time-reversal symmetry

$$\begin{aligned} \int_{\partial S_{equator}} \mathbf{A}(-\mathbf{k}) ds &\pmod{2\pi} \\ &= \int_{\partial S_{equator}} \mathbf{A}(\mathbf{k}) ds - i \int_{\partial S_{equator}} \alpha^*(\mathbf{k}) \partial_{\mathbf{k}} \alpha(\mathbf{k}) ds \pmod{2\pi} \\ &= \int_{\partial S_{equator}} \mathbf{A}(\mathbf{k}) ds + \phi_T(\mathbf{P}_1) - \phi_T(\mathbf{P}_2) \pmod{2\pi} \\ &= \int_{\partial S_{equator}} \mathbf{A}(\mathbf{k}) ds \pmod{2\pi}, \end{aligned} \quad (57)$$

where the time-reversal symmetry sewing matrix has the form $\alpha(\mathbf{k}) = e^{-i\phi_T(\mathbf{k})}$ and $\phi_T(\mathbf{P}_1) = \phi_T(-\mathbf{P}_1) = \phi_T(\mathbf{P}_2)$ in

the spinless case [see Eq. (45)]. In total, we get

$$\nu_{\Gamma} = \frac{2}{\pi} \left(-\phi_b(\mathbf{N}) + \frac{1}{2}(\phi_b(\mathbf{P}_1) + \phi_b(\mathbf{P}_2)) \right) \pmod{4}. \quad (58)$$

Explicitly calculating $\phi_b(\mathbf{P}_1) + \phi_b(\mathbf{P}_2)$ in the irrep $\Gamma_2\Gamma_3$ by plugging in the Bloch wavefunctions of the low-energy Hamiltonian into Eq. (6) yields 0. So

$$\nu_{\Gamma} = \frac{2}{\pi} \varphi(\mathbf{N}) \pmod{4}. \quad (59)$$

The irrep $\Gamma_2\Gamma_3$ in ${}^1E^2E$ of C_2 is σ_0 , so $\varphi(\mathbf{N}) = 0$, which means we get

$$\nu_{\Gamma} = 0 \pmod{4}. \quad (60)$$

A material implementation of this WP with charge 4 was found in BaIrP, see Ref. [73]. There it is shown that, upon introducing SOC, this crossing evolves into 12 WPs and a fourfold crossing at Γ with $C = \nu_{1,2} = \pm 4$, which is in Sec. VB 1 revealed to be the $\nu_n = \{\pm 3, \pm 1, \mp 1, \mp 3\}$ phase of the model described there.

3. Chiral nodal lines

Nodal lines protected by crystalline symmetries are commonly discussed in the context of mirror symmetries, which leave a plane in the Brillouin zone invariant where they provide two distinct representations. The presence of two distinct representations is sufficient to obtain accidental nodal lines. Furthermore, there can be symmetry-enforced line crossings, for example, if another symmetry operation anticommutes with the mirror symmetry, one finds nodal lines pinned to high-symmetry paths. Alternatively, if the original mirror symmetry is nonsymmorphic this is already enough to conclude in analogy to Eq. (2) that there must be an odd number of nodal lines crossing every other gap, which are movable in the sense that their position is parameter-dependent [21,22]. Other cases of nodal lines include higher-fold nodal lines or almost movable nodal lines, which are only pinned to a finite number of high-symmetry points [27,29].

For all of these nodal lines, the Chern number vanishes because of the mirror symmetry, when calculated on a surface that fully encloses the nodal line [78]. It comes to no surprise that despite the extensive research on various types of nodal lines, no example of a stable *chiral* nodal line, i.e., a nodal line with Chern number, has been discussed so far. Nevertheless, there are some reports of such nodal lines without mirror symmetry in the literature, which are either of unclear symmetry protection [79] or as in the case of the nodal lines in hexagonal AgF₃ [80] have found to be actually weakly gapped [37]. Whether a chiral nodal line can exist is not only of interest due to its unique topology, but also important for the study of enforced topological nodal planes. To rigorously deduce the existence of the latter, one needs to assume that a chiral nodal line does not exist. In this case, a nonzero sum of Weyl point chiralities within the Brillouin zone, implies a charged nodal plane, see Sec. IV B 1.

In this section, we aim to answer, whether chiral nodal lines can be stabilized by crystalline symmetries, and we will extensively apply the rotation symmetry constraint of Eq. (1). Doing so we consider points in reciprocal space lying away from any (glide) mirror planes. To approach the first goal,

let us assume that we have obtained a nodal line at a generic position in the Brillouin zone with a chirality $\nu_{\text{line}} < n$, where n is the order of the highest rotation symmetry. Suppose in this gedankenexperiment that we introduce all symmetry-allowed perturbations to the system to gap out the chiral nodal line. Since the nodal line is assumed to be chiral, its topological charge has to persist in the form of Weyl points. However, as long as the original rotation symmetry is preserved, the condition $\nu_{\text{line}} < n$ implies that a nodal line can not be gapped, because the number of resulting Weyl points at generic positions would be equal to ν_{line} and thus incompatible with the required multiplicity n . Unlike nodal lines protected by a \mathbb{Z}_2 invariant, shrinking the nodal line to a point would not remove it, but leave a Weyl point with the same topological charge behind.

Yet, despite this argument to stabilize a chiral nodal line, we will discuss in the following that the relation between rotation symmetry eigenvalues and the chirality, see Eq. (1), strongly limit the possibility to find any nodal band feature fulfilling $\nu_{\text{line}} < n$.

First, suppose there is a nodal line encircling an n -fold rotation axis. Then, we can enclose the whole line by a sphere analogously to Fig. 1(a), which implies by the arguments given in Sec. III A that the chirality of all band crossings enclosed by the sphere is related to the change of rotation eigenvalues on the north and south pole of the rotation axis $\Delta\varphi_b$. Several cases must be distinguished. If there is no additional point crossing on the rotation axes, then $\Delta\varphi_b = 0$ leading to $\nu_{\text{line}} = 0 \pmod{n}$, implying that the nodal line is trivial or at least unstable. If there are indeed additional point crossings on the rotation axis, then $\Delta\varphi_b \neq 0$ and one may choose the sphere to enclose only the point crossings, which implies that these crossings by themselves are responsible for the charge of $\Delta\varphi_b \frac{n}{2\pi} \pmod{n}$, which would be observed on the original sphere. In both cases, the chiral nodal line is unstable.

To circumvent the objections, one may consider more intricate configurations of nodal lines. If one examines a nodal line that is sufficiently extended such that it can not be enclosed by a sphere, it is generally still possible to find a surface to enclose the line and a section of the rotation axis. The proof of Eq. (1) can then be repeated for this new surface, after the subdivision of the integration surface for the Berry curvature, the edges must be related by symmetry, see also Ref. [55], where the integration surface intersects more than one rotation axis. Ultimately, one finds an expression depending on the changes of eigenvalues of the different rotation axes, but the symmetry representation only changes when traversing the integration contour if a crossing on a rotation axes has been enclosed. Thus either the nodal line itself has crossed a rotation axes and is responsible for the exchange of symmetry eigenvalues, such that the nodal line can be gapped out except at a set of corresponding point crossings on the rotation axes, or there will be no exchange of symmetry eigenvalues and hence at most a trivial charge. In Appendix D, we discuss the case of antiunitary symmetries of higher multiplicity and show that they do not circumvent the result obtained above from Eq. (1). In summary, we find that all configurations of chiral nodal lines discussed here do not fit to the original proposal of a topological charge $\nu_{\text{line}} < n$, hence we find that no *crystalline* symmetry is able to protect a chiral nodal line. Note, a chiral

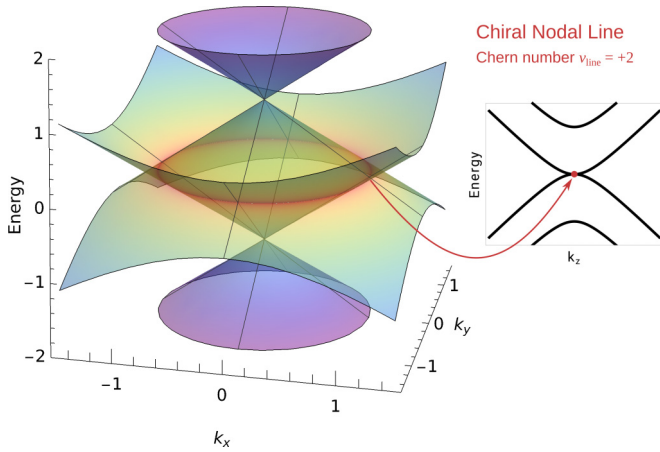


FIG. 4. *Chiral nodal line.* Band structure for the model chiral nodal line (red highlighting) described by Eq. (61). The dispersion of the nodal line is linear (quadratic) in radial (k_z) direction.

nodal line may still be found by considering systems with internal symmetries.

To conclude this section, we propose a low-energy model of a chiral nodal line to illustrate how our above symmetry argument can be circumvented. In this construction, we place two Weyl points, $W(\mathbf{k}, \epsilon)$, of different energy at the origin and couple them by the matrix $B(\mathbf{k})$ in a way that preserves an internal symmetry U_{line} . We define

$$W(\mathbf{k}, \epsilon) = \mathbf{k} \cdot \boldsymbol{\sigma} + \epsilon \sigma_0, \quad (61)$$

$$B(\mathbf{k}) = k_z \sigma_1, \quad \text{and} \quad (62)$$

$$H(\mathbf{k}) = \begin{pmatrix} W(\mathbf{k}, \epsilon) & B(\mathbf{k}) \\ B(\mathbf{k})^\dagger & W(\mathbf{k}, -\epsilon) \end{pmatrix}, \quad (63)$$

where we set the energy offset to $\epsilon = 1$, $\boldsymbol{\sigma}$ is the vector of Pauli matrices, and σ_0 denotes the two-dimensional unit matrix. The bands of the Weyl points intersect in a nodal sphere [81] and are gapped by $B(\mathbf{k})$ except at $k_z = 0$, see Fig. 4 for the resulting band structure. This model exhibits a chiral nodal line with a Chern number of $\nu_{\text{line}} = 2$, which is inherited from the interplay of two $\nu = +1$ Weyl points. It has to be noted that the charge of such a nodal line does also depend on the hybridization away from $k_z = 0$, e.g., for $B(\mathbf{k}) = k_z \sigma_3$ the nodal line is not charged. While $\mathbf{k} \cdot \boldsymbol{\sigma}$ exhibits a fourfold rotation symmetry $U(C_4) = (\sigma_0 + i\sigma_3)/\sqrt{2}$, this symmetry extended to $H(\mathbf{k})$ is broken by $B(\mathbf{k})$ for $k_z \neq 0$. Yet, perturbations that preserve the $U(C_4)$ at $k_z = 0$ symmetry gap out the nodal line, because the nodal line is not pinned to the $k_z = 0$ plane and loses its symmetry protection once moved away despite $\nu_{\text{line}} < n$. Nevertheless, there is an orbital symmetry in our model, namely,

$$U_{\text{line}} = \begin{pmatrix} 1 & 0 & 0 & 0 \\ 0 & 1 & 0 & 0 \\ 0 & 0 & -1 & 0 \\ 0 & 0 & 0 & -1 \end{pmatrix}, \quad (64)$$

which fulfills $[H(\mathbf{k}), U_{\text{line}}] = 0$ at $k_z = 0$ and does not act as a mirror symmetry for $k_z \neq 0$. Two bands with the $+1$ and -1

eigenvalues of U_{line} exchange at the chiral nodal line. Thus any perturbation that respects the symmetry U_{line} may deform the nodal line, but can not introduce a gap. Such a chiral nodal line could be realizable for example in optical metamaterials or other synthetic systems.

B. Applications and extensions of the global constraint

The global constraint contains the information on the possible numbers of crossings on rotation axes or mirror planes. This is for example a guide to the search for semimetals with few point or line crossings [27]. In this section, we combine both constraints and the Nielsen-Ninomiya theorem [50]. First, we will discuss a *paramagnetic* space group with an enforced topological nodal plane duo. Secondly, we illustrate the constraints with a real band structure including accidental Weyl points, nodal planes, and multifold crossings.

1. Symmetry-enforced topological nodal planes

In the following section, we apply local and global constraints to the theory of symmetry-enforced topological nodal planes. After a brief summary of the basic arguments that lead to (topological) nodal planes, we consider the nontrivial case of SG 94 $P4_22_12$. Although there are other space groups that host two nodal planes [28], which can be topological but are not enforced to Ref. [14], this space group is the only known case with two symmetry-enforced topological nodal planes in a paramagnetic space group, i.e., in a grey group including time reversal as a symmetry element.

We consider nodal planes as twofold degeneracies on the surface of the Brillouin zone. Such degenerate planes can be symmetry-enforced by the combined symmetry comprising time-reversal T and a twofold screw rotation \tilde{C}_2 [11,12,14,82]. In short, the antiunitary symmetry $T\tilde{C}_2$ fulfills Kramers theorem at every point on a plane in the Brillouin zone. Regions that host nodal planes are described by $k_i = \pi$ in units of the corresponding inverse lattice constant and have to be at the surface of the Brillouin zone. This gives rise to a natural distinction based on the number nodal planes (one, two, or three) or equivalently distinct symmetries $T\tilde{C}_2$ with eligible planes in the Brillouin zone. We refer to the case of two (three) nodal planes as nodal plane duo (trio) to highlight that these nodal planes form a single connected object that can only be assigned a single Chern number.

The whole gapless structure of nodal planes may exhibit a nonzero Chern number on a surface that encloses the plane, if mirror and inversion symmetries are absent. For nodal plane trios, i.e., nodal planes at $k_i = \pi$ with $i \in \{x, y, z\}$, a single Kramers Weyl point at the TRIM Γ can only be compensated by an opposite charge on the nodal planes, where one needs to consider the case of spinful time-reversal symmetry [11,12]. For nodal plane duos, a similar argument would result in two Kramers Weyl points that might cancel, hence it is a priori unclear, whether nodal plane duos may be nontrivial.

A topological nodal plane duo can, for example, occur due to the global constraint in a time-reversal broken state. The simplest case is realized in ferromagnetic MnSi with the magnetic space group $19.27 P2'_12'_12'_1$. Since the planes $k_x = \pi$ and $k_y = \pi$ exhibit a nodal plane duo, only the twofold rotation axis through Γ is not part of a nodal plane. On this axis, the

global constraint takes the form

$$\sum_{c_b} \Delta\varphi_{b,c_b} = -b \cdot \pi \pmod{2\pi}, \quad (65)$$

which results in an odd number of crossings for bands with odd b . Since each crossing exhibits a charge of $\nu = \pm 1$, cf. Eq. (1), there is an odd overall charge within the Brillouin zone that can not be compensated by generic crossings of even multiplicity. Thus the nodal plane duo is topological with a charge of $\nu_{\text{NP}} = 1 \pmod{2}$, see Ref. [14].

Finally, we consider the topological nodal plane duo enforced by SG 94 $P4_22_12$ for a spinful description with time-reversal symmetry. Again, the global constraint gives a nonzero sum of phase jumps for odd b along the fourfold rotation axis $Z\text{-}\Gamma\text{-}Z$. Here, one needs the local constraint, because it is insufficient to count the number of Weyl points, which may occur as single and double Weyl points. One finds

$$\nu_{Z\text{-}\Gamma\text{-}Z} \equiv \sum_{c_b} \nu_{c_b} = \sum_{c_b} \frac{n}{2\pi} \Delta\varphi_{b,c_b} = -2b \pmod{4}, \quad (66)$$

where the global and local constraints, Eqs. (1) and (2), have been substituted into the sum of all crossings on the fourfold rotation axis with $m = 2$ and $n = 4$. Thus, for odd b , the Chern number of the nodal plane duo $\nu_{\text{NP}} = -\nu_{Z\text{-}\Gamma\text{-}Z} \neq 0$ independently of the details of the system.

To illustrate these results we have devised a Hamiltonian of SG 94, see Appendix E. This model has a minimal set of four connected bands with symmetry-enforced hourglass band structures along $\Gamma\text{-}Z$ and $\Gamma\text{-}X$, see Fig. 5(a), and two nodal planes covering the surfaces defined by $k_x = \pi$ or $k_y = \pi$. The chiralities of Weyl points on the axis $\Gamma\text{-}Z\text{-}\Gamma_2$ follow our local constraint Eq. (1), see Fig. 5(b). As predicted the nodal planes are topologically charged. For example, for the lowest band, the chiralities $\nu_{1,1} = \nu_{1,2} = -1$ at Γ and Z , respectively, add up and are also not compensated by charges at generic positions, see Fig 5(c). Thus the lower nodal plane duo carries the opposite Chern number $\nu_{1,\text{NP}} = +2$. This concludes our discussion of the nodal planes in SG 94, which is the only known space group that enforces a duo of topological nodal planes without magnetism.

As final result regarding the topology of SG 94, it is no coincidence that the two fourfold double Weyl points at A and M, see Fig. 5, carry each the same chirality of $\nu = +2$. To see this, let us assume the screw rotation \tilde{C}_2^x of SG 94 is broken such that there is an arbitrarily small finite gap at the nodal planes. It turns out that now for the twofold degeneracies at TRIMs M and A the signs of the chiralities are fixed by the order of rotation eigenvalues. Yet, together with the global constraints one can reach a broader statement. One can conclude in this symmetry-reduced case that analogously to Eq. (66) the total charge on the axis $M\text{-}A\text{-}M$ is $\nu_{M\text{-}A\text{-}M}^x = 2 \pmod{4}$ with $b = 1$. Since the symmetry $T\tilde{C}_2^x$ preserves the charges while increasing the degeneracy forming the nodal plane, one finds that the non-Abelian charge $\nu_{M\text{-}A\text{-}M} = 4 \pmod{8}$ on the axis is twice as large as the symmetry-reduced case studied above. If there are just the crossings at M and A, as shown in Fig. 5, this implies that they carry the same charge of $\nu = +2$.

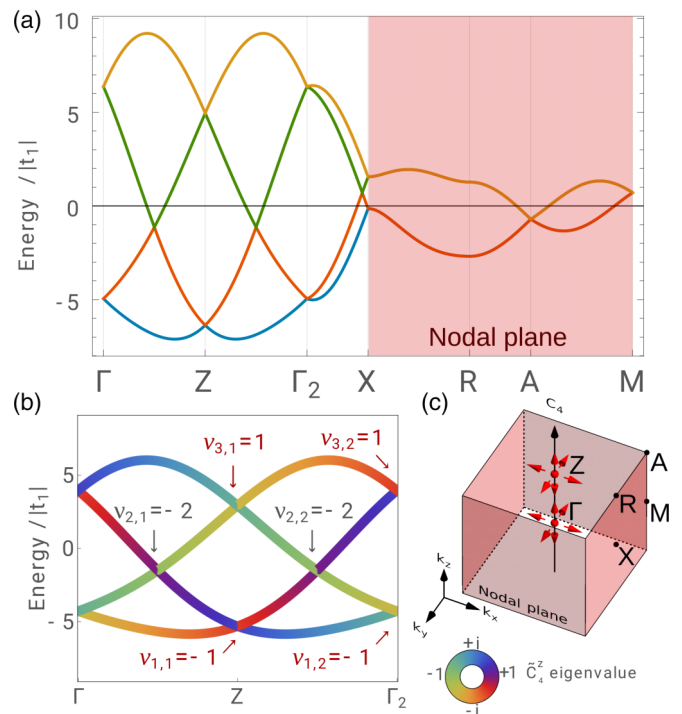


FIG. 5. *Tight-binding model of SG 94.* (a) Band structure of the model defined in Eq. (E1). (b) Symmetry eigenvalues of the fourfold screw rotation \tilde{C}_4 along the full rotation axis $\Gamma\text{-}Z\text{-}\Gamma_2$. The chiralities ν noted in red are compensated by an opposite charge contained within the nodal plane shaded in red in (a) and in the Brillouin zone (c). In (c), the arrows show the well-localized regions of diverging Berry curvature associated to the point crossings at Γ and Z .

2. Global constraints for multifold degeneracies

While in the previous example the absence of a multifold crossing simplified the exposition, we are going to consider in the following the opposite case, where several multifold crossings occur and local and global constraints may not directly substituted into each other. The salient difference is that at multifold crossings the exchange of bands described by $\Delta\varphi$ may occur with lower (or higher bands) that are not necessarily adjacent to the considered band, i.e., not only bands $b - 1$ (or $b + 1$).

To illustrate the constraints with multifold crossings in a real band structure we discuss the cubic compound BaAsPt (SG 198 $P2_13$) exhibiting an unusual multifold crossing point including a $\nu = 5$ band. The material will be closer examined in Sec. VIA.

Here, our goal is to give some intuition on how the global constraint is fulfilled, while respecting the Nielsen-Ninomyia theorem. For the latter, one may pick in principle any subset of bands to determine the relevant chiralities of crossings by the non-Abelian generalization of the Chern number for this set of bands. Here, we consider for simplicity only the band b' that bounds the light red shaded area in Fig. 9 from below.

Since we encounter multi-band crossings, e.g., at Γ , M, and R, we have to use the general form of the global constraint introduced in Eq. (49). It implies that each twofold rotation axis should exhibit a total phase $\sum_{c_{b'}} \Delta\varphi_{b',c_{b'}} = \pi \pmod{2\pi}$, whereas the symmorphic threefold rotations require a phase

change of $\sum_{c_{b'}} \Delta\varphi_{b',c_{b'}} = 0 \pmod{2\pi}$. Note that in Eq. (49) the summations include crossings to lower and to higher bands on the considered rotation axis.

One half of the threefold rotation axis Γ -R, cf. points Fig. 9, exhibits three Weyl points to higher and three to lower bands together with multifold crossings at Γ and R (one of the latter is in close proximity to Γ). Since between each two crossing on Γ -R there is a crossing in the next lower gap, all crossings to the higher (lower) band have an identical phase jump $\Delta\varphi$ and the numerical calculation yields $\Delta\varphi = +2\pi/3$ ($-2\pi/3$). When taking the position relative to band b' into account all five Weyl points thus contribute $\nu = +1$. As a side remark, the lower crossing of charge $\nu = -1$ in the inset appears together with three generic Weyl points with $\nu = +1$ in its close proximity. Due to their close proximity, we have labeled the crossing on the Γ -R axis with the total charge of the four crossings next to the rotation axis, i.e., $\nu = +2$ for the band that bounds the light red shaded region from below. While these generic crossings are not symmetry-enforced similar arrangements of crossings around a threefold rotation axis have been predicted before in an analysis of CoSi, which has the same SG 198 [15]. For the full threefold axis Γ -R, there are 12 phase jumps adding up to a phase shift of $\Delta\varphi = +24\pi/3 = 0 \pmod{2\pi}$. The multifold crossings at Γ and R exhibit $\Delta\varphi = \pm 2\pi/3$ such that in total the phase equals $0 \pmod{2\pi}$ on each threefold rotation axis. In total, the band b' comprises thus 48 Weyl points of charge $\nu = +1$ on generic points of its threefold rotation axes.

On the twofold rotation axis along Γ -X, there is one crossing contributing $\Delta\varphi = \pi$. Since Γ and X are time reversal invariant and the twofold rotation eigenvalues are complex at Γ and real at X, it is clear prior to any calculation that the phase changes at Γ but not at X. Thus a full twofold rotation axis X - Γ - X exhibits an odd number of phases as expected. Overall there are six Weyl points of $\nu = +1$ on the twofold axes through Γ . The twofold bands on the nodal planes along the R-M line exhibit two distinct representations that are characterized by twofold rotation eigenvalues like on Γ -X, thus also here the global constraint applies. On R-M, there is a crossing to a lower band as well as a pinned crossing at M, both exhibit an exchange of C_2 eigenvalues, whereas none occurs for the crossing at R. Thus, along the full line R-M-R, there is an odd number of crossings fulfilling the global constraint. Although we encounter chiral crossings on R-M, these do not contribute with a Chern number to the band b' , because these crossings lie completely below the light red shaded gap. Note, to determine that the sixfold crossing at R contributes the charge $\nu = -4$ to the band b' , one needs to determine a non-Abelian Chern number, see also Ref. [15] for the details of such a calculation. Finally, to apply the Nielsen-Ninomiya theorem to band b' , one has to consider the contribution by the nodal plane of $\nu = 3$.

In summary, the chiral charges on the band b' that bounds the light red shaded region from below are $6\nu_{b',\Gamma-X} = 6$, $8\nu_{b',\Gamma-R} = 48$, as well as $\nu_{b',\Gamma} = -5$, $\nu_{b',R} = -4$, and $\nu_{b',NP} = +3$, which adds up to 48. By using the Nielsen-Ninomiya theorem for band b' , we can infer that there are at least two sets of Weyl points at generic positions. Indeed, by a closer inspection of the band structure we find that there are additional Weyl points close to the Γ -R axes. There are 24 of such

Weyl points with charge $\nu = -1$ in the vicinity R as well as another set of Weyl points with also $\nu = -1$ close to Γ .

While we had to consider the charge of the nodal plane explicitly, in absence of nodal planes it is possible to infer the existence of Weyl points at generic positions based on symmetries alone, e.g., in a spinful representation of SG 19 or the magnetic SG 19.27 for the movable fourfold double Weyl points as noticed for a tight-binding model in Refs. [11,14]. It is thus possible to use the local and global constraints together with the Nielsen-Ninomiya theorem to deduce the existence of Weyl points at generic positions within the Brillouin zone.

V. GENERATION AND CLASSIFICATION OF LOW-ENERGY HAMILTONIANS FOR THE MULTIFOLD CROSSING CASE

As we have already seen in a previous Sec. IV A 2, combinations of different symmetries, including time-reversal, can lead to surprising results. Up until now, we considered only Weyl points. So the next question is how the non-Abelian constraints affect multifold crossings in this regard. Here we do not only want to restrict ourselves on just the evaluation of constraints, but to explicitly calculate Chern numbers in all topological phases of all multifold crossings, as the solution to constraints derived for the non-Abelian case (see Sec. III B) are not unique and larger Chern numbers than the minimal ones fulfilling the given constraints can, due to the higher symmetry, be no longer excluded. We can see these cases directly when such a topological classification is carried out explicitly.

This complete topological classification of all multifold crossings in all space groups follows a three phase approach. First all irreducible representations (irreps) with dimensions higher than 2 were found at all high-symmetry points using the Bilbao Crystallographic Server [83]. Since we included time-reversal symmetry in all of our analysis, the search can be restricted to double space groups with broken inversion symmetry, since only there topological charges are allowed to be nonzero in presence of time-reversal symmetry. Then, low-energy Hamiltonians were generated for all irreps found in the last step, such that these Hamiltonians respect all symmetries at the given high-symmetry points. Finally, the whole parameter space of these Hamiltonian are topologically classified.

We note that there is an alternative approach for generating low-energy Hamiltonians than the one shown in this section based on Ref. [32], where all possible Hamiltonian terms are tabulated. We used the method described here, since we found it more convenient to lookup a small number of symmetry generators and their representations instead of all possible Hamiltonian terms. See also Refs. [84–86] for more alternative algorithms.

A. Automatic generation of low-energy Hamiltonians from irreps

A general low-energy Hamiltonian up to second order in wave vector k has the following form:

$$H_{nm}(\mathbf{k}) = \sum_{hp_1} \alpha_{h,1} H_{hp_1nm}^1 k_{p_1} + \sum_{hp_1p_2} \alpha_{h,2} H_{hp_1p_2nm}^2 k_{p_1} k_{p_2} + \mathcal{O}(k^3). \tag{67}$$

Here n and m enumerate the degrees of freedom. $\alpha_{h,q}$ are the free parameters of H at order q . $H_{hp_1\dots p_qnm}^q$ are the linearly independent terms in H , with h indexing each term. The goal of the following algorithm is to compute these terms, such that H is symmetric under some group of symmetries.

The starting point of the automatic generation are symmetry generators and the corresponding irrep at a given high-symmetry point. With these generators we build up the whole little group G at this high-symmetry point and the representation $D(g)$ of those symmetries $g \in G$. The only constraint of a low-energy Hamiltonian at this point must be that it is symmetric

$$\forall g \in G : H(g\mathbf{k}) = D(g)H(\mathbf{k})D(g^{-1}). \quad (68)$$

We can symmetrize the Hamiltonian in Eq. (67) via

$$\tilde{H}_{hv_1ij}^1 = \frac{1}{|G|} \sum_{g \in G} g_{v_1p_1}^{-1} D(g)_{in} H_{hp_1nm}^1 D(g^{-1})_{mj}, \quad (69)$$

$$\tilde{H}_{hv_1v_2ij}^2 = \frac{1}{|G|} \sum_{g \in G} g_{v_1p_1}^{-1} g_{v_2p_2}^{-1} D(g)_{in} H_{hp_1p_2nm}^2 D(g^{-1})_{mj}, \quad (70)$$

...

where g_{ab} is the real space representation of g and Einstein notation was used. Then $\tilde{H}_{hp_1\dots p_qnm}^q$ are the new terms of a symmetric H . Note that $D(g)$ can be antiunitary, which is the case when g is, for example, the time-reversal symmetry. In this case, $D(g) = UK$ with U unitary and K being the complex conjugation operator. The latter one can be eliminated by commuting it through all term in Eqs. (69) and (70) until we can use $K^2 = 1$.

The algorithm starts by generating a set of random complex $H_{hp_1\dots p_qnm}^q$ terms, with $h \in \{1, \dots, N\}$ and N being the total amount of randomly generated terms. These are then symmetrized via Eq. (69) to produce N symmetrized $\tilde{H}_{hp_1\dots p_qnm}^q$ terms. Only the linearly independent terms are kept, which is done using a Gram-Schmidt orthogonalization, during which the terms indexed by h are treated as vectors by flattening indices $p_1 \dots p_qnm$ to a single index I . This also reduces the number of terms $\tilde{N} \leq N$ to the maximal set of symmetric and linearly independent terms. The number of free parameters of this Hamiltonian at order q is also \tilde{N} .

For better handling of these terms, we would like to normalize the real or imaginary part of as many of their entries to 1, since they are still filled with random numerical values of arbitrary magnitude. We can not normalize all entries to 1, since not all are linearly independent. This normalization is done by first gathering all nonzero columns in $\text{Re}(\tilde{H}_{hl}^q)$ and $\text{Im}(\tilde{H}_{hl}^q)$ in a new matrix M_{hr} with size (\tilde{N}, P) , with P the number of nonzero columns. Rows that are linearly dependent on other rows are removed in M , such that M is quadratic and invertible. The final terms of H are then computed with

$$H_{h'p_1\dots p_qnm}^{q'} = \sum_h M_{h'h}^{-1} \tilde{H}_{hp_1\dots p_qnm}^q. \quad (71)$$

Due to the inversion of M , the real or imaginary part of all nonzero entries in \tilde{H} , which are chosen to build up the M matrix, are normalized to 1 in only one of the terms while they are set to 0 in all other. Entries that are not part of the final M are either a fraction or a fraction consisting of square roots. The

last step of the algorithm is to convert the numerical values of H' into analytical expressions by comparing the entries to the values of those analytical expressions and also to project H' to Pauli or Gellmann matrices. To test if this conversion worked, the symmetry of the resulting Hamiltonian is checked.

B. Classification of all multifold crossings at high-symmetry points

Using the algorithm described in the previous section, a Hamiltonian for each irrep with dimension >2 was generated. Since we only want to study the topological charge of the crossing at the high-symmetry point in question, it is sufficient, with only one exception as we will see later, to generate only the terms up to linear order in k , since higher orders could only produce additional crossings away from the high-symmetry point and do not alter the topological charge of the multifold crossing. Some of the generated Hamiltonian are equivalent or equivalent up to a transformation, so these cases can be grouped and classified together. The transformations either have no effect on or flip the topological charge.

The determination of every band's topological phase diagrams of the Hamiltonians all follow the same idea of first finding all points in parameter space where the current band in question of the given Hamiltonian becomes gapless away from the crossing. These are the only points where topological phase transitions can happen, i.e., the topological charge of the multifold crossing can change. These points make up subspaces in parameter space, which separate different topological phases and were found by considering the characteristic polynomial of H and comparing it to a characteristic polynomial describing a Hamiltonian in a gapless phases.

So after finding these subspaces it is possible to determine the topological charges of every phase by evaluating it numerically deep in a given phase. This way one can color in the whole phase by the determined topological charge. Since no other topological phases are possible, we can enumerate all possible topological charges for all multifold crossings.

During this topological classification, the Chern number of single bands is sometimes undefined. This happens due to band degeneracies, for example nodal planes, which by symmetry persist to all orders in \mathbf{k} . In most of these cases, one can still define a non-Abelian Chern number, see Eq. (12). In the case of fourfold crossings on nodal planes, we compute non-Abelian Chern numbers $\nu_{b,b+1}$, where bands b and $b+1$ are part of the nodal plane.

1. Fourfold crossings

The main results for all fourfold crossings are summarized in Tables I and II. The topological charge of the lowest band ν_1 is undefined in most irreps, since there the lowest two bands can be shown to be always twofold degenerate at some k points away from 0 at all orders in \mathbf{k} due to symmetry constraints. Where this is not the case, an unusually high Chern number of ± 5 can be observed.

As this result is quite unexpected, we explicitly show the topological phase diagram and its derivation of one of the two Hamiltonians, the model for the $\bar{\Gamma}_6\bar{\Gamma}_7$ irrep, that describe these cases. This irrep can be found in SG 195-199. The little group contains $C_2^{x,y,z}$, $C_3^{(\pm 1, \pm 1, \pm 1)}$, and time-reversal symmetry. In the

TABLE I. All possible topological charges of all fourfold crossings in the spinless case (without SOC). Their Hamiltonians are either listed under the Model column or are obtained after a possible transformation applied on the given Hamiltonian.

SG	Irrep	ν_1	ν_2	ν_{12}	Model	Transformation
19	R_1R_1	-	-	± 2	G9	-
92	A_1A_2	-	-	± 2	G7	$k_x \rightarrow k_y, k_y \rightarrow -k_x, \alpha_2 = 0, \alpha_3 = 0$
96	A_1A_2	-	-	± 2	G7	$k_y \rightarrow -k_y, \alpha_2 = 0, \alpha_3 = 0$
198	R_1R_3/R_2R_2	-	-	± 2	G5	-
212/213	R_1R_2	-	-	± 2	G5	-
212/213	R_3	-	-	± 2	G6	-

following, all used representations are equivalent to the ones on the Bilbao Crystallographic Server [83]. The Hamiltonian generated by the algorithm described in the previous section is

$$\begin{aligned}
 H = & \alpha_0[2k_x\sigma_x\tau_z + k_y(-\sqrt{3}\sigma_x\tau_0 - \sigma_y\tau_0) \\
 & + k_z(\sigma_x\tau_x + \sqrt{3}\sigma_y\tau_x)] \\
 & + \alpha_1[-2k_x\sigma_y\tau_z + k_y(-\sigma_x\tau_0 + \sqrt{3}\sigma_y\tau_0) \\
 & + k_z(\sqrt{3}\sigma_x\tau_x - \sigma_y\tau_x)] \\
 & + 2\alpha_2[k_x\sigma_z\tau_x + k_y\sigma_0\tau_y + k_z\sigma_z\tau_z] \quad (72)
 \end{aligned}$$

with τ and σ being Pauli matrices. It is possible to show (see Appendix G 1) that the Hamiltonian is only gapless for $\alpha_2 = \pm\sqrt{\alpha_0^2 + \alpha_1^2}$, $\alpha_2 = 0$ or $\sqrt{\alpha_0^2 + \alpha_1^2} = 0$ at points away from $k = (0, 0, 0)$. We can assign the spaces in between gapless planes in parameter space α_n with precomputed Chern numbers to arrive at the topological phase diagram of the $\Gamma_6\Gamma_7$ irrep model. See Fig. 6 for the phase diagram for band 2. We find that band 1 has two phases, for $\alpha_2 < 0$ the Chern number is $\nu_1 = -3$, for $\alpha_2 > 0$ it is $\nu_1 = 3$. For bands 3 and 4, $\nu_3 = -\nu_2$ and $\nu_4 = -\nu_1$.

In the Appendix of Ref. [73], a symmetry equivalent Hamiltonian to Eq. (72) has been derived, although there the whole topological phase diagram has not been mapped out. Previously [17], this fourfold crossing has been described by a Rarita-Schwinger-Weyl spin-3/2 Hamiltonian [87–89] $H(\mathbf{k}) = \alpha\mathbf{S} \cdot \mathbf{k}$, which only supports the $\nu_n = \{\pm 3, \pm 1, \mp 1, \mp 3\}$ phase, or a distinction between the 3/2 chiral fermion and the one found here was made [90] but only the $\nu_2 = \pm 1$ phase was considered. Here we see that this description is incomplete. To our knowledge, the $\nu_n = \{\pm 3, \mp 5, \pm 5, \mp 3\}$ topological phase has not been observed yet.

We find no threefold symmetry eigenvalue phase jumps for the lowest/highest band. A phase jump of $2\pi/3$ for $\alpha_2 < 0$ and of $4\pi/3$ for $\alpha_2 > 0$ was observed for band 2. For all bands, a phase jump of π was found for both twofold symmetries, which constraints all Chern numbers to be odd $\nu_n = 1 \pmod 2$. Further, the threefold symmetry constraints the Chern number of the lowest and highest bands to $\nu_{1/4} = 0 \pmod 3$, which is consistent with $\nu_{1/4} = \pm 3$. Then, for $\alpha_2 < 0$, we have the constraint $\nu_{2/3} = 1 \pmod 3$ and for $\alpha_2 > 0$, we have $\nu_{2/3} = 2 \pmod 3$, which are fulfilled in all phases in Fig. 6.

TABLE II. All possible topological charges of fourfold crossings in all spinful SGs and their Hamiltonians.

SG	Irrep	ν_1	ν_2	ν_{12}	Model	Transformation
18	$\bar{S}_5\bar{S}_5/\bar{R}_5\bar{R}_5$	-	-	± 2	G3	-
19	$\bar{S}_5\bar{S}_5$	-	-	± 2	G3	-
19	$\bar{T}_5\bar{T}_5$	-	-	± 2	G3	$k_x \rightarrow k_y, k_y \rightarrow k_z, k_z \rightarrow k_x$
19	$\bar{U}_5\bar{U}_5$	-	-	± 2	G3	$k_y \rightarrow k_z, k_z \rightarrow k_y$
90	$\bar{A}_6\bar{A}_7/\bar{M}_6\bar{M}_7$	-	-	± 2	G7	-
92/94/96	$\bar{M}_6\bar{M}_7$	-	-	± 2	G7	-
92/96	$\bar{R}_5\bar{R}_5$	-	-	± 2	G3	$k_x \rightarrow k_y, k_y \rightarrow k_z, k_z \rightarrow k_x$
92/96	$\bar{A}_7\bar{A}_7$	-	-	± 4	G8	-
94	$\bar{A}_6\bar{A}_7$	-	-	± 2	G7	$k_x \leftrightarrow k_y$
195/196/197/198/199	$\bar{\Gamma}_6\bar{\Gamma}_7$	± 3	$\pm 1, \mp 5$	$\pm 4, \pm 2$	VB1	-
195	$\bar{R}_6\bar{R}_7$	± 3	$\pm 1, \mp 5$	$\pm 4, \pm 2$	VB1	-
197	$\bar{H}_6\bar{H}_7$	± 3	$\pm 1, \mp 5$	$\pm 4, \pm 2$	VB1	-
198	$\bar{M}_5\bar{M}_5$	-	-	± 2	G3	-
199	$\bar{H}_6\bar{H}_7$	± 3	$\pm 1, \mp 5$	$\pm 4, \pm 2$	VB1	$U = \sigma_z\tau_x$
207/208/209/210 /211/212/213/214	$\bar{\Gamma}_8$	± 3	$\pm 1, \mp 5$	$\pm 4, \pm 2$	G2	-
207/208	\bar{R}_8	± 3	$\pm 1, \mp 5$	$\pm 4, \pm 2$	G2	-
211	\bar{H}_8	± 3	$\pm 1, \mp 5$	$\pm 4, \pm 2$	G2	-
212	$\bar{M}_6\bar{M}_7$	-	-	± 2	G4	-
213	$\bar{M}_6\bar{M}_7$	-	-	± 2	G4	$k_y \rightarrow -k_y$
214	\bar{H}_8	± 3	$\pm 1, \mp 5$	$\pm 4, \pm 2$	G2	$U = \sigma_0\tau_x, \alpha_1 \rightarrow -\alpha_1$

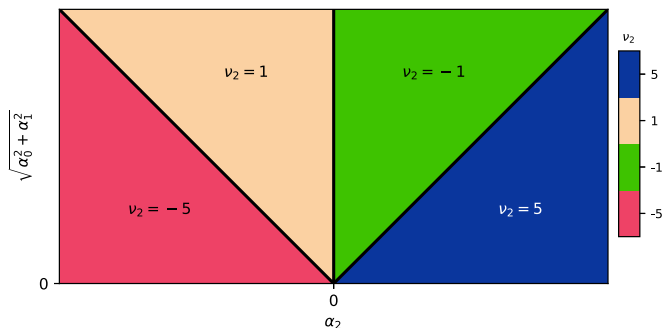


FIG. 6. Topological phase diagram of the fourfold crossing described by Hamiltonian (72) with three parameters α_0 , α_1 and α_2 . Depicted is the Chern number ν_2 of band 2. An unusually high absolute Chern number of 5 can be found in regions where $\alpha_2 > \sqrt{\alpha_0^2 + \alpha_1^2}$ or $\alpha_2 < -\sqrt{\alpha_0^2 + \alpha_1^2}$.

The transition between $\nu_2 = \pm 1$ and $\nu_2 = \mp 5$ phases is facilitated (see Appendix G 1) by a gap closing of the middle two bands. This suggests, that the mechanism behind this Chern number switch is an absorption/emission of six Weyl points on the C_2 invariant axes into/out of the multifold crossing. This implies an exchange of C_2 symmetry eigenvalues of bands 2 and 3 between these two phases, which we confirmed by a direct calculation.

The phase transition ν_n to $-\nu_n$ at $\alpha_2 = 0$ takes place by a simultaneous gap closing on C_2 invariant lines of the outer band pairs (1,2) and (3,4) as well as on C_3 invariant lines of band pair (2,3). Since corresponding symmetry eigenvalues switch on both invariant lines, six WPs on the outer band pairs and eight WPs on the middle band-pair fuse with or emerge from the fourfold crossing. The WPs on C_2 invariant lines with total charge ± 6 switch the sign of the lowest/highest Chern number $\nu_{1/4} = \mp 3 \rightarrow \pm 3$. For the middle, two bands a combined total Chern number of $\mp 6 \pm 8 = \pm 2$ switches the sign of the middle Chern numbers $\nu_{2/3} = \mp 1 \rightarrow \pm 1$.

This means, consecutive topological phase transitions over $\nu_2 = 5 \rightarrow -1 \rightarrow 1$ produce a total of 26 WPs distributed across the three band pairs, six in the lower and upper band pairs respectively and $6 + 8 = 14$ in the middle band pair, provided there are no other crossings at the start in the $\nu_2 = 5$ phase, since these could also be merged into the multifold point to carry out the phase transition. This process is visualized in Fig. 7.

In Fig. 8, the spin texture of this fourfold crossing in the $\nu_2 = -1$ and $\nu_2 = 5$ phase are compared for bands 1 and 2. To extend the discussion of spin textures at multifold crossings [91] to the novel phase of $\nu_2 = 5$, we construct a spin operator for p -orbitals sitting at the 1a Wyckoff position of SG 195. In the presence of SOC, the p energy levels split into the fourfold representation of interest $\bar{\Gamma}_6\bar{\Gamma}_7$ as well as the 2D irrep $\bar{\Gamma}_5$. The parameters chosen for the $\nu_2 = -1$ phase are $\alpha_0 = 0$, $\alpha_1 = 1.6$ and $\alpha_2 = 1$, while for the $\nu_2 = 5$ phase, the parameters are $\alpha_0 = 0$, $\alpha_1 = 1$ and $\alpha_2 = 1.6$. The spin operator was constructed using consecutive diagonalizations of the p -orbital symmetry representation and $\bar{\Gamma}_6\bar{\Gamma}_7 \oplus \bar{\Gamma}_5$ (see Appendix F). We find a significant difference regarding the spin textures of band 2 between $\nu_2 = -1$ and $\nu_2 = 5$ phases. The s_x (so 100) component of the spin expectation value flips

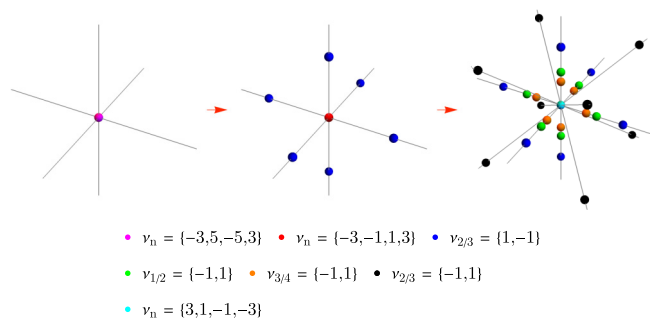


FIG. 7. Starting from a single fourfold crossing described by the $\bar{\Gamma}_6\bar{\Gamma}_7$ irrep model [see Eq. (72)] in the $\nu_2 = 5$ phase, a phase transition to $\nu_2 = 1$ over $\nu_2 = -1$ produces a total of 26 WPs across the three band pairs. WP and multifold point charges are color-coded.

discontinuously when going from the $\nu_2 = -1$ to the $\nu_2 = 5$ phase, see Fig. 8(b). This qualitative difference in the spin texture of multifold crossings belonging to distinct phases is in principle measurable by spin-resolved ARPES experiments [70,72]. In this way, these two topological phases can be distinguished.

2. Threefold and sixfold crossings

The Hamiltonians for threefold and sixfold crossings found by the procedure described above reproduce the ones listed in Ref. [16]. We also find the Hamiltonians for all threefold crossings

$$H = \begin{pmatrix} 0 & k_z(\alpha - i\beta) & -k_y(\alpha + i\beta) \\ & 0 & k_x(\alpha - i\beta) \\ \dots & & 0 \end{pmatrix} \quad (73)$$

to be equivalent up to transformations. Since these transformations and the explicit dependence of the topological charge were omitted in Ref. [16], we included them here in Tables III and IV and in Appendix H.

The sixfold crossing Hamiltonian of SG 198 $\bar{R}_7\bar{R}_7$ irrep is equal to

$$\begin{aligned} H = & \alpha_0[k_x\sigma_z\lambda_7 - k_y\sigma_z\lambda_6 + k_z\sigma_z\lambda_3] \\ & + \alpha_1[k_x\sigma_0\lambda_5 + k_y\sigma_0\lambda_2 + k_z\sigma_0\lambda_1] \\ & + \alpha_2[k_x\sigma_x\lambda_7 - k_y\sigma_x\lambda_6 + k_z\sigma_x\lambda_3] \\ & + \alpha_3[k_x\sigma_y\lambda_7 - k_y\sigma_y\lambda_6 + k_z\sigma_y\lambda_3] \end{aligned} \quad (74)$$

with σ_n and λ_n being Pauli and Gellmann matrices (see Appendix J for a definition). This Hamiltonian is equivalent up to a unitary transformation to the one found in Ref. [16], with $e^{i\phi} = \alpha_0 + i\alpha_1$ and $b = \alpha_2 + i\alpha_3$. There it was also shown that you can arrive at the Hamiltonian for the SG 212 and 213 $\bar{R}_7\bar{R}_8$ irrep by setting $\phi = \frac{\pi}{2}$. Due to nodal planes crossing these points, Chern numbers for odd fillings can not be defined. The non-Abelian Chern number for the middle two bands $\nu_{34} = 0$ remains trivial, while the Chern number for the remaining bands are $\nu_{12} = -\nu_{56} = \pm 4$. The exact phase diagram and its derivation can be found in Appendix I.

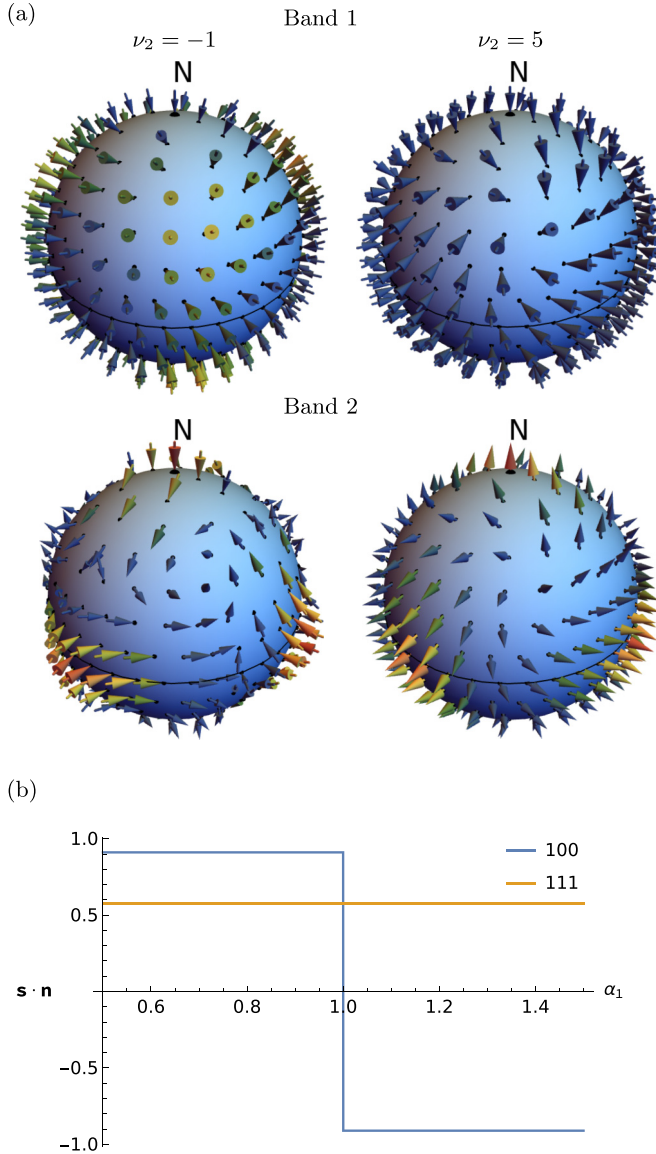


FIG. 8. (a) Spin texture for the fourfold crossing described by Eq. (72) for bands 1 and 2 in the $\nu_2 = -1$ and $\nu_2 = 5$ phases. The arrow size and color depend on the magnitude of the spin, red being maximal. (b) Normal component of the spin expectation value, so $\mathbf{s} \cdot \mathbf{n}$, in 100 (so $\mathbf{n} = (1, 0, 0)$) and 111 direction over the parameter α_1 tuning from the $\nu_2 = 5$ to $\nu_2 = -1$ phase. We see a spin flip from an outside to inside facing spin during this phase transition in the 100 direction, while the spin at 111 is staying constant. See Appendix F for a definition of \mathbf{s} .

VI. MATERIALS

Here we discuss two material examples. Details on the calculations can be found in Appendix L.

A. BaAsPt and related compounds (SG 198)

A material search for a fourfold crossing with a Chern number of 5 sufficiently close to the Fermi energy was done in space groups 195–199 and 207–214. First materials from the materials project [92] are screened for fourfold crossings near the Fermi energy. The Chern number of this point was directly

TABLE III. All threefold crossings without SOC and corresponding transformations, which generate their Hamiltonian from Eq. (73).

SG	Irrep	Transformation
195...199	Γ_4	$\beta \rightarrow -\beta, k_x \rightarrow k_z, k_y \rightarrow -k_x, k_z \rightarrow k_y$
195	R_4	$\beta \rightarrow -\beta, k_x \rightarrow k_z, k_y \rightarrow -k_x, k_z \rightarrow k_y$
197	H_4, P_4	$\beta \rightarrow -\beta, k_x \rightarrow k_z, k_y \rightarrow -k_x, k_z \rightarrow k_y$
199	H_4	$\beta \rightarrow -\beta, k_y \rightarrow -k_x$
207...214	Γ_4, Γ_5	$\alpha = 0, \beta \rightarrow -\beta, k_x \rightarrow k_z, k_y \rightarrow -k_x, k_z \rightarrow k_y$
207, 208	R_4, R_5	$\alpha = 0, \beta \rightarrow -\beta, k_x \rightarrow k_z, k_y \rightarrow -k_x, k_z \rightarrow k_y$
211, 214	H_4, H_5	$\alpha = 0, \beta \rightarrow -\beta, k_x \rightarrow k_z, k_y \rightarrow -k_x, k_z \rightarrow k_y$

computed [15] using density-functional theory, in particular QUANTUM ESPRESSO [93]. This search was stopped at the first material found, which was BaAsPt in SG 198. There a fourfold point with $\nu = \pm 5$ was found at Γ at -100 meV, see Fig. 9. References [94,95] also mention a fourfold degeneracy at Γ in BaAsPt and a related compound BaPt, although no topological classification has been performed and therefore the $\nu = \pm 5$ phase has not been identified. We note that BaAsPt belongs to a class of materials in SG 198, referred to as LaIrSi-type materials [73], consisting of three elements and with similar bandstructures, as seen on the materials project [92]. Due to their similar atomic coordination [96] we expect for this material class the same orbital characteristics as in BaAsPt, such that $\nu = \pm 5$ should also occur there, though likely at varying distances to E_F . We note that, this topological phase can in principle occur in the broad class of B20 materials, and in fact in any compound crystallizing in SG 198.

A full topological classification [15] of the 6 bands crossing E_F has been carried out. We enumerate these bands from 1 to 6 in descending order in energy. The charge of the nodal planes, which occur in SG 198 at the BZ boundary, is shown in Fig. 9 in solid colored lines. The figure also shows all crossings on high-symmetry lines. WPs at generic positions have been found for band pair (4,5) (the band pair with $\nu = \pm 5$ at Γ and whose bandgap is shaded light red) at $\mathbf{k} = 2\pi(-0.0289, -0.2699, -0.2988)^T$ and all symmetry related points with $\nu_5 = -1$. Another generic WP was found at $\mathbf{k} = 2\pi(0, -0.2085, -0.291)^T$ with $\nu_4 = -1$ for band pair (3,4). The fermion doubling theorem is fulfilled when including the topological charges of the WPs, multifold crossings and NPs found by the full topological classification of the six bands crossing E_F .

Further, a large topological band gap shaded in light red separating the two bands with $\nu = \pm 5$ can be seen. A surface DOS calculation at 100 meV shows a large number of Fermi arcs, see Fig. 10, despite a screening of the topological charge from the fourfold point, which due to the filling of this

TABLE IV. All spinful threefold crossings. The Hamiltonian is described in Eq. (73).

SG	Irrep	Transformation
199,214	\bar{P}_7	–

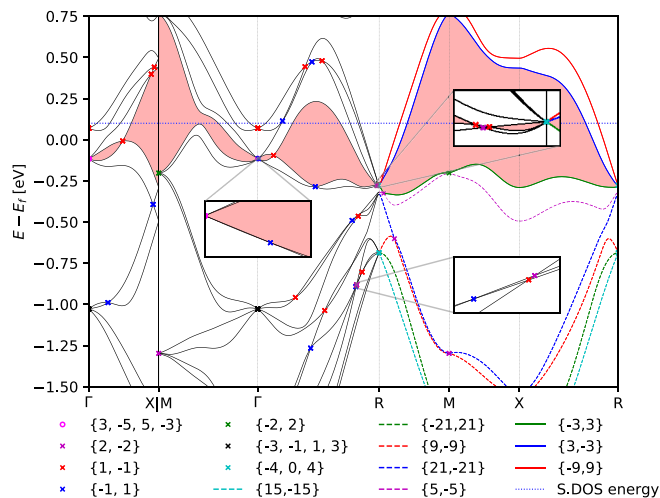


FIG. 9. Band structure of BaAsPt and all band crossings on high-symmetry lines. The bandgap between the bands with a Chern number of ± 5 at the fourfold Γ crossings is indicated by the light red region. This topological bandgap is responsible for the Fermi arcs in Fig. 10. The blue dashed line is the energy slice taken there. We also observe NPs with Chern numbers up to 21 at energies below E_f .

topological band gap is $-3 + 5 = -2$, by charges on Γ -X, which sum up to 2. Four copies of these WPs appear on the projection $\bar{\Gamma}$ - \bar{M} . Very close to the Γ point on the Γ -R line

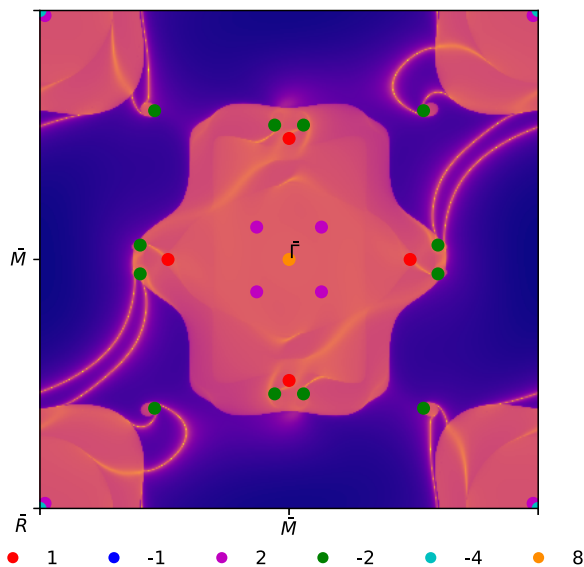


FIG. 10. Surface density of states (DOS) of BaAsPt at 0.1 eV. Also shown are the projected topological charges, relevant to a band-filling in between the bandpair with charge $\nu = \pm 5$ at Γ from the bulk. This band gap corresponds to the parts of the surface DOS without bulk states, where the Fermi arcs reside. With this filling, the charge of the Γ point is $3 - 5 = -2$, which is compensated by two WPs on the Γ -X line. Further, there are 8 WPs on the Γ -R line very close to the Γ point which we included into the total charge of 8 of the projected $\bar{\Gamma}$ point. The total charge of bulk states around $\bar{\Gamma}$ is 4, so there are four Fermi arcs connecting these states to the \bar{R} point with topological charge $\nu = -4$. Note that the $\nu = 2$ charges near \bar{R} are slightly away from \bar{R} , so there are 4 copies at every corner. These charges are connected with 8 Fermi arcs to bulk states with $\nu = -2$ points between $\bar{\Gamma}$ and \bar{R} .

there are eight WPs, which we included into the charge of $\bar{\Gamma}$. The total charge of the bulk bands surrounding $\bar{\Gamma}$ of four give rise to four Fermi arcs emerging from the bulk states at $\bar{\Gamma}$ and running to the \bar{R} point with charge -4 . The remaining Fermi arcs are entirely explained by projected topological crossings of the band pair (4,5), namely, a small pocket between $\bar{\Gamma}$ and \bar{R} containing a charge of -2 and connecting via 2 Fermi arcs to bulk bands with a charge of 2 near \bar{R} . In total, we are counting 12 Fermi arcs.

B. NbO₂ and TaO₂ (SG 80)

Niobium dioxide was first synthesized in 1941 and was shown to crystallize in a rutile structure with tetragonal space group symmetry 136 [97]. Further research revealed the existence of a distorted lower-symmetry phase β -NbO₂ [98]. During the structural transition, pairs of niobium atoms dimerize along the c-axis, and although the nature of the transition is believed to be of Peierls type, the specifics have been the subject of an extensive amount of research throughout the years [99–103]. Slightly sub-stoichiometric single crystals of β -NbO₂ can be synthesized in oxygen-deficient environments, and its crystal structure has space group symmetry 80 [104]. Much later, β -NbO₂ was proposed as a potential realization of a topological chiral crystal with Kramers-Weyl fermions in its bulk and the corresponding boundary modes on its surface [11].

Since the topological band gap in β -NbO₂ is small and the crossing of interest is overshadowed by spectral weight of other bands in its vicinity, we propose two alterations to the compound to improve its usefulness as a topological semimetal. First, to increase the effect of spin-orbit coupling, we consider the hypothetical compound β -TaO₂, which is expected to have the same crystal structure since tantalum and niobium have very similar ionic radii and electron configurations [105]. Second, we enhance the distortion mode that connects the rutile and the reported lower-symmetry phase of NbO₂. To do this, we compare the crystal structures of the parent and the distorted compound, calculate the irreducible representations of the distortions and identify the linear combination of modes that connects the two configurations using the ISODISTORT tool [106]. The computed distortion is then exaggerated by a factor of 1.5, retaining the space group symmetry of β -NbO₂. Potential routes to synthesize the proposed crystal include growing it at higher temperatures or in a more oxygen-deficient environment [104].

The band structure and the surface states of β -TaO₂ are shown in Fig. 11. In the vicinity of the Fermi energy there are two time-reversal-related double Weyl points protected by fourfold rotation symmetry, one of which is seen on the line Γ -M, as well as two double Weyl points pinned to the points labeled P. Our calculation shows that Weyl points on Γ -M with charge $\nu = +2$ compensate the ones at P with $\nu = -2$. To our knowledge, this is the first example, where double Weyl points are enforced away from a TRIM but pinned to a lower symmetry point. These doubly charged degeneracies on a twofold rotation axis contradict previous suggestions that double Weyl points require four- or sixfold rotational symmetry [35], and can only be understood from our argument using the local constraint, see Sec. IV A 1.

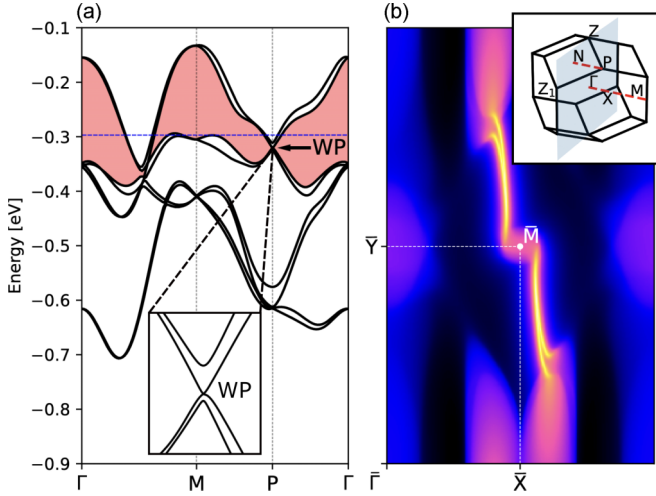


FIG. 11. (a) DFT bulk band structure of the distorted TaO₂ compound with the topological band gap colored in red and an arrow pointing to the Weyl point (WP). The inset is showing a zoom of the double Weyl point. (b) Surface spectral density at -0.297 eV [blue dashed line in (a)] with a termination projecting M onto Γ ($\bar{\Gamma}$) and P onto N (\bar{M}) as shown in the inset. Two Fermi arcs connect the projection of the Weyl point at P with the bulk bands.

VII. CONCLUSION

In this paper, we have derived two fundamental laws of chiral band crossings, namely, a local and a global constraint, that are satisfied by any set of chiral crossings connected by symmetry and topology. We have shown that such sets of band crossings form a *topological network*, whose chiral charges are determined by the fundamental laws. The local constraint relates the chiral charge of the crossing to the phase jump in symmetry eigenvalues (Sec. II A). The global constraint, on the other hand, restricts the number and types of crossings on high-symmetry axes, thereby providing useful *sum rules* (Sec. II B). Together with the famous fermion-doubling theorem by Nielsen and Ninomiya, these laws describe all conditions that networks of chiral band crossings must satisfy and thus give a deeper understanding for their existence.

To demonstrate the usefulness of the fundamental laws, we have applied them to prove the existence of enforced double Weyl points, nodal planes, and other band topologies, and have shown that space group symmetries can not stabilize nodal lines with finite chiral charges (Sec. IV). Combining the local constraint with an exhaustive classification of low-energy models, we have determined the generic topological phase diagrams of all multifold crossings (Sec. V). Our analysis reveals that multifold crossings can exhibit more than one configuration of chiral charges. Moreover, we have found a novel fourfold crossing point with Chern number 5 (Sec. VB 1).

Our findings have direct implications for material design and for interpreting the band topology of existing materials. For example, we have identified the B20 materials class as having band structures where this Chern number 5 crossing can occur and have shown that for BaAsPt this exotic band crossing is at the Fermi level (Sec. VI). In addition, we have

uncovered that NbO₂/TaO₂ in SG 80 has a band structure with double Weyl points.

There are several directions for future work. First, the local and global constraints generalize immediately to one- and two-dimensional systems and can be applied also to magnetic space groups. For example, the local constraint can be used to infer the existence of double Weyl points away from TRIMs in magnetic space groups, similar to Sec. IV A 1. Second, our fundamental laws can be employed to study (multifold) nodal points and nodal planes of bosonic band structures, e.g., phonon or magnon bands. Third, our results have implications for topological response functions that are influenced by the Berry curvature, e.g., anomalous Hall currents, photogalvanic effects, and magneto-optic Kerr effects. Working out signatures of the discussed band topologies (e.g., the nodal planes or the fourfold crossings with $\nu = 5$) in these response functions would be an interesting task for future study.

ACKNOWLEDGMENTS

We are thankful to Douglas Fabini, Johannes Mitscherling, and Barry Bradlyn for enlightening discussions. We acknowledge the support by the Max Planck-UBC-UTokyo Center for Quantum Materials. KA, MMH, NH, and APS thank the YITP Kyoto for hospitality. M.M.H. was funded by the Deutsche Forschungsgemeinschaft (DFG, German Research Foundation) – Projektnummer 518238332. K.A., N.H., and A.P.S. are funded by the Deutsche Forschungsgemeinschaft (DFG, German Research Foundation) – TRR 360 – 492547816.

APPENDIX A: PROOF OF EQ. (7)

Since we chose a different sign in the definition of the Berry connection [see Eq. (14)] as compared to [55], we here present the derivation of Eq. (7) [Eq. (83) in Ref. [55]]. The following equations are valid for any crystalline symmetry R , while in this paper, we are concerned with the $R = D(C_n)$ case.

$$\begin{aligned} \mathbf{A}(R \cdot \mathbf{k}) &= i \langle n(R \cdot \mathbf{k}) | R \cdot \nabla_{\mathbf{k}} | m(R \cdot \mathbf{k}) \rangle \\ &= iR \sum_{c,d} \mathcal{B}_{C_n}(\mathbf{k})_{nc} \langle c(\mathbf{k}) | \hat{R}^{-1} \nabla_{\mathbf{k}} \mathcal{B}_{C_n}^*(\mathbf{k})_{md} \hat{R} | d(\mathbf{k}) \rangle \\ &= iR \sum_{c,d} \mathcal{B}_{C_n}(\mathbf{k})_{nc} \langle c(\mathbf{k}) | \nabla_{\mathbf{k}} \mathcal{B}_{C_n}^*(\mathbf{k})_{md} | d(\mathbf{k}) \rangle \\ &= R(\mathcal{B}_{C_n} \mathbf{A}(\mathbf{k}) \mathcal{B}_{C_n}^{-1} + i \mathcal{B}_{C_n} \nabla_{\mathbf{k}} \mathcal{B}_{C_n}^{-1}). \end{aligned} \quad (\text{A1})$$

APPENDIX B: TIGHT-BINDING MODEL FOR SG 80

To illustrate the band topology induced by SG 80, we give a minimal tight-binding model for the spinless and spinful case, as discussed in Sec. IV A 1. We consider a generic model for the 2a Wyckoff position and take all symmetry-allowed terms up to second nearest neighbors into account. We use the phase convention of Bloch functions for the tight-binding orbitals [59] and the primitive vectors as basis for \mathbf{k} [107]. Our model takes the form

$$\begin{aligned} (H_{\text{SG80}, \uparrow})_{11} &= 2t'_1(\cos(k_1 + k_2 + k_3) + \cos(k_3)) \\ &\quad + 2t'_2(\cos(k_1) + \cos(k_2)), \end{aligned} \quad (\text{B1})$$

$$(H_{\text{SG80},\uparrow})_{22} = 2t'_1(\cos(k_1) + \cos(k_2)) + 2t'_2(\cos(k_1 + k_2 + k_3) + \cos(k_3)), \quad (\text{B2})$$

$$(H_{\text{SG80},\uparrow})_{12} = (H_{\uparrow})_{21}^* \quad (\text{B3})$$

$$= t_1(1 + e^{ik_1} + e^{i(k_1+k_3)} + e^{i(k_1+k_2+k_3)}) + t_2(e^{i(k_1+k_2)} + e^{-ik_2} + e^{i(2k_1+k_2+k_3)} + e^{ik_3}), \quad (\text{B4})$$

where the parameters $t_1, t_2, t'_1, t'_2 \in \mathbb{R}$. With spin-orbit coupling the full Hamiltonian becomes

$$H_{\text{SG80}}(\mathbf{k}) = \begin{pmatrix} H_{\text{SG80},\uparrow}^{\text{SOC}} & H_{\text{SG80},\uparrow\downarrow}^{\text{SOC}} \\ (H_{\text{SG80},\uparrow\downarrow}^{\text{SOC}})^\dagger & H_{\text{SG80},\downarrow}^{\text{SOC}} \end{pmatrix}, \quad (\text{B5})$$

where $H_{\text{SG80},\uparrow}^{\text{SOC}}$ and $H_{\text{SG80},\downarrow}^{\text{SOC}}$ is obtained by $H_{\text{SG80},\uparrow}$ by adding hopping terms that differ for the two spin directions. We introduce this by

$$H_{\text{SG80},\uparrow}^{\text{SOC}} = H_{\text{SG80},\uparrow} + \Delta H_{\text{SG80},\uparrow}, \quad (\text{B6})$$

$$(\Delta H_{\text{SG80},\uparrow})_{11} = (\tilde{t}'_1(e^{i(-k_1-k_2-k_3)} + e^{ik_3}) + \tilde{t}'_2(e^{-ik_1} + e^{-ik_2})) + \text{c.c.}, \quad (\text{B7})$$

$$(\Delta H_{\text{SG80},\uparrow})_{22} = (\tilde{t}'_1(e^{-ik_1} + e^{-ik_2}) + \tilde{t}'_2(e^{i(-k_1-k_2-k_3)} + e^{ik_3})) + \text{c.c.}, \quad (\text{B8})$$

$$(\Delta H_{\text{SG80},\uparrow})_{12} = (\Delta H_{\text{SG80},\uparrow})_{21}^* = \tilde{t}_1(e^{ik_1} + e^{i(k_1+k_2+k_3)}) + \tilde{t}_2(e^{ik_1+ik_2} + e^{i(2k_1+k_2+k_3)}) + \tilde{t}_1^*(1 + e^{i(k_1+k_3)}) + \tilde{t}_2^*(e^{-ik_2} + e^{ik_3}), \quad (\text{B9})$$

where $\tilde{t}'_1, \tilde{t}'_2 \in \mathbb{C}$. The corresponding matrix elements in $H_{\text{SG80},\downarrow}^{\text{SOC}}$ can be obtained from $H_{\text{SG80},\uparrow}^{\text{SOC}}$ by replacing in the diagonal entries $\mathbf{k} \rightarrow -\mathbf{k}$ and in the off-diagonal entries $\tilde{t}_1(\tilde{t}_2) \rightarrow \tilde{t}_1^*(\tilde{t}_2^*)$ for all occurrences. The coupling between spins takes the form

$$(H_{\text{SG80},\uparrow\downarrow})_{11} = 2il'_1(\sin(k_1 + k_2 + k_3) + \sin(k_3)) + 2il'_2(\sin(k_1) - \sin(k_2)), \quad (\text{B10})$$

$$(H_{\text{SG80},\uparrow\downarrow})_{22} = 2l'_1(\sin(k_1) - \sin(k_2)) + 2l'_2(-\sin(k_1 + k_2 + k_3) - \sin(k_3)), \quad (\text{B11})$$

$$(H_{\text{SG80},\uparrow\downarrow})_{12} = l_1(1 + ie^{ik_1} - e^{i(k_1+k_3)} - ie^{i(k_1+k_2+k_3)}) + l_2(-ie^{i(k_1+k_2)} + e^{-ik_2} + ie^{i(2k_1+k_2+k_3)} - e^{ik_3}), \quad (\text{B12})$$

$$(H_{\text{SG80},\uparrow\downarrow})_{21} = -(H_{\text{SG80},\uparrow\downarrow}(\mathbf{k} \rightarrow -\mathbf{k}))_{12}, \quad (\text{B13})$$

where the parameters $l_1, l_2, l'_1, l'_2 \in \mathbb{C}$.

For the remaining discussion, we use the parameters defined in units of t_1 as $t_2 = 0.2$, $t'_1 = 0.3$, $t'_2 = -0.2$ and if spin-orbit coupling is included we add $\tilde{t}_1 = -0.1 + 0.2i$, $\tilde{t}_2 = 0.05 -$

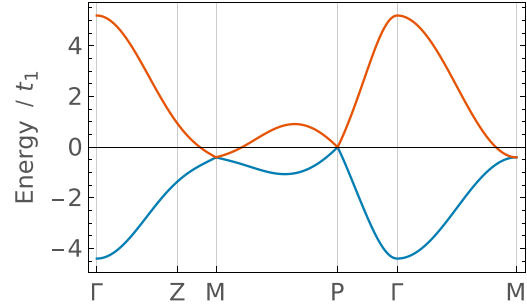


FIG. 12. Band structure for the model defined in Eq. (B5) respecting SG 80 *without* SOC. The Brillouin zone is shown in the in-set of Fig. 11(b).

$0.05i$, $l_1 = 0.4i$, $l_2 = 0.05 - 0.15i$, $\tilde{t}'_1 = 0.1$, $\tilde{t}'_2 = 0.05$, $l'_1 = l'_2 = 0.1i$. A possible minimal set of parameters that realizes the same band topology is given by $\tilde{t}_1 = 0.2 + 0.4i$, $l_1 = 0.8i$, $\tilde{t}_1 = 0.4$, where all other parameters (except $t_1 = 1$) are set to 0.

In the limit of vanishing spin-orbit coupling, our model exhibits only three Weyl points for each spin sector, one at each of the two distinct points P with $\nu = +1$ and a double Weyl point at the TRIM M with $\nu = -2$, see Fig. 12. Without the spin degeneracy the unity charge at the point P is different from the possible charges of twofold crossings at TRIMs, which are always $\nu = \pm 2$ in spinless systems [36]. The double Weyl point at M shows on the Γ -M path, i.e., the path where $k_z = 0$, the typical quadratic dispersion expected perpendicular to the rotation axis Γ -Z-M [73]. Note, our model for SG 80 without SOC is a counter example to the commonly conceived notion that there have to be at least four Weyl points in the presence of time-reversal symmetry [108,109]. Here, the number of Weyl points in our model is lower than four without additional band crossings [27].

Once spin-orbit coupling is taken into account the bands at P (M) split into a double Weyl point and two nondegenerate bands (two double Weyl points on the Γ -Z-M path), a detailed description is given in Sec. IV A 1.

For the numerical determination of Chern numbers, we use the Wilson loop approach on a discretized Brillouin zone as described in Ref. [110].

APPENDIX C: LOCAL CONSTRAINTS IN THE PRESENCE OF QUASISYMMETRIES

In the following, we derive a low-energy model for a twofold crossing that appears among the spinless representations of the point group T 23, describing the rotation symmetries of a tetrahedron. The resulting model applies to SGs 195-199 at the TRIMs Γ and R , L , or H within the primitive, face-centered, or body-centered cubic unit cells in the nomenclature of the Bilbao crystallographic server [111]. All possible terms up to third order that are compatible with the twofold and threefold rotation of the cubic point groups symmetry are taken into account by the Hamiltonian $H_T(\mathbf{k})$

with

$$H_T(\mathbf{k}) = (d_0 + d_1(k_x^2 + k_y^2 + k_z^2))\sigma_0 + a_0 k_x k_y k_z \sigma_z + \begin{pmatrix} 0 & a_1(k_x^2 + k_y^2 e^{-i2\pi/3} + k_z^2 e^{-i4\pi/3}) \\ \text{H.c.} & 0 \end{pmatrix}, \quad (\text{C1})$$

where the Pauli matrices σ_i have been used and $d_0, d_1, a_0 \in \mathbb{R}$, $a_1 \in \mathbb{C}$. The first term only shifts and bends both bands equally. The chirality ν of the twofold crossing at $\mathbf{k} = (0, 0, 0)$ is $\nu = 4\text{sgn}(a_0)$. In the basis used, the twofold and threefold rotations and time reversal are represented by

$$U(C_2^x) = \sigma_0, \quad U(C_3^{111}) = \begin{pmatrix} e^{i2\pi/3} & 0 \\ 0 & e^{-i2\pi/3} \end{pmatrix}, \quad (\text{C2})$$

and

$$T = \sigma_1 K, \quad (\text{C3})$$

respectively.

As discussed in the main text, $\nu = \pm 4$ is a peculiar value. For example, for $a_0 > 0$, the local constraints, Eq. (1), derived from the twofold and threefold rotations imply $\nu = 0 \pmod 2 = 1 \pmod 3$, which is consistent with $\nu = 4$ but would imply the simpler possibility of $\nu = -2$. This can not only be understood by a refined local constraint, Eq. (60), but also by the emergence of a yet recognized quasisymmetry that mimics a fourfold rotation. The existence of a fourfold symmetry, can be motivated pictorially by noticing that the symmetries C_2^z and $C_2^z T$ together reduce the integration surface of the Chern number into a quarter of the full sphere, as discussed in Sec. IV A 2. To gap out the bands away from $\mathbf{k} = 0$ and to obtain a well-defined chirality, it is sufficient to take all the symmetry-allowed terms up to cubic order in k_i , as we did in $H_T(\mathbf{k})$. Interestingly, the fourfold rotation symmetry of the model is only broken at the fourth order in k_i , which is irrelevant for the value of the Chern number.

The model, Eq. (C1), exhibits a parameter-dependent fourfold rotation symmetry $U(C_4^z)$ defined as

$$U(C_4^z) = \begin{pmatrix} 0 & e^{i(\arg(a_1)+2\pi/3)} \\ e^{-i(\arg(a_1)+2\pi/3)} & 0 \end{pmatrix}, \quad (\text{C4})$$

fulfilling

$$U(C_4^z)^\dagger H_T(k_x, k_y, k_z) U(C_4^z) = H_T(k_y, -k_y, k_z). \quad (\text{C5})$$

The symmetry eigenvalues of this operation are independent of a_1 and equal to $\lambda(C_4^z) \in \{+1, -1\}$. We made a choice of complex phase in Eq. (C4) that also does not affect the eigenvalues, but has been used to ensure that $U(C_4^z)$ commutes with time-reversal symmetry T . The commuting property together with the reality of eigenvalues implies that at the twofold degeneracy the symmetry eigenvalues of $U(C_4^z)$ do not exchange, i.e., the phase jump is $\Delta\varphi = 0$. And thus we can apply our local constraint according to Eq. (1) to the fourfold rotation to obtain $\nu = 0 \pmod 4$ resulting in $\nu = +4$ for $a_0 > 0$.

Let us compare this result to another low-energy model, again for a spinless system but now described by the octahe-

dral point group O 432, where the twofold axes of tetrahedral group T are replaced by fourfold rotations. We can turn $H_T(\mathbf{k})$ into a model of point group O by setting $a_1 = e^{-i2\pi/3}$ in Eq. (C1). This choice turns the quasisymmetry $U(C_4^z)$ into a representation [77] of the actual fourfold rotation of the octahedral point group. Naturally, for this fourfold rotation $U(C_4^z)$ our argument on the local constraint on the chirality is unchanged and one finds $\nu = \pm 4$ as well.

In summary, we find that the existence of a fourfold quasisymmetry in the low-energy model explains the charge $\nu = \pm 4$ of the twofold degeneracies with the tetrahedral point group T.

APPENDIX D: CHIRAL NODAL LINES FROM MAGNETIC SYMMETRIES

In Sec. IV A 3, we discussed the possibility of a nodal line characterized by a nonzero Chern number. In the following we generalize this discussion to symmetries, which comprise both time reversal T and an n -fold rotation C_n around the z direction. The arguments excluding the possibility of chiral nodal lines for $C_4 T$ and $C_6 T$ follow from the constraints in Eqs. (31) and (32) in the same way as in the main text.

If there is a nonzero sewing matrix phase difference $\Delta\phi_{c_b}$, the relations imply a pointlike band crossing on the axis. Since this implies that the only possible chiral charges of the line are equal to the multiplicity of Weyl points, such lines would be unstable. To see this, consider a case where $\Delta\phi_{c_b}$ is nonzero and does not change when the size of the sphere surrounding the $C_n T$ invariant point shrinks to zero. $\Delta\phi_{c_b} \neq 0$ implies with the local constraints $\nu_{c_b} \neq 0$. If ν_{c_b} is nonzero, only a pointlike crossing can carry the charge implied by the arbitrary small integration sphere.

Alternatively, if $\Delta\phi_{c_b}$ changes discontinuously when the sphere shrinks to zero, the crossings carrying the charge difference implied by the constraints, Eqs. (31) or (32), must lie on the rotation axis and can not be attributed to a chiral nodal line. To see this, one must deform the integration sphere into an spheroid while keeping the intersection points on the axis constant, such that $\Delta\phi_{c_b}$ remains unchanged. Thereby, the equatorial radius of the spheroid can be reduced to zero to exclude any finite size nodal line from the enclosed region, such that the topological charges may only lie on the rotation axis in form of WPs located where $\Delta\phi_{c_b}$ changes.

The case of $C_2 T$ differs, as the constraint derived from it does not include a term in the form of $\Delta\phi_{c_b}$, see Eq. (36). Instead it involves the winding of ϕ around the rotation axis on a $C_2 T$ invariant path. A nonzero winding, which results in a $\nu_{c_b} = 1 \pmod 2$ constraint, does not imply a charged nodal line of charge 1, since this nodal line is able to gap out into just a single WP on the $C_2 T$ invariant plane.

APPENDIX E: TIGHT-BINDING MODEL FOR SG 94

In the following, we define the model of SG 94 including spin and with time-reversal symmetry, which is used to create Fig. 5. We take the 2a Wyckoff position with the sites $(0, 0, 0)$, $(1/2, 1/2, 1/2)$ and a spin-1/2 as internal degree of freedom on each site. To keep the model simple, we pick three independent terms that are sufficient to avoid any

accidental band degeneracies from the set of hopping terms between up to next-nearest neighbors. Our 4×4 Hamiltonian thus takes the form

$$H_{\text{SG94},\uparrow} = \begin{pmatrix} H_{\text{SG94},\uparrow} & H_{\text{SG94},\text{SOC}} \\ H_{\text{SG94},\text{SOC}}^\dagger & H_{\text{SG94},\downarrow} \end{pmatrix}, \quad (\text{E1})$$

where the matrix blocks are

$$(H_{\text{SG94},\uparrow})_{11} = (H_{\text{SG94},\uparrow})_{22} = t_2 e^{-ik_z} + t_2^* e^{ik_z}, \quad (\text{E2})$$

$$(H_{\text{SG94},\uparrow})_{12} = (1 + e^{ik_x})(1 + e^{ik_y})(t_1 + t_1^* e^{ik_z}), \quad (\text{E3})$$

$$H_{\text{SG94},\downarrow} = H_{\text{SG94},\downarrow}(t_1 \leftrightarrow t_1^*, t_2 \leftrightarrow t_2^*) \quad (\text{E4})$$

for hopping that preserves spin and

$$(H_{\text{SG94},\text{SOC}})_{11} = (H_{\text{SG94},\text{SOC}})_{22} = 0, \quad (\text{E5})$$

$$(H_{\text{SG94},\text{SOC}})_{12} = t_{\text{SOC}}^* (-ie^{ik_x} + ie^{ik_y} - e^{ik_z} + e^{i(k_x+k_y+k_z)}) \\ + t_{\text{SOC}} (i - ie^{i(k_x+k_y)} - e^{i(k_x+k_z)} + e^{i(k_y+k_z)}), \quad (\text{E6})$$

$$(H_{\text{SG94},\text{SOC}})_{21} = e^{-i(k_x+k_y+k_z)} (t_{\text{SOC}}^* (-1 + e^{i(k_x+k_y)} \\ - ie^{i(k_x+k_z)} + ie^{i(k_y+k_z)}) \\ + t_{\text{SOC}} (-e^{ik_x} + e^{ik_y} + ie^{ik_z} - ie^{i(k_x+k_y+k_z)})) \quad (\text{E7})$$

for spin-orbit coupling terms. For Fig. 5, we use the parameters $t_1 = 1 + i$, $t_2 = 0.5 + 0.8i$, $t_{\text{SOC}} = -0.2 + 0.5i$.

APPENDIX F: CONSTRUCTION OF THE SPIN OPERATOR IN SG 195

We start by building a symmetry representation ρ at Γ by considering a p -orbital placed on the Wyckoff position 1a in SG 195

$$\rho(g) = \rho_{\text{orbital}}(g) \otimes \rho_{\text{spin}}(g), \quad (\text{F1})$$

where $g \in G$ with the little group G at Γ and ρ_{orbital} and ρ_{spin} being the action of the symmetry g on the orbital and spin degrees of freedom. To construct the spin operator, we want to find a U such that

$$U^\dagger \rho(g) U = (\bar{\Gamma}_6 \bar{\Gamma}_7 \oplus \bar{\Gamma}_5)(g). \quad (\text{F2})$$

We arrive at U by consecutive diagonalizations of $\rho(g)$ and $(\bar{\Gamma}_6 \bar{\Gamma}_7 \oplus \bar{\Gamma}_5)(g)$ for the generators g of the group. We first start with C_2

$$U_{\rho,C_2}^\dagger \rho(C_2) U_{\rho,C_2} = \text{diag}(i, i, i, -i, -i, -i) \wedge \quad (\text{F3})$$

$$U_{\Gamma,C_2}^\dagger (\bar{\Gamma}_6 \bar{\Gamma}_7 \oplus \bar{\Gamma}_5)(C_2) U_{\Gamma,C_2} = \text{diag}(i, i, i, -i, -i, -i)$$

\Rightarrow

$$U_{\rho,\text{block}}^\dagger U_{\rho,C_2}^\dagger \rho(C_2) U_{\rho,C_2} U_{\rho,\text{block}} = \text{diag}(i, i, i, -i, -i, -i) \\ = U_{\Gamma,\text{block}}^\dagger U_{\Gamma,C_2}^\dagger (\bar{\Gamma}_6 \bar{\Gamma}_7 \oplus \bar{\Gamma}_5)(C_2) U_{\Gamma,C_2} U_{\Gamma,\text{block}}, \quad (\text{F4})$$

where $\text{diag}(\dots)$ are diagonal matrices of symmetry eigenvalues and the $U_{x,\text{block}}$ have the block-diagonal form

$$U_{x,\text{block}} = \begin{pmatrix} U_{x,1,\text{block}} & 0 \\ 0 & U_{x,2,\text{block}} \end{pmatrix} \quad (\text{F5})$$

of 3×3 blocks, as eigenvectors in U_{x,C_2} can still be transformed in the $\pm i$ symmetry eigenvalue subspace. We can choose $U_{x,\text{block}}$ by diagonalizing the two diagonal 3×3 blocks of $\rho(C_3)$ and $(\bar{\Gamma}_6 \bar{\Gamma}_7 \oplus \bar{\Gamma}_5)(C_3)$

$$U_{\rho,\text{block}}^\dagger U_{\rho,C_2}^\dagger \rho(C_3) U_{\rho,C_2} U_{\rho,\text{block}} \\ = \begin{pmatrix} \text{diag}(e^{-\frac{i\pi}{4}}, e^{-\frac{i11\pi}{12}}, e^{\frac{5i\pi}{12}}) & Y_\rho \\ Y_\rho^\dagger & \text{diag}(e^{\frac{i\pi}{4}}, e^{\frac{i11\pi}{12}}, e^{-\frac{5i\pi}{12}}) \end{pmatrix}, \quad (\text{F6})$$

$$U_{\Gamma,\text{block}}^\dagger U_{\Gamma,C_2}^\dagger (\bar{\Gamma}_6 \bar{\Gamma}_7 \oplus \bar{\Gamma}_5)(C_3) U_{\Gamma,C_2} U_{\Gamma,\text{block}} \\ = \begin{pmatrix} \text{diag}(e^{-\frac{i\pi}{4}}, e^{-\frac{i11\pi}{12}}, e^{\frac{5i\pi}{12}}) & Y_\Gamma \\ Y_\Gamma^\dagger & \text{diag}(e^{\frac{i\pi}{4}}, e^{\frac{i11\pi}{12}}, e^{-\frac{5i\pi}{12}}) \end{pmatrix} \quad (\text{F7})$$

with matrices Y_x resulting from the application of the two previous diagonalizations. Equations (F6) and (F7) constrain the $U_{x,\text{block}}$ up to phases of the resulting eigenvectors of the 3×3 diagonal blocks in the transformed C_3 representations. These phases can be found by requiring $Y_\rho = Y_\Gamma$ and considering time-reversal symmetry T , where phases can be chosen such that

$$U_{\rho,\text{block}}^\dagger U_{\rho,C_2}^\dagger \rho(T) U_{\rho,C_2}^* U_{\rho,\text{block}}^* \\ = U_{\Gamma,\text{block}}^\dagger U_{\Gamma,C_2}^\dagger (\bar{\Gamma}_6 \bar{\Gamma}_7 \oplus \bar{\Gamma}_5)(T) U_{\Gamma,C_2}^* U_{\Gamma,\text{block}}^* \quad (\text{F8})$$

is fulfilled, where we already applied the complex conjugation operator of T . U in Eq. (F2) is then

$$U = U_{\rho,C_2} U_{\rho,\text{block}} U_{\Gamma,\text{block}}^\dagger U_{\Gamma,C_2}^\dagger \quad (\text{F9})$$

and the full spin operator is

$$U^\dagger \mathbb{1} \otimes \sigma_a U. \quad (\text{F10})$$

In this expression, Eq. (F10), only the 4×4 subblock belonging to the representation $\bar{\Gamma}_6 \bar{\Gamma}_7$ describes the spin texture of the multifold crossing, see Fig. 8. Explicitly, the spin operator in the $\bar{\Gamma}_6 \bar{\Gamma}_7$ irrep basis of the Bilbao crystallographic server [111] is

$$s_x = \frac{1}{3} \begin{pmatrix} 0 & -1 & 1 + i\sqrt{3} & 0 \\ -1 & 0 & 0 & -1 - i\sqrt{3} \\ 1 + i\sqrt{3} & 0 & 0 & 1 \\ 0 & -1 + i\sqrt{3} & 1 & 0 \end{pmatrix}, \quad (\text{F11})$$

$$s_y = \frac{1}{3} \begin{pmatrix} 0 & i & -i - \sqrt{3} & 0 \\ -i & 0 & 0 & -i - \sqrt{3} \\ i - \sqrt{3} & 0 & 0 & i \\ 0 & i - \sqrt{3} & -i & 0 \end{pmatrix}, \quad (\text{F12})$$

$$s_z = \frac{1}{3} \begin{pmatrix} -1 & 0 & 0 & 2 \\ 0 & 1 & 2 & 0 \\ 0 & 2 & 1 & 0 \\ 2 & 0 & 0 & -1 \end{pmatrix}. \quad (\text{F13})$$

APPENDIX G: FOURFOLD MODELS

1. SG 198 $\bar{\Gamma}_6\bar{\Gamma}_7$ model with SOC

In the following, we show that the phase transitions of the low-energy Hamiltonian (72) describing the $\bar{\Gamma}_6\bar{\Gamma}_7$ irrep are the ones shown in Fig. 6. We first apply a transformation into a basis diagonal in the threefold rotation

$$\begin{pmatrix} q_+ \\ q_- \\ q_z \end{pmatrix} = \frac{1}{2\sqrt{3}} \begin{pmatrix} 2 & -1 + i\sqrt{3} & -1 - i\sqrt{3} \\ 2 & -1 - i\sqrt{3} & -1 + i\sqrt{3} \\ -2 & -2 & -2 \end{pmatrix} \cdot \mathbf{k}. \quad (\text{G1})$$

Due to scale invariance, we can parametrize the following way:

$$\alpha_0 = \cos(G) \cos(Z), \quad (\text{G2})$$

$$\alpha_1 = \cos(G) \sin(Z), \quad (\text{G3})$$

$$\alpha_2 = \sin(G) \quad (\text{G4})$$

with $0 \leq Z < 2\pi$ and $-\frac{\pi}{2} \leq G \leq \frac{\pi}{2}$. We find all points in parameter space α_n where the energy levels of H become degenerate away from $\mathbf{k} = 0$ by considering the characteristic polynomial of H

$$\chi(E) = E^4 + a(q_+, q_z)E^2 + \det H. \quad (\text{G5})$$

Since there are only even powers of E in χ , the spectrum is particle-hole symmetric. It is gapless when $\det H = 0$ or $a^2 - 4\det H = 0$. We find that χ and $\det H$ do not depend on Z , so the topological phase diagram must be rotationally invariant. Further we parametrize

$$q_+ = \exp(iK) \cos(M), \quad (\text{G6})$$

$$q_z = \sin(M) \quad (\text{G7})$$

with $0 \leq K < 2\pi$ and $-\frac{\pi}{2} \leq M \leq \frac{\pi}{2}$, due to scale-invariance without loss of generality.

$\det H = 0$ case. We find

$$\det H = p_1(G, M) \cos(K)^3 + p_2(G, M) \cos(K) + p_3(G, M). \quad (\text{G8})$$

Particle-hole symmetry implies $\det H \geq 0$, so $\det H = 0$ must be a minimum. Therefore

$$\frac{d \det H}{dK} = -\sin(K)(3p_1 \cos(K)^2 + p_2) = 0 \quad (\text{G9})$$

$$\Rightarrow (\sin(K) = 0 \Rightarrow K \in \{0, \pi\}) \quad (\text{G10})$$

$$\vee \cos(K) = \pm \sqrt{\frac{-p_2}{3p_1}} = \pm \frac{1}{2} \quad (\text{G11})$$

$$\Rightarrow K \in \left\{ \frac{\pi}{3}, \frac{2\pi}{3}, \frac{4\pi}{3}, \frac{5\pi}{3} \right\}. \quad (\text{G12})$$

So $\{0, \frac{\pi}{3}, \frac{2\pi}{3}, \pi, \frac{4\pi}{3}, \frac{5\pi}{3}\}$ are the only K values where H can get gapless via $\det H = 0$.

With $K = 0$, $\det H$ has the form

$$\det H = f_4(M) \sin(G)^4 + f_2(M) \sin(G)^2 + f_0(M). \quad (\text{G13})$$

It is zero when

$$\sin(G)^2 = \frac{-f_2 \pm \sqrt{f_2^2 - 4f_4f_0}}{2f_4} = U_{\pm}(M). \quad (\text{G14})$$

A solution for G is found, when U_{\pm} is real and $0 \leq U_{\pm} \leq 1$. We find this is the case for $M \in \{-\frac{\pi}{2}, \arctan(\frac{1}{2}), \frac{\pi}{2}\}$, where $U_+ = 0 \Rightarrow G = 0$, and $M = -\frac{\pi}{4}$ with $U_+ = \frac{1}{2} \Rightarrow G = \pm\frac{\pi}{4}$. $U_- = \sin(G)^2$ only reproduces the $M = -\frac{\pi}{4}$ solution.

The $M \in \{-\frac{\pi}{2}, \arctan(\frac{1}{2}), \frac{\pi}{2}\}$ solutions with $K = 0$ correspond (under symmetry and scale transformations) to degeneracies on the $k = (t, t, t)$ line, while $M = -\frac{\pi}{4}$ corresponds to $k = (t, 0, 0)$.

For the case $K = \pi$, we find after a transformation with $M \rightarrow -M$ and $U_{\pm} \rightarrow U_{\mp}$ the same solutions. All other cases of K can be found by applying the threefold symmetry. Therefore, with $\det H = 0$, degeneracies only happen on high-symmetry lines and there are gapless points at $G \in \{0, \pm\frac{\pi}{4}\}$. We find for $G = 0$ a gap closing of the bandpair (2,3) on C_3 invariant lines and at $G = \pm\frac{\pi}{4}$ a gap closing on C_2 invariant lines for the same bandpair.

$a^2 - 4\det H = 0$ case. We find due to particle-hole symmetry $a = -E_1^2 - E_2^2$, with E_n being the energies of band n , so $a^2 - 4\det H \geq 0$, since

$$\begin{aligned} a^2 &\geq 4\det H \\ \iff (E_1^2 + E_2^2)^2 &\geq 4E_1^2E_2^2 \\ \iff (E_1^2 - E_2^2)^2 &\geq 0. \end{aligned} \quad (\text{G15})$$

So the point where $a^2 - 4\det H = 0$ must be a minimum of $a^2 - 4\det H$. We find the following form of $a^2 - 4\det H$

$$\begin{aligned} a^2 - 4\det H &= s_1(G, M) \cos(K)^3 \\ &+ s_2(G, M) \cos(K) + s_3(G, M). \end{aligned} \quad (\text{G16})$$

An optimum can be found via

$$\frac{d(a^2 - 4\det H)}{dK} = -\sin(K)(3s_1 \cos(K)^2 + s_2) = 0 \quad (\text{G17})$$

$$\Rightarrow K \in \{0, \pi\} \quad (\text{G18})$$

$$\vee \cos(K) = \pm \sqrt{\frac{-s_2}{3s_1}} = \pm \frac{1}{2} \quad (\text{G19})$$

$$\Rightarrow K \in \left\{ \frac{\pi}{3}, \frac{2\pi}{3}, \frac{4\pi}{3}, \frac{5\pi}{3} \right\}. \quad (\text{G20})$$

So once again $\{0, \pi, \frac{\pi}{3}, \frac{2\pi}{3}, \frac{4\pi}{3}, \frac{5\pi}{3}\}$ are the only K values where H can get gapless, now via $a^2 - 4\det H = 0$. With $K = \frac{n\pi}{3}$ and $n \in \mathbb{N}$ we find

$$a^2 - 4\det H = (r_1(n, M) \cos(G)^2 + r_2(n, M)) \cos(G)^2 \quad (\text{G21})$$

solutions to $\cos(G)^2 = 0$ and $\cos(G)^2 = \frac{-r_2}{r_1}$ only exist for $G \in \{-\frac{\pi}{2}, 0, \frac{\pi}{2}\}$. For $G = 0$ we find a gap closing of the outer bandpairs at C_2 invariant lines. For $G = \pm\frac{\pi}{2}$, the gap closing of the same bandpair occurs for any q , as we find that $a^2 - 4\det H = 0$ for any M, K .

We therefore showed that the Hamiltonian is only gapless for $G \in \{-\frac{\pi}{2}, -\frac{\pi}{4}, 0, \frac{\pi}{4}, \frac{\pi}{2}\}$ at points away from $k = (0, 0, 0)$, which translates to $\alpha_2 = \pm\sqrt{\alpha_0^2 + \alpha_1^2}$, $\alpha_2 = 0$ or $\sqrt{\alpha_0^2 + \alpha_1^2} = 0$.

2. SG 207 $\bar{\Gamma}_8$ model with SOC

The generator of this irrep contains a time-reversal symmetry T , three twofold symmetries 2_{001} , 2_{010} , 2_{110} , and a threefold symmetry 3_{111} . The first-order Hamiltonian generated from these symmetries is

$$H = \alpha_0 \left[\frac{k_x}{2} (\sqrt{3}\sigma_x\tau_0 + \sigma_x\tau_z + \sigma_y\tau_0 - \sqrt{3}\sigma_y\tau_z) + \frac{k_y}{2} (-\sqrt{3}\sigma_x\tau_0 - \sigma_x\tau_z + \sigma_y\tau_0 - \sqrt{3}\sigma_y\tau_z) + k_z (\sigma_x\tau_x - \sigma_x\tau_y) \right] + \frac{\alpha_1}{\sqrt{2}} [k_x(\sigma_0\tau_x + \sigma_0\tau_y + \sigma_z\tau_x - \sigma_z\tau_y) + k_y(\sigma_0\tau_x + \sigma_0\tau_y - \sigma_z\tau_x + \sigma_z\tau_y) + 2k_z\sigma_z\tau_z]. \quad (\text{G22})$$

The characteristic polynomial of this Hamiltonian is identical to the one of Eq. (72) from the main text when $\alpha_1 = 0$ and $\alpha_2 \rightarrow \alpha_1$. Therefore the topological phase separating points in parameter space of α_0 and α_1 are reproduced. Computing the Chern numbers, one finds that topological phase diagram as a whole stays the same, except now, one axis corresponds to only α_0 , instead of $\sqrt{\alpha_0^2 + \alpha_1^2}$. The statements about the symmetry eigenvalue phase jumps also stay the same. We note that the topological phase diagram of an equivalent Hamiltonian in SG 207 has been examined in a similar way in the supplementary material of Ref. [16] (see Sec. IV), but the $v_2 = 5$ phase has not yet been identified.

This model also describes SG 207 \bar{R}_8 , SG 208 $\bar{\Gamma}_8$, \bar{R}_8 , SG 209 $\bar{\Gamma}_8$, SG 210 $\bar{\Gamma}_8$, SG 211 $\bar{\Gamma}_8$, \bar{H}_8 , SG 212 $\bar{\Gamma}_8$, SG 213 $\bar{\Gamma}_8$, SG 214 $\bar{\Gamma}_8$ with SOC.

The SG 214 \bar{H}_8 model with SOC can be found by applying $U = \sigma_0\tau_x$ and $\alpha_1 \rightarrow -\alpha_1$ to the Hamiltonian in Eq. (G22).

3. SG 198 $\bar{M}_5\bar{M}_5$ model with SOC

The generator of this irrep contains a time-reversal symmetry T and two twofold symmetries 2_{001} , 2_{010} . The generated Hamiltonian is

$$H = \alpha_0 k_z \sigma_0 \tau_y + \alpha_1 k_x \sigma_z \tau_z + \alpha_2 k_x \sigma_x \tau_z + \alpha_3 k_x \sigma_y \tau_z + \alpha_4 k_y \sigma_z \tau_x + \alpha_5 k_y \sigma_x \tau_x + \alpha_6 k_y \sigma_y \tau_x. \quad (\text{G23})$$

Its spectrum is particle-hole symmetric as the characteristic polynomial is $\chi(E) = E^4 + aE^2 + \det H$.

We can rewrite H with

$$\alpha_1 = (\alpha_1, \alpha_2, \alpha_3)^T, \quad (\text{G24})$$

$$\alpha_2 = (\alpha_4, \alpha_5, \alpha_6)^T, \quad (\text{G25})$$

such that

$$H = \alpha_0 k_z \tau_y \sigma_0 + k_x \tau_z (\alpha_1 \cdot \sigma) + k_y \tau_x (\alpha_2 \cdot \sigma). \quad (\text{G26})$$

Due to the two nodal planes on the $k_x = 0$ and $k_y = 0$ planes, the Chern number of single bands are always undefined. The Chern number for a filling of 2 can still be computed when there are no fourfold degeneracies away from $\mathbf{k} = (0, 0, 0)^T$. Therefore we only need to find these fourfold degenerate points in parameter space, that is when $\det H = 0$.

If $\alpha_0 = 0$, then H is fourfold degenerate on the k_z line. If $\alpha_0 \neq 0$, $\alpha_1 \neq 0$ and $\alpha_2 \neq 0$, we can normalize $|\alpha_{1/2}| = 1$ by using scale invariance of H . We rotate σ with a unitary transformation $U^\dagger \sigma U = R\sigma$ with R being a rotation matrix, such that

$$U^\dagger (\alpha_1 \cdot \sigma) U = \alpha_1 \cdot (R\sigma) = (R^{-1}\alpha_1) \cdot \sigma = \sigma_z, \quad (\text{G27})$$

where we chose R such that $R^{-1}\alpha_1 = (1, 0, 0)^T$. Then

$$H' = U^\dagger H U = \alpha_0 k_z \tau_y \sigma_0 + k_x \tau_z \sigma_z + k_y \tau_x (\tilde{\alpha}_2 \cdot \sigma). \quad (\text{G28})$$

with $\tilde{\alpha}_2 = R^{-1}\alpha_2$. We parametrize without loss of generality

$$\tilde{\alpha}_2 = (\cos P \cos R, \cos P \sin R, \sin P)^T, \quad (\text{G29})$$

$$\mathbf{k} = (\cos G \cos Z, \cos G \sin Z, \sin G)^T. \quad (\text{G30})$$

We find

$$|H'| = \det H = A(P, R, Z) \cos(G)^4 + 1 \quad (\text{G31})$$

and $\det H \geq 0$. The point $\det H = 0$ must be a minimum of $\det H$. We find optima at $G \in \{-\frac{\pi}{2}, 0, \frac{\pi}{2}\}$. $G = \pm\frac{\pi}{2}$ can be excluded, since there $\det H = 1 \neq 0$. This leaves $G = 0$. With this, we find the constraint for A such that $\det H = 0$,

$$A(P, R, Z) = 4(\cos^4 Z - \cos^2 Z)(1 - \cos^2 R \cos^2 P) = -1. \quad (\text{G32})$$

We find optima of $\det H$ with $\frac{d\det H}{dZ}|_{G=0} = \frac{dA}{dZ} = 0$ at $Z = n\frac{\pi}{4}$ with $n \in \mathbb{Z}_8$. We can exclude $Z = \frac{\pi}{2}, \pi$, and $\frac{3\pi}{2}$, since there $A = 0$. Inserting the remaining Z values, we get

$$\cos^2 R \cos^2 P = 0. \quad (\text{G33})$$

Note that

$$\alpha_1 \cdot \alpha_2 = (R^{-1}\alpha_1) \cdot (R^{-1}\alpha_2) = (1, 0, 0)^T \cdot \tilde{\alpha}_2 = \cos P \cos R. \quad (\text{G34})$$

Therefore $\alpha_1 \cdot \alpha_2 = 0$ represents a surface in parameter space separating different topological phases. This is also true when $|\alpha_{1/2}| = 0$.

If $|\alpha_1| = 0$, we find the characteristic polynomial of H with the same parametrization of \mathbf{k} as above and $|\alpha_2| = 1$

$$\chi(E) = (E^2 + \cos^2 G \cos^2 Z - 1)^2. \quad (\text{G35})$$

Note that $\chi(E)$ is independent of α_2 since it can always be rotated by a unitary transformation, such that H is rotationally invariant in α_2 . We find a fourfold point at $E_{1,2,3,4} = 0$. This is the case, when $G = 0$ and $Z \in \{0, \pi\}$, so H is fourfold degenerate on the k_x line.

If $|\alpha_2| = 0$, we find the characteristic polynomial of H with $|\alpha_1| = 1$

$$\chi(E) = (E^2 + \cos^2 G \sin^2 Z - 1)^2. \quad (G36)$$

We find a fourfold point at $G = 0$ and $Z \in \{\frac{\pi}{2}, \frac{3\pi}{2}\}$, so H is fourfold degenerate on the k_y line.

In conclusion, we found that the topology of this model is entirely dependent on the sign of α_0 and $\alpha_1 \cdot \alpha_2$. We find the Chern number of the lowest two bands to be $\nu = 2(-1)^{\theta(\alpha_0) + \theta(\alpha_1 \cdot \alpha_2)}$, with $\theta(x)$ being the Heaviside step function.

For both twofold symmetries, the constraint of Eq. (18) amounts to $\nu_{12} = 0 \pmod 2$ by direct calculation. This can be seen directly on the (001) line, where the same symmetry eigenvalues are paired by 2_{001} . This way, a symmetry eigenvalue jump can be defined for the two degenerate bands and is equal to π everywhere in the phase diagram. Using Eq. (19) one arrives once again at $\nu_{12} = \frac{2}{2\pi}(\pi + \pi) \pmod 2 = 0 \pmod 2$.

This Hamiltonian also describes SG 18 $\bar{S}_5\bar{S}_5$, $\bar{R}_5\bar{R}_5$, SG 19 $\bar{S}_5\bar{S}_5$ with SOC. By applying a Chern number preserving $k_x \rightarrow k_y, k_y \rightarrow k_z, k_z \rightarrow k_x$ rotation, one arrives at the SG 19 $\bar{T}_5\bar{T}_5$, SG 92 $\bar{R}_5\bar{R}_5$ and SG 96 $\bar{R}_5\bar{R}_5$ Hamiltonian. By applying a $k_y \rightarrow k_z, k_z \rightarrow k_y$ reflection, during which Chern numbers are flipped, one arrives at the SG 19 $\bar{U}_5\bar{U}_5$ model.

4. SG 212 $\bar{M}_6\bar{M}_7$ model with SOC

The little groups generator contains a time-reversal symmetry T and three twofold symmetries $2_{001}, 2_{010}, 2_{110}$. The low-energy Hamiltonian generated from these symmetries is

$$\begin{aligned} H = & \alpha_0 k_z \sigma_z \tau_z + \alpha_1 [k_x \sigma_0 \tau_y - k_y \sigma_z \tau_x] \\ & + \alpha_2 [k_x \sigma_x \tau_z - k_y \sigma_y \tau_0] \\ & + \alpha_3 [k_x \sigma_y \tau_z + k_y \sigma_x \tau_0]. \end{aligned} \quad (G37)$$

The lower and upper two bands of this Hamiltonian always have doubly degenerate points, such that the Chern number of the lower and upper band is undefined. This means, we only have to look at all points in parameter space where $\det H = 0$. This is the case when $|\alpha_1, \alpha_2, \alpha_3| = 0$. There, $H = 0$ on the $k_z = 0$ plane. We also find $H = 0$ for $\alpha_0 = 0$ on the k_z line. Due to these considerations and scaling properties of H , we first consider the $\alpha_0 = 1$ case, which corresponds to $\alpha_0 > 0$.

We also set $k_z = 1$, such that all now reachable k points correspond under rescaling to the upper half of the unit sphere in k space. We parametrize

$$\begin{aligned} \alpha_1 &= r_1 \cos P \cos R, \\ \alpha_2 &= r_1 \cos P \sin R, \\ \alpha_3 &= r_1 \sin P \end{aligned} \quad (G38)$$

with $r_1 \geq 0$. $\det H$ takes on the following form:

$$\begin{aligned} \det H = & r_1^4 (k_x^4 + k_y^4 + (16F(R, P) + 2)k_x^2 k_y^2) \\ & + 2r_1^2 (k_x^2 + k_y^2) + 1 \end{aligned} \quad (G39)$$

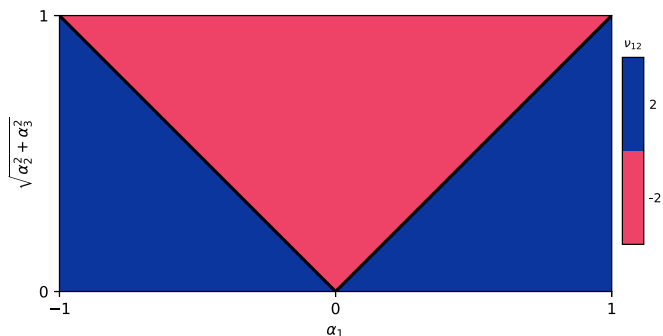


FIG. 13. Topological phase diagram of the lower two bands Chern number ν_{12} of the SG 212 $\bar{M}_6\bar{M}_7$ Model with $\alpha_0 > 0$.

where we find $-\frac{1}{4} \leq F(R, P) \leq 0$ with $F(R, P) = \cos^2 P \cos^2 R (\cos^2 P \cos^2 R - 1) = \alpha_1^2 (\alpha_1^2 - r_1^2) / r_1^4$. Inserting the minimal value of F in $\det H$, we get

$$\det H = r_1^4 (k_x^2 - k_y^2)^2 + 2r_1^2 (k_x^2 + k_y^2) + 1. \quad (G40)$$

There $\det H = 0$ has no real solution, as $\det H > 0$. Therefore, for all $F \in [-\frac{1}{4}, 0]$, $\det H > 0$. Due to symmetry, this means, that also on the $k_z = -1$ plane, no degeneracies of the middle bandpair can occur. The only way left is the $k_z = 0$ with $r_1 > 0$ and $|(k_x, k_y)| \neq 0$ case. We enforce this, by parametrizing $k_x = r_2 \cos(G), k_y = r_2 \sin(G)$ with $r_2 > 0$. The determinant with $k_z = 0$ becomes

$$\begin{aligned} \det H = & r_1^4 r_2^4 (1 - 4(1 - \cos(P)^2 \cos(R)^2) \\ & \times \cos(P)^2 \cos(R)^2 \sin(2G)^2). \end{aligned} \quad (G41)$$

At $\det H = 0$, this becomes

$$|\sin(2G)| = \frac{1}{2\sqrt{1 - \left(\frac{\alpha_1}{r_1}\right)^2 \left|\frac{\alpha_1}{r_1}\right|}} = K(\alpha_1/r_1). \quad (G42)$$

The only solutions with $0 \leq K \leq 1$ and $K \in \mathbb{R}$, are $\alpha_1 = \pm \frac{r_1}{\sqrt{2}}$ with $K = 1$, such that $G \in \{\frac{\pi}{4}, \frac{3\pi}{4}, \frac{5\pi}{4}, \frac{7\pi}{4}\}$. The topological phase diagram is therefore rotationally invariant in the $(\alpha_1, \alpha_2, \alpha_3)$ parameter space around the α_1 axis. The phase separating lines are $\alpha_1 = \pm \sqrt{\alpha_2^2 + \alpha_3^2}$. The topological phase diagram can be determined the same way as in the previous models, see Fig. 13. For $\alpha_0 < 0$, the Chern numbers in Fig. 13 switch signs.

By direct calculation of Eq. (18), we find $\nu_{12} = 0 \pmod 2$. The symmetry eigenvalue phase jump for 2_{001} is defined, since on the (001) the same symmetry eigenvalues are paired, and π for all bands. The symmetry eigenvalue jump of 2_{110} is also defined and π . Both lead to the $\nu_{12} = 0 \pmod 2$ constraint once again, see Eq. (19). Symmetry eigenvalue jumps are undefined for 2_{010} , as there different symmetry eigenvalues are paired.

We get the SG 213 $\bar{M}_6\bar{M}_7$ Model with SOC by mapping $k_y \rightarrow -k_y$. This flips the sign of the Chern numbers in the topological phase diagram of this model.

5. SG 198 R_1R_3 model without SOC

This model is symmetric under a time-reversal symmetry T , two twofold symmetries $2_{001}, 2_{010}$, and a threefold

symmetry 3_{111} .

$$H = \alpha_0[-k_x\sigma_z\tau_x + k_y\sigma_0\tau_y + k_z\sigma_z\tau_z]. \quad (\text{G43})$$

Due to the nodal plane, the Chern number of the lower and upper bands are undefined. The Chern number with a filling of 2 is $\nu_{12} = 2(-1)^{\theta(\alpha_0)}$. Evaluating Eq. (18) yields the constraints $\nu_{12} = 0 \pmod{2}$, $\nu_{12} = 1 \pmod{3}$ for $\alpha_0 > 0$ and $\nu_{12} = 2 \pmod{3}$ for $\alpha_0 < 0$, which are all fulfilled in this model. This model also describes SG 198 R_2R_2 , SG 212 R_1R_2 , SG 213 R_1R_2 without SOC.

6. SG 212 R_3 model without SOC

This model is symmetric under a time-reversal symmetry T , three twofold symmetries 2_{001} , 2_{010} , 2_{110} , and a threefold symmetry 3_{111} . The low-energy Hamiltonian is

$$H = \alpha_0[k_x(-\sigma_0\tau_x + \sigma_0\tau_y - \sigma_z\tau_x - \sigma_z\tau_y) + k_y(-\sigma_0\tau_x + \sigma_0\tau_y + \sigma_z\tau_x + \sigma_z\tau_y) + 2k_z\sigma_z\tau_z]. \quad (\text{G44})$$

Due to the nodal plane, the Chern number of the lower and upper bands are undefined. The Chern number with a filling of 2 is $\nu_{12} = 2(-1)^{\theta(\alpha_0)}$. From Eq. (18) we get the fulfilled constraints $\nu_{12} = 0 \pmod{2}$, $\nu_{12} = 1 \pmod{3}$ for $\alpha_0 > 0$ and $\nu_{12} = 2 \pmod{3}$ for $\alpha_0 < 0$. This model also describes SG 213 R_3 without SOC.

7. SG 90 $\bar{A}_6\bar{A}_7$ model with SOC

This model is symmetric under a time-reversal symmetry T , two twofold symmetries 2_{001} , 2_{010} , and a fourfold symmetry 4_{001} . The Hamiltonian is

$$\begin{aligned} H = & \alpha_0 k_z \sigma_z \tau_z + \alpha_1 [k_x (\sigma_0 \tau_y + \sigma_z \tau_x) + k_y (\sigma_0 \tau_y - \sigma_z \tau_x)] \\ & + \frac{\alpha_2}{\sqrt{2}} [k_x (-\sigma_x \tau_0 - \sigma_x \tau_z + \sigma_y \tau_0 - \sigma_y \tau_z) \\ & + k_y (-\sigma_x \tau_0 + \sigma_x \tau_z + \sigma_y \tau_0 + \sigma_y \tau_z)] \\ & + \frac{\alpha_3}{\sqrt{2}} [k_x (\sigma_x \tau_0 - \sigma_x \tau_z + \sigma_y \tau_0 + \sigma_y \tau_z) \\ & + k_y (\sigma_x \tau_0 + \sigma_x \tau_z + \sigma_y \tau_0 - \sigma_y \tau_z)]. \end{aligned} \quad (\text{G45})$$

We only need to look at the $\det H = 0$ points, due to the double degeneracy of the first two bands at some \mathbf{k} lines. When $\alpha_0 = 0$, $H = 0$ on the k_z line, so $\alpha_0 = 0$ divides the topological phase diagram. Therefore we set $\alpha_0 = 1$, which corresponds to the $\alpha_0 > 0$ region. The Chern numbers we get will either remain unchanged or flip for $\alpha_0 < 0$. We also first look at the $k_z = 1$ plane. Then we get

$$\begin{aligned} \det H = & A(k_x, k_y, r) \sin(P)^4 + B(k_x, k_y, r) \sin(P)^2 \\ & + C(k_x, k_y, r), \end{aligned} \quad (\text{G46})$$

where we parameterized $\alpha_1 = r \sin(P)$, $\alpha_2 = r \cos(P) \cos(R)$, $\alpha_3 = r \cos(P) \sin(R)$, and $r > 0$. We find that the determinant fulfills $B^2 - 4AC \leq 0$. So the only possible real solutions of $\det H = 0$ are when $B^2 - 4AC = 0$, which is the case when $k_x = 0 \vee k_y = 0$. At those points, $\det H = 0$ can not be fulfilled, since $A(0, k_y, r) = A(k_x, 0, r) = B(0, k_y, r) = B(k_x, 0, r) = 0$ and $C(0, k_y, r) \geq 1$ and $C(k_x, 0, r) \geq 1$. The only place left is the $k_z = 0$ plane. We parametrize

$k_x = \cos(G)$, $k_y = \sin(G)$, where we used the scaling properties of H . We get

$$\begin{aligned} \det H = & r^4 (-64 \sin(G)^4 \sin(P)^4 + 64 \sin(G)^4 \sin(P)^2 \\ & + 64 \sin(G)^2 \sin(P)^4 - 64 \sin(G)^2 \sin(P)^2 + 4). \end{aligned} \quad (\text{G47})$$

The only real solutions are $G \in \{\frac{\pi}{4}, \frac{3\pi}{4}, \frac{5\pi}{4}, \frac{7\pi}{4}\}$ with $P = \pm \frac{\pi}{4}$.

The topological phase diagram is identical to the one of the SG 212 $\bar{M}_6\bar{M}_7$ model, see Fig. 13, with $\alpha_0 > 0$. The Chern numbers flip when $\alpha_0 < 0$.

The symmetry eigenvalue jump of 2_{001} is always π . The one of 4_{001} and 2_{010} can not be defined, since different eigenvalues are paired. So we need to use Eq. (18) to derive constraints. We get $\nu_{12} = 0 \pmod{2}$ and $\nu_{12} = 2 \pmod{4}$, both fulfilled in all topological phases of this model.

This model also describes SG 90 $\bar{M}_6\bar{M}_7$, SG 92 $\bar{M}_6\bar{M}_7$, SG 94 $\bar{M}_6\bar{M}_7$, SG 96 $\bar{M}_6\bar{M}_7$ with SOC. The reflection $k_x \leftrightarrow k_y$ can be applied, during which Chern numbers are flipped, to get the SG 94 $\bar{A}_6\bar{A}_7$ model with SOC. Apply the Chern number preserving rotation $k_x \rightarrow k_y$ and $k_y \rightarrow -k_x$ and set $\alpha_2 = 0$ and $\alpha_3 = 0$ to get the SG 92 A_1A_2 model without SOC, where the Chern number with a filling of 2 is just $\nu = -2(-1)^{\theta(\alpha_0)}$. The SG 96 A_1A_2 model is found by applying a $k_y \rightarrow -k_y$ reflection and also by setting $\alpha_2 = 0$ and $\alpha_3 = 0$. This flips the sign of the Chern number.

8. SG 92 $\bar{A}_7\bar{A}_7$ model with SOC

This model is symmetric under a time-reversal symmetry T , two twofold symmetries 2_{001} , 2_{010} , and a fourfold symmetry 4_{001} . The generated Hamiltonian is

$$H = \alpha_0 k_z \sigma_z \tau_z + \alpha_1 k_x \sigma_x \tau_0 + \alpha_2 k_z \sigma_y \tau_0. \quad (\text{G48})$$

No Chern numbers can be defined. This Hamiltonian also describes SG 96 $\bar{A}_7\bar{A}_7$ with SOC. This Hamiltonian must be expanded to k^2 to extract Chern numbers. This was done in [27,112]. One arrives at $\nu = \pm 4$ for a filling of 2. Other Chern numbers can not be defined due to degeneracies. See [112] for the exact topological phase diagram.

9. SG 19 R_1R_1 model without SOC

This model is symmetric under a time-reversal symmetry T and two twofold symmetries 2_{001} , 2_{010} . The Hamiltonian is

$$H = \alpha k_x \sigma_z \tau_z + \beta k_y \sigma_z \tau_x + \gamma k_z \sigma_0 \tau_y. \quad (\text{G49})$$

H is always doubly degenerate due to the nodal planes. Therefore we only need to look for $\det H = 0$.

$$\det H = (k_x^2 \alpha^2 + k_y^2 \beta^2 + k_z^2 \gamma^2)^2. \quad (\text{G50})$$

This leads to the condition

$$k_x^2 \alpha^2 + k_y^2 \beta^2 + k_z^2 \gamma^2 = 0. \quad (\text{G51})$$

There exist \mathbf{k} points away from $\mathbf{k} = 0$ where this is the case when $\alpha = 0 \vee \beta = 0 \vee \gamma = 0$. We get $\nu_{12} = -2(-1)^{\theta(\alpha) + \theta(\beta) + \theta(\gamma)}$ for the lower two bands. The symmetry eigenvalue phase jump is always π for both 2_{001} and 2_{010} .

Therefore we get the condition $\nu_{12} = 0 \pmod 2$ from Eq. (19), which is fulfilled.

APPENDIX H: THREEFOLD MODELS

Introduce $\kappa = \alpha + i\beta$. Normalize it without loss of generality $\kappa = e^{i\gamma}$. Then

$$H = \begin{pmatrix} 0 & k_z e^{-i\gamma} & -k_y e^{i\gamma} \\ & 0 & k_x e^{-i\gamma} \\ \dots & & 0 \end{pmatrix}. \tag{H1}$$

The characteristic polynomial is

$$\begin{aligned} \chi(\lambda) &= -\lambda^3 + \lambda(k_x^2 + k_y^2 + k_z^2) - 2k_x k_y k_z \cos(3\gamma) \\ &= -\lambda^3 + 3\lambda - 2k_x k_y k_z \cos(3\gamma), \end{aligned} \tag{H2}$$

where we set normalized $k_x^2 + k_y^2 + k_z^2 = 3$ using the scale invariance of H . The characteristic polynomial with two degenerate energies is

$$\begin{aligned} \chi(\lambda) &= -(\lambda - E_1)^2(\lambda - E_2) \\ &= -\lambda^3 + \lambda^2(E_2 + 2E_1) \\ &\quad - \lambda(E_1^2 + 2E_1 E_2) + E_1^2 E_2. \end{aligned} \tag{H3}$$

We see that

$$E_2 = -2E_1, \tag{H4}$$

$$\begin{aligned} 3 &= -E_1^2 - 2E_1 E_2 = 3E_1^2 \\ \Rightarrow E_1 &= \pm 1 \wedge E_2 = \mp 2. \end{aligned} \tag{H5}$$

Using Eq. (H5) in Eq. (H3) and comparing it to Eq. (H2), we get

$$k_x^2 k_y^2 k_z^2 \cos(3\gamma)^2 = 1 \wedge k_x^2 + k_y^2 + k_z^2 = 3. \tag{H6}$$

The only solutions are

$$k_{x/y/z} = \pm 1 \wedge \gamma = \frac{\pi n}{3} \quad \text{with } n \in \mathbb{Z} \tag{H7}$$

so all lines in $\alpha\beta$ parameter space going from the origin and in $\frac{\pi}{3}$ angle to each other, starting at the $\beta = 0$ line are the only lines separating different topological phases. We get the phase diagram for ν_1 shown in Fig. 14, and $\nu_2 = -\nu_1$. The $\nu_1 = -2$ phases coincide with a symmetry eigenvalue phase jump of $\Delta\varphi_1 = 2\pi/3$, $\Delta\varphi_2 = 0$ and $\Delta\varphi_3 = 4\pi/3$ for the threefold rotation. The first bands phase jump leads with Eq. (1) to the constraint $\nu_1 = 1 \pmod 3$, consistent with $\nu_1 = -2$. We get phase jumps of $\Delta\varphi_1 = 4\pi/3$, $\Delta\varphi_2 = 0$ and $\Delta\varphi_3 = 2\pi/3$ for the $\nu_1 = 2$ phase, which is consistent with the constraint $\nu_1 = 2 \pmod 3$ derived from the $\Delta\varphi_1$.

APPENDIX I: SIXFOLD MODELS

The topological phase diagram for the sixfold model in Eq. (74) of irrep $\bar{R}_7 \bar{R}_7$ is invariant under rescaling $\alpha_n \rightarrow \alpha_n/r$ with $r > 0$. So we can reduce the number of parameters of the sixfold model to 3 by choosing an r such that $(\alpha_0 + i\alpha_1)/r = e^{i\phi}$. We rename $\alpha_{2/3}/r$ as $\alpha_{2/3}$. The parameters ϕ and $b = \alpha_2 + i\alpha_3$ correspond to the ones found in Ref. [16].

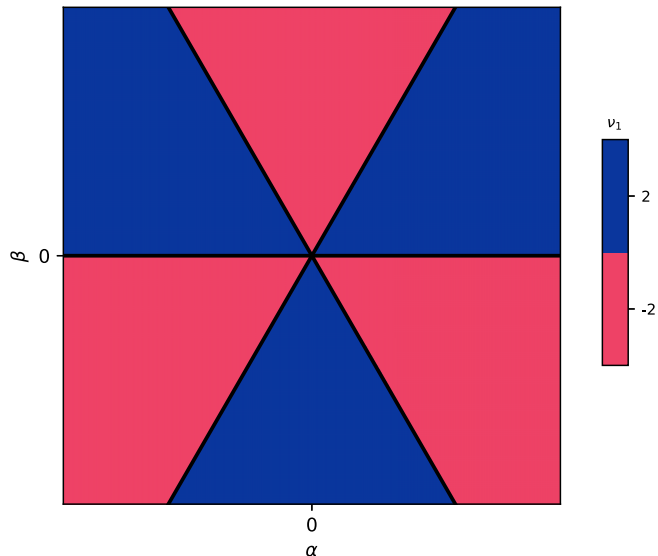


FIG. 14. Topological phase diagram of band I of the SG 199 \bar{P}_7 model.

The characteristic polynomial is of the form

$$\chi(E) = E^6 + A_1 E^4 + A_2 E^2 - \det H. \tag{I1}$$

We see that the spectrum must be particle-hole symmetric. Due to the nodal planes, Chern numbers for odd fillings can not be defined. One way a topological phase transition can happen is by a sixfold degeneracy. We first show that the only places, where this can happen is on the nodal planes. The determinant of H looks like this

$$\det H = B(\alpha_n) k_x^2 k_y^2 k_z^2. \tag{I2}$$

$\det H = 0$ is a necessary condition for a sixfold degeneracy. When $B \neq 0$, this is only the case on the nodal planes. A sixfold degeneracy and particle-hole symmetry implies $E_n = 0$. Therefore $A_1 = 0 \wedge A_2 = 0$ on the nodal plane. We parametrize $k_x = \cos(P)$, $k_y = \sin(P)$, $k_z = 0$. Then

$$A_1 = -2(\alpha_2^2 + \alpha_3^2 + 1), \tag{I3}$$

$$A_2 = (\alpha_2^2 + \alpha_3^2 + 1)^2. \tag{I4}$$

$A_1 = 0 \wedge A_2 = 0$ is not possible. This is also the case for all other nodal planes.

Another way a topological phase transition can happen is by a twofold degeneracy. At the energy of a twofold degeneracy, χ must have a maximum or minimum with $\chi = 0$. With $k_x^2 + k_y^2 + k_z^2 = 1$ we find that Eqs. (I3) and (I4) remain true. This means, χ has a local maximum at

$$E_{\pm}^{\max} = \pm \sqrt{\frac{\alpha_2^2 + \alpha_3^2 + 1}{3}} \tag{I5}$$

independent of a_0 and \mathbf{k} . $\det H$ is tuning the value of this maximum. Therefore $\det H$ can be tuned such that $\chi(E_{\pm}^{\max}) = 0$, where E_{\pm}^{\max} are the energies of the double degeneracies, in this case of band pairs (2,3) and (4,5). We get the condition

$$\det H = \frac{4}{27} (\alpha_2^2 + \alpha_3^2 + 1)^3. \tag{I6}$$

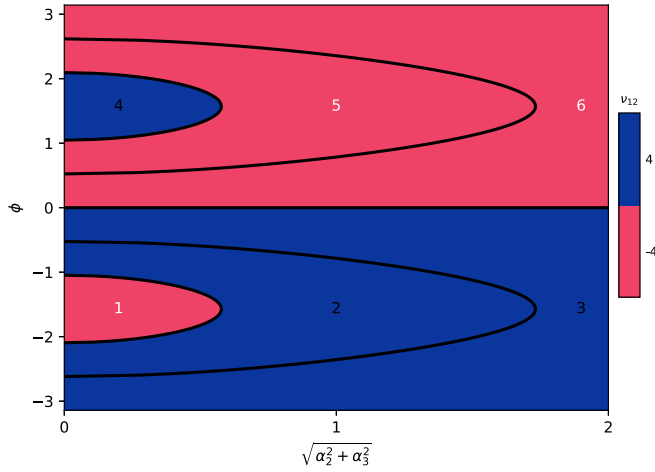


FIG. 15. Analytical topological phase diagram for a filling of 2 of the $\bar{R}_7\bar{R}_7$ model. All phases separated by a closing gap are numerated from 1 to 6.

We find that $\det H$ is

$$\det H = k_x^2 k_y^2 k_z^2 (2 \cos(2\phi) - 1 + \alpha_2^2 + \alpha_3^2)^2 \times (2 \cos(2\phi) + 2 + 4\alpha_2^2 + 4\alpha_3^2). \quad (17)$$

Equating the last two equations with $F = \alpha_2^2 + \alpha_3^2 + 1$ ($1 \leq F$), $S = 2 \cos(2\phi) - 2$ ($0 \geq S \geq -4$), and $A^{-1} = 27k_x^2 k_y^2 k_z^2$ ($1 \leq A$), we have

$$(S + F)^2(S + 4F) = 4AF^3. \quad (18)$$

The only solutions with $1 \leq A$ are $A = 1 \wedge S = -3F$ or $A = 1 \wedge S = 0$. $A = 1$ implies $k_x = k_y = k_z = \pm \frac{1}{\sqrt{3}}$ again. We get $\cos(2\phi) = \frac{-3\alpha_2^2 - 3\alpha_3^2 - 1}{2}$ and $\phi \in \{0, \pi\}$ as a surface in parameter space separating different topological phases.

Further, χ has minima at $E^{\min} = 0$ and $E_{\pm}^{\min} = \pm(\alpha_2^2 + \alpha_3^2 + 1)$ with $\chi(E^{\min}) = -\det H$. So we once again have the condition $\det H = 0$. The only unexplored way this condition can be fulfilled is by $B(\alpha_n) = 0$. This leads to

another phase separating surface with $\cos(2\phi) = \frac{-\alpha_2^2 - \alpha_3^2 + 1}{2}$, which corresponds to degeneracies of band pairs (1,2), (3,4), and (5,6). Since χ is independent of k_n at these parameters, this degeneracy occurs at all k points. It turns out, that this gap closing does not lead to a change in Chern number. This can be seen in Fig. 15, where the topological phase diagram of this model is shown and every phase is numerated from 1 to 6. Additionally, for small off diagonal terms ($\alpha_{2/3} \ll 1$) the topological phase diagram is equivalent to a double threefold point, as expected, since at $b = 0$, H is a direct sum of two threefold points. At large off diagonal terms, this is no longer the case. This is the only topological phase diagram out of all multifold crossings, where the topological phase depends on the parameters relative magnitude, in this case, the ratio $\frac{|\alpha_0 + i\alpha_1|}{|\alpha_2 + i\alpha_3|}$. The Chern number for the two middle bands is always zero. Following Ref. [16], we can get the SG 212/213 $\bar{R}_7\bar{R}_8$ model by setting $\alpha_0 = \frac{\pi}{2}$.

The band 1 symmetry eigenvalue jump of the threefold rotation is 0 in phases 3 and 6, $\frac{4\pi}{3}$ in phases 1 and 2 and $\frac{2\pi}{3}$ in phases 4 and 5. The band 2 symmetry eigenvalue jump of the threefold rotation is 0 in phases 2 and 5, $\frac{4\pi}{3}$ in phases 1 and 3 and $\frac{2\pi}{3}$ in phases 4 and 6. For band 3, we get symmetry eigenvalue jumps of 0 in phases 1 and 4, $\frac{4\pi}{3}$ in phases 2 and 6 and $\frac{2\pi}{3}$ in phases 3 and 5. For the remaining bands, particle-hole symmetry interchanges $\frac{2\pi}{3} \leftrightarrow \frac{4\pi}{3}$. We see that we can still distinguish between phases 1 and 2 (4 and 5) by symmetry eigenvalue jumps.

Bandpairs are degenerate on rotation axis of the twofold rotation, so Eq. (1) can not be applied here. Considering Eq. (18), all jumps of $\log \det \mathcal{B}_{C_2}$ are zero for all bandpairs. This puts constraints $v_{1,2} = 0 \pmod{2}$ and $v_{3,4} = 0 \pmod{2}$ on the non-Abelian Chern numbers. Further, the threefold rotation symmetry eigenvalue jumps lead with Eq. (19) to the following constraints $v_{1,2} = 1 \pmod{3}$ in phases 1, 5 and 6 and $v_{1,2} = 2 \pmod{3}$ in phases 2, 3 and 4. These constraints are consistent with the Chern numbers found in Fig. 15. For bands 3 and 4, we get $v_{1,2} = 0 \pmod{3}$, which is also fulfilled.

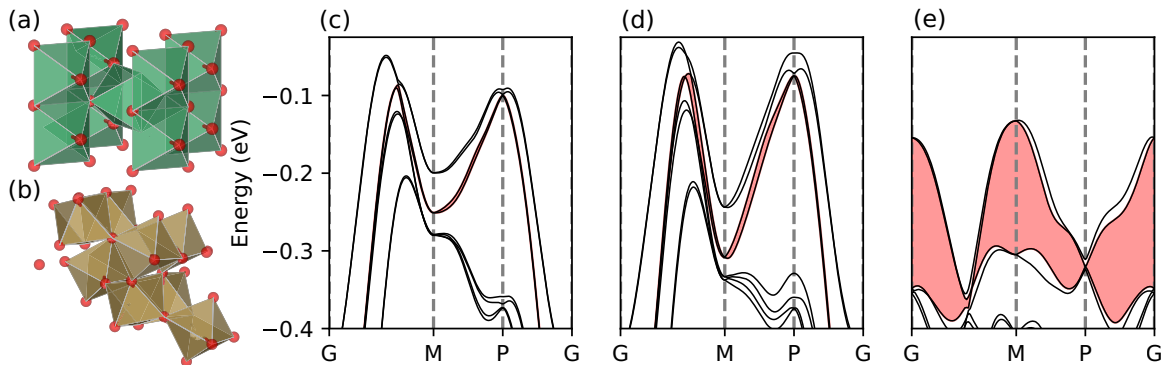


FIG. 16. (a) Crystal structure of the parent compound NbO_2 in SG #136 and (b) of TaO_2 with increased oxygen-deficiency in SG #80. [(c) and (d)] DFT band structures for the reported oxygen-deficient NbO_2 , the same structure with Nb substituted by Ta and the structure with enhanced oxygen-deficiency modeled by an increased distortion. The topological gaps are colored in red. NbO_2 has a small topological gap that can be slightly enhanced by substitution. Distorting the material (by a factor of 1.5 with respect to the distortion of the parent compound in SG #136 to the reported oxygen-deficient structure in SG #80) leads to a band inversion and a significant enhancement of the topological band gap.

APPENDIX J: GELLMANN MATRICES

We use the following definition of the Gellmann matrices.

$$\lambda_0 = \begin{pmatrix} 1 & 0 & 0 \\ 0 & -1 & 0 \\ 0 & 0 & 0 \end{pmatrix}, \tag{J1}$$

$$\lambda_1 = \begin{pmatrix} 0 & -i & 0 \\ i & 0 & 0 \\ 0 & 0 & 0 \end{pmatrix}, \tag{J2}$$

$$\lambda_2 = \begin{pmatrix} 0 & 0 & -i \\ 0 & 0 & 0 \\ i & 0 & 0 \end{pmatrix}, \tag{J3}$$

$$\lambda_3 = \begin{pmatrix} 0 & 1 & 0 \\ 1 & 0 & 0 \\ 0 & 0 & 0 \end{pmatrix}, \tag{J4}$$

$$\lambda_4 = \begin{pmatrix} \frac{1}{\sqrt{3}} & 0 & 0 \\ 0 & \frac{1}{\sqrt{3}} & 0 \\ 0 & 0 & -\frac{2}{\sqrt{3}} \end{pmatrix}, \tag{J5}$$

$$\lambda_5 = \begin{pmatrix} 0 & 0 & -i \\ 0 & 0 & 0 \\ i & 0 & 0 \end{pmatrix}, \tag{J6}$$

$$\lambda_6 = \begin{pmatrix} 0 & 0 & 1 \\ 0 & 0 & 0 \\ 1 & 0 & 0 \end{pmatrix}, \tag{J7}$$

$$\lambda_7 = \begin{pmatrix} 0 & 0 & 0 \\ 0 & 0 & 1 \\ 0 & 1 & 0 \end{pmatrix}, \tag{J8}$$

$$\lambda_8 = \mathbb{1}. \tag{J9}$$

APPENDIX K: DETAILS ON THE CALCULATION FOR TaO₂ AND NbO₂

To enlarge the topological band gap, we distort the reported oxygen-deficient NbO₂ structure further, modeling a stronger oxygen-deficiency, as well as substituting Nb with Ta. We assume that the enhanced deficiency leads to a distortion that is larger in magnitude but preserves the ratio of the modes it is composed of. In general, this is a complicated linear combination of many distortion modes. First,

TABLE V. Atomic positions of the distorted β -TaO₂ compound. The coordinates are given in lattice vectors $a_1 = (-4.847, 4.847, 2.967)$, $a_2 = (4.847, -4.847, 2.967)$, and $a_3 = (4.847, 4.847, -2.967)$ in units of angstrom.

Atom	x	y	z
Ta	0.276080	0.033580	0.217160
Ta	0.816420	0.058920	0.782840
Ta	0.308920	0.026080	0.742500
Ta	0.283580	0.566420	0.257500
Ta	0.206250	0.448580	0.727330
Ta	0.721250	0.478920	0.272670
Ta	0.728920	0.956250	0.257670
Ta	0.698580	0.471250	0.742330
O	0.097210	0.840550	0.951600
O	0.888950	0.145610	0.048400
O	0.395610	0.847210	0.756660
O	0.090550	0.638950	0.243340
O	0.618220	0.372050	0.977430
O	0.394620	0.640790	0.022570
O	0.890790	0.368220	0.746170
O	0.622050	0.144620	0.253830
O	0.111550	0.357720	0.449770
O	0.907950	0.661780	0.550230
O	0.911780	0.861550	0.253830
O	0.607720	0.657950	0.746170
O	0.595550	0.852220	0.484930
O	0.367290	0.110620	0.515070
O	0.360620	0.345550	0.243330
O	0.102220	0.117290	0.756670

we identify which linear combination of modes leads to the above-mentioned structural phase transition by using the ISODISTORT tool [106]. By comparing the parent and the reported oxygen-deficient compound, we can identify and then exaggerate the distortion by a factor of 1.5. The band structure of that structure has a much larger topological band gap while preserving the symmetry of the reported oxygen-deficient crystal, see Fig. 16. The crystallographic axes of the distorted cell are $a_1 = (-4.847, 4.847, 2.967)$, $a_2 = (4.847, -4.847, 2.967)$, and $a_3 = (4.847, 4.847, -2.967)$ in units of angstrom. The positions of the atoms are listed in Table V.

APPENDIX L: DETAILS ON DFT CALCULATIONS

The DFT calculations have been performed using the VASP software [113–115] and QUANTUM ESPRESSO [93,116] with optimized norm-conserving Vanderbilt pseudopotentials [117] from PSEUDODOJO [118] within the PBE approximation [119] of the exchange-correlation functional. For wannierization WANNIER90 [120] has been employment and the surface simulation was carried out using WANNIERTOOLS [121].

[1] C.-K. Chiu, J. C. Y. Teo, A. P. Schnyder, and S. Ryu, Classification of topological quantum matter with symmetries, *Rev. Mod. Phys.* **88**, 035005 (2016).

[2] N. P. Armitage, E. J. Mele, and A. Vishwanath, Weyl and dirac semimetals in three-dimensional solids, *Rev. Mod. Phys.* **90**, 015001 (2018).

- [3] A. Bernevig, H. Weng, Z. Fang, and X. Dai, Recent progress in the study of topological semimetals, *J. Phys. Soc. Jpn.* **87**, 041001 (2018).
- [4] B. A. Bernevig, C. Felser, and H. Beidenkopf, Progress and prospects in magnetic topological materials, *Nature (London)* **603**, 41 (2022).
- [5] H. Gao, J. W. Venderbos, Y. Kim, and A. M. Rappe, Topological semimetals from first principles, *Annu. Rev. Mater. Res.* **49**, 153 (2019).
- [6] B. Q. Lv, T. Qian, and H. Ding, Experimental perspective on three-dimensional topological semimetals, *Rev. Mod. Phys.* **93**, 025002 (2021).
- [7] X. Wan, A. M. Turner, A. Vishwanath, and S. Y. Savrasov, Topological semimetal and fermi-arc surface states in the electronic structure of pyrochlore iridates, *Phys. Rev. B* **83**, 205101 (2011).
- [8] G. Xu, H. Weng, Z. Wang, X. Dai, and Z. Fang, Chern semimetal and the quantized anomalous hall effect in HgCr_2Se_4 , *Phys. Rev. Lett.* **107**, 186806 (2011).
- [9] A. A. Soluyanov, D. Gresch, Z. Wang, Q. Wu, M. Troyer, X. Dai, and B. A. Bernevig, Type-ii weyl semimetals, *Nature (London)* **527**, 495 (2015).
- [10] B. Yan and C. Felser, Topological materials: Weyl semimetals, *Annu. Rev. Condens. Matter Phys.* **8**, 337 (2017).
- [11] G. Chang, B. J. Wieder, F. Schindler, D. S. Sanchez, I. Belopolski, S.-M. Huang, B. Singh, D. Wu, T.-R. Chang, T. Neupert *et al.*, Topological quantum properties of chiral crystals, *Nat. Mater.* **17**, 978 (2018).
- [12] Z.-M. Yu, W. Wu, Y. X. Zhao, and S. A. Yang, Circumventing the no-go theorem: A single weyl point without surface fermi arcs, *Phys. Rev. B* **100**, 041118(R) (2019).
- [13] M. Xiao, L. Ye, C. Qiu, H. He, Z. Liu, and S. Fan, Experimental demonstration of acoustic semimetal with topologically charged nodal surface, *Sci. Adv.* **6**, eaav2360 (2020).
- [14] M. A. Wilde, M. Dodenhöft, A. Niedermayr, A. Bauer, M. M. Hirschmann, K. Alpin, A. P. Schnyder, and C. Pfleiderer, Symmetry-enforced topological nodal planes at the fermi surface of a chiral magnet, *Nature (London)* **594**, 374 (2021).
- [15] N. Huber, K. Alpin, G. L. Causer, L. Worch, A. Bauer, G. Benka, M. M. Hirschmann, A. P. Schnyder, C. Pfleiderer, and M. A. Wilde, Network of topological nodal planes, multifold degeneracies, and Weyl points in CoSi , *Phys. Rev. Lett.* **129**, 026401 (2022).
- [16] B. Bradlyn, J. Cano, Z. Wang, M. Vergniory, C. Felser, R. J. Cava, and B. A. Bernevig, Beyond dirac and weyl fermions: Unconventional quasiparticles in conventional crystals, *Science* **353**, aaf5037 (2016).
- [17] P. Tang, Q. Zhou, and S.-C. Zhang, Multiple types of topological fermions in transition metal silicides, *Phys. Rev. Lett.* **119**, 206402 (2017).
- [18] N. Schröter, D. Pei, M. G. Vergniory, Y. Sun, K. Manna, F. De Juan, J. Krieger, V. Süß, M. Schmidt, P. Dudin *et al.*, Chiral topological semimetal with multifold band crossings and long fermi arcs, *Nat. Phys.* **15**, 759 (2019).
- [19] J. Cano, B. Bradlyn, and M. Vergniory, Multifold nodal points in magnetic materials, *APL Mater.* **7**, 101125 (2019).
- [20] H. Watanabe, H. C. Po, M. P. Zaletel, and A. Vishwanath, Filling-enforced gaplessness in band structures of the 230 space groups, *Phys. Rev. Lett.* **117**, 096404 (2016).
- [21] S. M. Young and C. L. Kane, Dirac Semimetals in Two Dimensions, *Phys. Rev. Lett.* **115**, 126803 (2015).
- [22] R. Takahashi, M. Hirayama, and S. Murakami, Spinless hourglass nodal-line semimetals, *Phys. Rev. B* **96**, 155206 (2017).
- [23] S. M. Young and B. J. Wieder, Filling-enforced magnetic dirac semimetals in two dimensions, *Phys. Rev. Lett.* **118**, 186401 (2017).
- [24] J. Zhang, Y.-H. Chan, C.-K. Chiu, M. G. Vergniory, L. M. Schoop, and A. P. Schnyder, Topological band crossings in hexagonal materials, *Phys. Rev. Mater.* **2**, 074201 (2018).
- [25] Y.-H. Chan, B. Kilic, M. M. Hirschmann, C.-K. Chiu, L. M. Schoop, D. G. Joshi, and A. P. Schnyder, Symmetry-enforced band crossings in trigonal materials: Accordion states and weyl nodal lines, *Phys. Rev. Mater.* **3**, 124204 (2019).
- [26] A. Leonhardt, M. M. Hirschmann, N. Heinsdorf, X. Wu, D. H. Fabini, and A. P. Schnyder, Symmetry-enforced topological band crossings in orthorhombic crystals: Classification and materials discovery, *Phys. Rev. Mater.* **5**, 124202 (2021).
- [27] M. M. Hirschmann, A. Leonhardt, B. Kilic, D. H. Fabini, and A. P. Schnyder, Symmetry-enforced band crossings in tetragonal materials: Dirac and weyl degeneracies on points, lines, and planes, *Phys. Rev. Mater.* **5**, 054202 (2021).
- [28] Z.-M. Yu, Z. Zhang, G.-B. Liu, W. Wu, X.-P. Li, R.-W. Zhang, S. A. Yang, and Y. Yao, Encyclopedia of emergent particles in three-dimensional crystals, *Sci. Bull.* **67**, 375 (2022).
- [29] Y.-M. Xie, X.-J. Gao, X. Y. Xu, C.-P. Zhang, J.-X. Hu, J. Z. Gao, and K. T. Law, Kramers nodal line metals, *Nat. Commun.* **12**, 3064 (2021).
- [30] J. Kruthoff, J. de Boer, J. van Wezel, C. L. Kane, and R.-J. Slager, Topological classification of crystalline insulators through band structure combinatorics, *Phys. Rev. X* **7**, 041069 (2017).
- [31] S. Ono and K. Shiozaki, Symmetry-based approach to superconducting nodes: Unification of compatibility conditions and gapless point classifications, *Phys. Rev. X* **12**, 011021 (2022).
- [32] F. Tang and X. Wan, Exhaustive construction of effective models in 1651 magnetic space groups, *Phys. Rev. B* **104**, 085137 (2021).
- [33] F. Tang and X. Wan, Complete classification of band nodal structures and massless excitations, *Phys. Rev. B* **105**, 155156 (2022).
- [34] A. Knoll and C. Timm, Classification of weyl points and nodal lines based on magnetic point groups for spin- $\frac{1}{2}$ quasiparticles, *Phys. Rev. B* **105**, 115109 (2022).
- [35] C. Fang, M. J. Gilbert, X. Dai, and B. A. Bernevig, Multi-Weyl topological semimetals stabilized by point group symmetry, *Phys. Rev. Lett.* **108**, 266802 (2012).
- [36] S. S. Tsirkin, I. Souza, and D. Vanderbilt, Composite weyl nodes stabilized by screw symmetry with and without time-reversal invariance, *Phys. Rev. B* **96**, 045102 (2017).
- [37] R. González-Hernández, E. Tuiran, and B. Uribe, Chiralities of nodal points along high-symmetry lines with screw rotation symmetry, *Phys. Rev. B* **103**, 235143 (2021).
- [38] T. Bevan, A. Manninen, J. Cook, J. Hook, H. Hall, T. Vachaspati, and G. Volovik, Momentum creation by vortices in superfluid ^3He as a model of primordial baryogenesis, *Nature (London)* **386**, 689 (1997).

- [39] N. P. Ong and S. Liang, Experimental signatures of the chiral anomaly in dirac–weyl semimetals, *Nat. Rev. Phys.* **3**, 394 (2021).
- [40] P. Hosur and X. Qi, Recent developments in transport phenomena in weyl semimetals, *C. R. Phys.* **14**, 857 (2013), topological insulators / Isolants topologiques.
- [41] A. A. Burkov, Chiral anomaly and transport in weyl metals, *J. Phys.: Condens. Matter* **27**, 113201 (2015).
- [42] T. Liang, Q. Gibson, M. N. Ali, M. Liu, R. J. Cava, and N. P. Ong, Ultrahigh mobility and giant magnetoresistance in the dirac semimetal Cd_3As_2 , *Nat. Mater.* **14**, 280 (2015).
- [43] F. de Juan, A. G. Grushin, T. Morimoto, and J. E. Moore, Quantized circular photogalvanic effect in weyl semimetals, *Nat. Commun.* **8**, 15995 (2017).
- [44] F. Flicker, F. de Juan, B. Bradlyn, T. Morimoto, M. G. Vergniory, and A. G. Grushin, Chiral optical response of multifold fermions, *Phys. Rev. B* **98**, 155145 (2018).
- [45] Z. Ni, K. Wang, Y. Zhang, O. Pozo, B. Xu, X. Han, K. Manna, J. Paglione, C. Felser, A. G. Grushin, F. de Juan, E. J. Mele, and L. Wu, Giant topological longitudinal circular photo-galvanic effect in the chiral multifold semimetal *cosi*, *Nat. Commun.* **12**, 154 (2021).
- [46] P. Liu, J. R. Williams, and J. J. Cha, Topological nanomaterials, *Nat. Rev. Mater.* **4**, 479 (2019).
- [47] A. A. Burkov, Topological semimetals, *Nat. Mater.* **15**, 1145 (2016).
- [48] L. M. Schoop, A. Topp, J. Lippmann, F. Orlandi, L. MÜchler, M. G. Vergniory, Y. Sun, A. W. Rost, V. Duppel, M. Krivenkov, S. Sheoran, P. Manuel, A. Varykhalov, B. Yan, R. K. Kremer, C. R. Ast, and B. V. Lotsch, Tunable weyl and dirac states in the nonsymmorphic compound *cesbte*, *Sci. Adv.* **4**, eaar2317 (2018).
- [49] M. M. Hirschmann, A. S. Gibbs, F. Orlandi, D. Khalyavin, P. Manuel, V. Abdolazimi, A. Yaresko, J. Nuss, H. Takagi, A. P. Schnyder, and A. W. Rost, Creating and controlling dirac fermions, weyl fermions, and nodal lines in the magnetic antiperovskite Eu_3PbO , *Phys. Rev. Mater.* **6**, 114202 (2022).
- [50] H. Nielsen and M. Ninomiya, The adler-bell-jackiw anomaly and weyl fermions in a crystal, *Phys. Lett. B* **130**, 389 (1983).
- [51] N. B. M. Schröter, S. Stolz, K. Manna, F. de Juan, M. G. Vergniory, J. A. Krieger, D. Pei, T. Schmitt, P. Dudin, T. K. Kim, C. Cacho, B. Bradlyn, H. Borrmann, M. Schmidt, R. Widmer, V. N. Strocov, and C. Felser, Observation and control of maximal chern numbers in a chiral topological semimetal, *Science* **369**, 179 (2020).
- [52] M. Yao, K. Manna, Q. Yang, A. Fedorov, V. Voroshnin, B. Valentin Schwarze, J. Hornung, S. Chattopadhyay, Z. Sun, S. N. Guin *et al.*, Observation of giant spin-split fermi-arc with maximal chern number in the chiral topological semimetal *ptga*, *Nat. Commun.* **11**, 2033 (2020).
- [53] Y. X. Zhao and A. P. Schnyder, Nonsymmorphic symmetry-required band crossings in topological semimetals, *Phys. Rev. B* **94**, 195109 (2016).
- [54] T. L. Hughes, E. Prodan, and B. A. Bernevig, Inversion-symmetric topological insulators, *Phys. Rev. B* **83**, 245132 (2011).
- [55] C. Fang, M. J. Gilbert, and B. A. Bernevig, Bulk topological invariants in noninteracting point group symmetric insulators, *Phys. Rev. B* **86**, 115112 (2012).
- [56] A. Alexandradinata, X. Dai, and B. A. Bernevig, Wilson-loop characterization of inversion-symmetric topological insulators, *Phys. Rev. B* **89**, 155114 (2014).
- [57] A. Bouhon and A. M. Black-Schaffer, Global band topology of simple and double dirac-point semimetals, *Phys. Rev. B* **95**, 241101(R) (2017).
- [58] A. Bouhon, G. F. Lange, and R.-J. Slager, Topological correspondence between magnetic space group representations and subdimensions, *Phys. Rev. B* **103**, 245127 (2021).
- [59] D. Vanderbilt, *Berry Phases in Electronic Structure Theory: Electric Polarization, Orbital Magnetization and Topological Insulators* (Cambridge University Press, Cambridge, 2018).
- [60] A. A. Soluyanov and D. Vanderbilt, Smooth gauge for topological insulators, *Phys. Rev. B* **85**, 115415 (2012).
- [61] D. Xiao, M.-C. Chang, and Q. Niu, Berry phase effects on electronic properties, *Rev. Mod. Phys.* **82**, 1959 (2010).
- [62] M. M. Hirschmann, Topological band crossings in metals, magnets, and non-Hermitian systems, Ph.D. thesis, University of Stuttgart, 2021.
- [63] A. Furusaki, Weyl points and dirac lines protected by multiple screw rotations, *Sci. Bull.* **62**, 788 (2017).
- [64] S.-M. Huang, S.-Y. Xu, I. Belopolski, C.-C. Lee, G. Chang, T.-R. Chang, B. Wang, N. Alidoust, G. Bian, M. Neupane, D. Sanchez, H. Zheng, H.-T. Jeng, A. Bansil, T. Neupert, H. Lin, and M. Z. Hasan, New type of weyl semimetal with quadratic double weyl fermions, *Proc. Natl. Acad. Sci. USA* **113**, 1180 (2016).
- [65] W. Tan, X. Jiang, Y. Li, X. Wu, J. Wang, and B. Huang, A unified understanding of diverse spin textures of kramers–weyl fermions in nonmagnetic chiral crystals, *Adv. Funct. Mater.* **32**, 2208023 (2022).
- [66] Q. Chen, F. Chen, Y. Pan, C. Cui, Q. Yan, L. Zhang, Z. Gao, S. A. Yang, Z.-M. Yu, H. Chen *et al.*, Discovery of a maximally charged weyl point, *Nat. Commun.* **13**, 7359 (2022).
- [67] B. Feng, Y.-H. Chan, Y. Feng, R.-Y. Liu, M.-Y. Chou, K. Kuroda, K. Yaji, A. Harasawa, P. Moras, A. Barinov *et al.*, Spin texture in type-ii weyl semimetal WTe_2 , *Phys. Rev. B* **94**, 195134 (2016).
- [68] I. Marković, C. Hooley, O. J. Clark, F. Mazzola, M. D. Watson, J. M. Riley, K. Volckaert, K. Underwood, M. Dyer, P. Murgatroyd *et al.*, Weyl-like points from band inversions of spin-polarised surface states in *nbgesb*, *Nat. Commun.* **10**, 5485 (2019).
- [69] S.-Y. Xu, I. Belopolski, D. S. Sanchez, M. Neupane, G. Chang, K. Yaji, Z. Yuan, C. Zhang, K. Kuroda, G. Bian *et al.*, Spin polarization and texture of the fermi arcs in the Weyl fermion semimetal TaAs , *Phys. Rev. Lett.* **116**, 096801 (2016).
- [70] G. Gatti, D. Gosálbez-Martínez, S. S. Tsirkin, M. Fanciulli, M. Puppini, S. Polishchuk, S. Moser, L. Testa, E. Martino, S. Roth *et al.*, Radial spin texture of the Weyl fermions in chiral tellurium, *Phys. Rev. Lett.* **125**, 216402 (2020).
- [71] W.-Y. He, X. Y. Xu, and K. T. Law, Kramers weyl semimetals as quantum solenoids and their applications in spin-orbit torque devices, *Commun. Phys.* **4**, 66 (2021).
- [72] K. Hagiwara, P. Rüßmann, X. L. Tan, Y.-J. Chen, K. Ueno, V. Feyer, G. Zamborlini, M. Jugovac, S. Suga, S. Blügel *et al.*, Link between weyl-fermion chirality and spin texture, [arXiv:2205.15252](https://arxiv.org/abs/2205.15252).

- [73] T. Zhang, R. Takahashi, C. Fang, and S. Murakami, Twofold quadruple weyl nodes in chiral cubic crystals, *Phys. Rev. B* **102**, 125148 (2020).
- [74] H. Li, T. Zhang, A. Said, Y. Fu, G. Fabbris, D. G. Mazzone, J. Zhang, J. Lapano, H. N. Lee, H. C. Lei, M. P. M. Dean, S. Murakami, and H. Miao, Observation of a chiral wave function in the twofold-degenerate quadruple weyl system bapgte, *Phys. Rev. B* **103**, 184301 (2021).
- [75] C. Cui, X.-P. Li, D.-S. Ma, Z.-M. Yu, and Y. Yao, Charge-four weyl point: Minimum lattice model and chirality-dependent properties, *Phys. Rev. B* **104**, 075115 (2021).
- [76] L. Luo, W. Deng, Y. Yang, M. Yan, J. Lu, X. Huang, and Z. Liu, Observation of quadruple weyl point in hybrid-weyl phononic crystals (unpublished).
- [77] L. Elcoro, B. Bradlyn, Z. Wang, M. G. Vergniory, J. Cano, C. Felser, B. A. Bernevig, D. Orobengoa, G. Flor, and M. I. Aroyo, Double crystallographic groups and their representations on the Bilbao crystallographic server, *J. Appl. Crystallogr.* **50**, 1457 (2017).
- [78] A. Bouhon and A. M. Black-Schaffer, Bulk topology of line-nodal structures protected by space group symmetries in class AI, [arXiv:1710.04871](https://arxiv.org/abs/1710.04871).
- [79] P.-M. Chiu, C.-Y. Huang, W.-J. Li, and T.-K. Lee, Emergence of topological phases by stacking of two-dimensional lattices with nonsymmorphic symmetry, *J. Phys.: Condens. Matter* **31**, 035501 (2019).
- [80] R. González-Hernández, E. Tuiran, and B. Uribe, Topological electronic structure and weyl points in nonsymmorphic hexagonal materials, *Phys. Rev. Mater.* **4**, 124203 (2020).
- [81] O. Türker and S. Moroz, Weyl nodal surfaces, *Phys. Rev. B* **97**, 075120 (2018).
- [82] W. Wu, Y. Liu, S. Li, C. Zhong, Z.-M. Yu, X.-L. Sheng, Y. X. Zhao, and S. A. Yang, Nodal surface semimetals: Theory and material realization, *Phys. Rev. B* **97**, 115125 (2018).
- [83] M. I. Aroyo, A. Kirov, C. Capillas, J. Perez-Mato, and H. Wondratschek, Bilbao crystallographic server. ii. representations of crystallographic point groups and space groups, *Acta Crystallogr., Sect. A: Found. Crystallogr.* **62**, 115 (2006).
- [84] J. M. Luttinger, Quantum theory of cyclotron resonance in semiconductors: General theory, *Phys. Rev.* **102**, 1030 (1956).
- [85] D. Gresch, Identifying Topological Semimetals, Ph.D. thesis, ETH Zurich (2018).
- [86] Y. Jiang, Z. Fang, and C. Fang, A $k \cdot p$ effective hamiltonian generator, *Chin. Phys. Lett.* **38**, 077104 (2021).
- [87] W. Rarita and J. Schwinger, On a theory of particles with half-integral spin, *Phys. Rev.* **60**, 61 (1941).
- [88] M. Ezawa, Pseudospin- $\frac{3}{2}$ fermions, type-ii weyl semimetals, and critical weyl semimetals in tricolor cubic lattices, *Phys. Rev. B* **94**, 195205 (2016).
- [89] L. Liang and Y. Yu, Semimetal with both rarita-schwinger-weyl and weyl excitations, *Phys. Rev. B* **93**, 045113 (2016).
- [90] G. Chang, S.-Y. Xu, B. J. Wieder, D. S. Sanchez, S.-M. Huang, I. Belopolski, T.-R. Chang, S. Zhang, A. Bansil, H. Lin *et al.*, Unconventional chiral fermions and large topological fermi arcs in RhSi, *Phys. Rev. Lett.* **119**, 206401 (2017).
- [91] M. Lin, I. Robredo, N. B. M. Schröter, C. Felser, M. G. Vergniory, and B. Bradlyn, Spin-momentum locking from topological quantum chemistry: Applications to multifold fermions, *Phys. Rev. B* **106**, 245101 (2022).
- [92] A. Jain, S. P. Ong, G. Hautier, W. Chen, W. D. Richards, S. Dacek, S. Cholia, D. Gunter, D. Skinner, G. Ceder, and K. A. Persson, The Materials Project: A materials genome approach to accelerating materials innovation, *APL Mater.* **1**, 011002 (2013).
- [93] P. Giannozzi, S. Baroni, N. Bonini, M. Calandra, R. Car, C. Cavazzoni, D. Ceresoli, G. L. Chiarotti, M. Cococcioni, I. Dabo *et al.*, Quantum espresso: A modular and open-source software project for quantum simulations of materials, *J. Phys.: Condens. Matter* **21**, 395502 (2009).
- [94] T. Zhang, Y. Jiang, Z. Song, H. Huang, Y. He, Z. Fang, H. Weng, and C. Fang, Catalogue of topological electronic materials, *Nature (London)* **566**, 475 (2019).
- [95] M. Vergniory, L. Elcoro, C. Felser, N. Regnault, B. A. Bernevig, and Z. Wang, A complete catalogue of high-quality topological materials, *Nature (London)* **566**, 480 (2019).
- [96] S. F. Matar, R. Pöttgen, and M. Nakhil, Electronic structure and chemical bonding in lairsi-type intermetallics, *Z. Naturforsch., B* **72**, 207 (2017).
- [97] G. Brauer, Die oxyde des niobs, *Z. Anorg. Allg. Chem.* **248**, 1 (1941).
- [98] A. Magneli, G. Andersson, and G. Sundkvist, Note on the crystal structure of niobium dioxide, *Acta Chem. Scand., Ser. A and Ser. B* **9**, 1402 (1955).
- [99] A. O'Hara, T. N. Nunley, A. B. Posadas, S. Zollner, and A. A. Demkov, Electronic and optical properties of NbO₂, *J. Appl. Phys.* **116**, 213705 (2014).
- [100] K. Seta and K. Naito, Calorimetric study of the phase transition in NbO₂, *J. Chem. Thermodyn.* **14**, 921 (1982).
- [101] S. Shapiro, J. Axe, G. Shirane, and P. Raccach, Neutron scattering study of the structural phase transition in NbO₂, *Solid State Commun.* **15**, 377 (1974).
- [102] C. Rao, G. R. Rao, and G. S. Rao, Semiconductor-metal transitions in NbO₂ and Nb_{1-x}V_xO₂, *J. Solid State Chem.* **6**, 340 (1973).
- [103] K. Jacob, C. Shekhar, M. Vinay, and Y. Waseda, Thermodynamic properties of niobium oxides, *J. Chem. Eng. Data* **55**, 4854 (2010).
- [104] H.-J. Schweizer and R. Gruehn, Zur darstellung und kristallstruktur von β -NbO₂/synthesis and crystal structure of β -NbO₂, *Z. Naturforsch., B* **37**, 1361 (1982).
- [105] K. J. Schulz, N. M. Piatak, and J. F. Papp, Niobium and tantalum, Tech. Rep. (US Geological Survey, 2017).
- [106] H. T. Stokes, D. M. Hatch, B. J. Campbell, and D. E. Tanner, Isodisplace: A web-based tool for exploring structural distortions, *J. Appl. Crystallogr.* **39**, 607 (2006).
- [107] W. Setyawan and S. Curtarolo, High-throughput electronic band structure calculations: Challenges and tools, *Comput. Mater. Sci.* **49**, 299 (2010).
- [108] Z. Wang, D. Gresch, A. A. Soluyanov, W. Xie, S. Kushwaha, X. Dai, M. Troyer, R. J. Cava, and B. A. Bernevig, MoTe₂: A Type-II Weyl topological metal, *Phys. Rev. Lett.* **117**, 056805 (2016).
- [109] I. Belopolski, P. Yu, D. S. Sanchez, Y. Ishida, T.-R. Chang, S. S. Zhang, S.-Y. Xu, H. Zheng, G. Chang, G. Bian *et al.*, Signatures of a time-reversal symmetric weyl semimetal with only four weyl points, *Nat. Commun.* **8**, 942 (2017).
- [110] T. Fukui, Y. Hatsugai, and H. Suzuki, Chern numbers in discretized brillouin zone: Efficient method of computing (spin) hall conductances, *J. Phys. Soc. Jpn.* **74**, 1674 (2005).

- [111] M. I. Aroyo, D. Orobengoa, G. de la Flor, E. S. Tasci, J. M. Perez-Mato, and H. Wondratschek, Brillouin-zone database on the *Bilbao Crystallographic Server*, *Acta Crystallogr. Sect. A* **70**, 126 (2014).
- [112] W. Wu, Z.-M. Yu, X. Zhou, Y. X. Zhao, and S. A. Yang, Higher-order dirac fermions in three dimensions, *Phys. Rev. B* **101**, 205134 (2020).
- [113] G. Kresse and J. Hafner, *Ab initio* molecular dynamics for liquid metals, *Phys. Rev. B* **47**, 558 (1993).
- [114] G. Kresse and J. Furthmüller, Efficiency of ab-initio total energy calculations for metals and semiconductors using a plane-wave basis set, *Comput. Mater. Sci.* **6**, 15 (1996).
- [115] G. Kresse and J. Furthmüller, Efficient iterative schemes for ab initio total-energy calculations using a plane-wave basis set, *Phys. Rev. B* **54**, 11169 (1996).
- [116] P. Giannozzi, O. Andreussi, T. Brumme, O. Bunau, M. B. Nardelli, M. Calandra, R. Car, C. Cavazzoni, D. Ceresoli, M. Cococcioni *et al.*, Advanced capabilities for materials modelling with quantum espresso, *J. Phys.: Condens. Matter* **29**, 465901 (2017).
- [117] D. R. Hamann, Optimized norm-conserving Vanderbilt pseudopotentials, *Phys. Rev. B* **88**, 085117 (2013).
- [118] M. J. van Setten, M. Giantomassi, E. Bousquet, M. J. Verstraete, D. R. Hamann, X. Gonze, and G.-M. Rignanese, The pseudodojo: Training and grading a 85 element optimized norm-conserving pseudopotential table, *Comput. Phys. Commun.* **226**, 39 (2018).
- [119] J. P. Perdew, K. Burke, and M. Ernzerhof, Generalized gradient approximation made simple, *Phys. Rev. Lett.* **77**, 3865 (1996).
- [120] A. A. Mostofi, J. R. Yates, G. Pizzi, Y.-S. Lee, I. Souza, D. Vanderbilt, and N. Marzari, An updated version of wannier90: A tool for obtaining maximally-localised Wannier functions, *Comput. Phys. Commun.* **185**, 2309 (2014).
- [121] Q. Wu, S. Zhang, H.-F. Song, M. Troyer, and A. A. Soluyanov, Wannertools: An open-source software package for novel topological materials, *Comput. Phys. Commun.* **224**, 405 (2018).